Surface Acoustic Mode Aluminum Nitride Transducer for micro-size liquid sensing applications

Bui, Thu Hang

DOI
10.4233/uuid:84d9d425-1b2c-46c3-b256-feeeb8fa3351

Publication date
2018

Document Version
Final published version

Citation (APA)
Bui, T. H. (2018). *Surface Acoustic Mode Aluminum Nitride Transducer for micro-size liquid sensing applications*. [Dissertation (TU Delft), Delft University of Technology].
https://doi.org/10.4233/uuid:84d9d425-1b2c-46c3-b256-feeeb8fa3351

SURFACE ACOUSTIC MODE ALUMINUM NITRIDE TRANSDUCER FOR MICRO-SIZE LIQUID SENSING APPLICATIONS

SURFACE ACOUSTIC MODE ALUMINUM NITRIDE TRANSDUCER FOR MICRO-SIZE LIQUID SENSING APPLICATIONS

Proefschrift

ter verkrijging van de graad van doctor
aan de Technische Universiteit Delft,
op gezag van de Rector Magnificus prof.dr. ir. T.H.J.J. van der Hagen,
voorzitter van het College voor Promoties,
in het openbaar te verdedigen op
maandag 26 November 2018 om 12:30

door

Thu Hang BUI

Master in Electronics - Telecommunication Technology,
University of Engineering and Technology, VNU-Hanoi, Vietnam
geboren te Hanoi, Vietnam

Dit proefschrift is goedgekeurd door de

Promotoren prof.dr. P.M. Sarro
prof.dr. T. Chu Duc

Samenstelling commissie:

Rector Magnificus,	voorzitter
Prof.dr. P.M. Sarro,	Technische Universiteit Delft, promotor
Prof.dr. T. Chu Duc,	Hanoi National University, promotor
Onafhankelijke leden:	
Prof.Dr.ir. J. Lötters,	Universiteit van Twente
Prof.dr. P.G. Steeneken,	Technische Universiteit Delft
Prof.dr.ir. M.J. Vellekoop,	Universiteit Bremen
Prof.dr. P.J. French,	Technische Universiteit Delft
Dr. G. Pandraud	Technische Universiteit Delft

Keywords: surface acoustic wave, microfluidics, piezoelectric sensor, liquid sensors

ISBN: 000-00-0000-000-0

Printed by: Ipskamp Printing, The Netherlands

CONTENTS

1

INTRODUCTION

In this chapter, we introduce the topic and objectives of the thesis: Surface acoustic mode aluminum nitride transducers for micro-size liquid sensing applications. A brief overview of the developments in microfluidics in relation to acoustic wave devices is given. Classification and existing problems of the acoustic wave modes are presented in order to provide reasons for choosing aluminum nitride based on surface acoustic waves for microfluidics applications. Finally, the structure of the thesis and the issues addressed in each chapter are outlined.

1

1.1. ACOUSTIC WAVE DEVICES FOR LIQUID SENSING

THE development of the integrated circuit (IC) in the 1970s (like monolithic processing, printed circuit board technologies, hybrid and multichip module technologies) and microelectromechanical systems (MEMS) in the late 1980s (like thin film materials, silicon micromachining, 3D lithography) have made a large variety of integrated sensors possible. These continuous developments in the microelectronics industry on one side and the increasing demand from the industry on the other side have further pushed the miniaturization of these sensors, both at chip level and for the overall system [1–4]. An interesting class of these microsensors is fluidic sensors, i.e. sensors for the detection of substances in the liquid state, or fluidic flow. For example, some typical applications are flow sensors for measuring the amount of fuel flowing inside an engine, or liquid level sensors for monitoring liquid level or liquid leaks in variety of home appliances (dishwashers, washing machines, detergent dispensers, clothes steamers, espresso machines, and heating-ventilation-air-conditioning HVAC), in vending machines, and industrial compressors, in food and beverage manufacturing, and many medical, transportation, aerospace and military applications [2, 4, 5].

First common methods used to recognize liquids are based on chemical reactions changing the coloring of the liquid and forming bubbles. However, in fact, when the analytes cannot be recognized, it needs chemical sensing technology. Fluidic sensors can be classified into six main types according to the signal domain used, i.e. based on the conversion of nonelectrical energy like thermal, radiation, mechanical, magnetic or bio (chemical) energy or images changes into an electrical or optical one [4]. Another classification for fluidic microsensors is based on the electrical output signal. This can be voltage (piezoelectric devices), current (photoelectric, ion sensitive field effect transistor ISFET devices), capacitance (co-planar, capacitive liquid level microsensors using dielectric permittivity variation), resistance (piezoresistive pressure microsensors) [4–6]. Capacitive sensors, available as commercial products, are often used to sense liquid properties such as liquid viscosity, liquid salt concentration, and liquid-level. The sensing mechanism is mostly based on changes in density. Disadvantages are shorter range (sensing scope from 3-60 mm [7]), bigger device [8–10] (for example, capacitive proximity sensors 10-30 mm [10]) and more sensitive to changes in environmental conditions such as temperature, and humidity and needs a non-conductive sublayer contacting the liquid medium [7, 11, 12]. Photoelectric devices are also used in commercial liquid sensors. However, they has some disadvantages, such as being affected by target materials or colors, shorter detection distance (50 m for the thru-beam type and 5 m for the diffuse reflective type while ultrasonic devices are up to 10 m), and lens are easily altered easily by contamination [13].

Among of them, piezoelectric devices are still largely preferred because of benefits of the piezoelectric effect, such as a small sensitivity to electrostatic-based and thermal-based actuation effects, faster response and greater efficiency (than other thermal devices). Besides, they have a greater energy density, a lower operating voltage, and a greater force-resisting capability than electrostatic devices (co-planar, capacitive devices), and a large range of the operating frequency [1, 4].

It is quite common that microsensors in liquid applications employ acoustic wave devices. The sensing mechanisms are based on the influence of mass loading, mechan-

ical properties, rheological properties, electrical properties and thermal effects on the mechanical wave velocity, magnitude attenuation or phase, frequency shift [6]. A remarkable property of acoustic wave sensors is to provide a direct response to physical and chemical properties of piezoelectric substrates and substances, such as surface mass, stress, strain, liquid density, viscosity, permittivity and conductivity [4]. Compared to other sensors, acoustic wave sensors have a larger attenuation range; a quick response of the piezoelectric effect; utilize an interdigital transducer (IDT) array, a comb structure, that can be fabricated using conventional CMOS and advanced MEMS technology; and can be embedded in a compact package (chips in microsize) [1–4]. Due to use the standard IC fabrication technology, it can be manufactured in large quantities at competitive cost. The basic mechanism is a change in velocity, in shift, attenuation and acoustic impedance of acoustic waves [6, 14, 15] caused by a change in the fluidic flow or the liquid composition. Thanks to the miniaturization the used technology permits and the response these devices can give, it is possible to use just a very small volume of the liquid sample, typically from a few picoliters (pl) to a few microliters. The integrated fluidic microsensor using acoustic wave devices has a dimension from a few square millimeters (mm^2) to a few square centimeters (cm^2) [3, 4, 16]. Typical commercial devices are acoustic wave filters, amplifier, pressure piezoelectric sensors and bio/chemical sensors which are integrated into a bigger system; for example having actuators, manipulators and even other sensors [1, 6, 17–19].

The piezoelectric effect was discovered in 1880s but it took until 1917 for the first quartz resonator, the first sensor based on acoustic waves, to be demonstrated [20, 21]. Until now, it has been applied for a wide range of sensors [6]. The operating mechanism is the conversion to an electrical output signal of nonelectrical input signal related to the impact induced by surrounding factors, like temperature, mass loading, magnetic waves or pressure. Like sensors in general, acoustic wave devices can be also classified according to the energy domain as shown in Fig 1.1. The first acoustic wave microsensors, the quartz resonators, belong to the group of mechanical sensors. They are still one of the most widespread applications of acoustic wave devices because of their high sensitivity and various measurable mechanical parameters from static, kinematic ones (such as external force, velocity, acceleration, vibration and flow rate) related to physical properties of materials (such as density, mass, strain, and viscosity) [4]. The second major application of acoustic waves is in radiation sensors. Commercial products which are often mentioned as highly effective acoustic wave microsensors are ultraviolet radiation and magnetic field sensors [22, 23]. Applying acoustic waves for biochemical sensors is an upcoming area, especially for the surface acoustic wave mode devices [6].

Generated acoustic waves can be longitudinal and transversal waves, traveling inside the piezoelectric plate or on the surface. Surface acoustic waves are often used in most of sensing applications in Fig 1.1 because of the high sensitivity (effects such as physical, chemical and biological properties of the substance can cause electrical perturbations of the device) and the simple design (pairs of interdigital electrodes lying on the surface of the piezoelectric material). Besides, they are also used in bio and microfluidics applications like transporting, mixing, atomizing and jetting microdroplets [6, 17, 24–26]. The developments in promising piezoelectric materials, such as quartz (SiO_2), lithium tantalate ($LiTaO_3$), lithium niobate ($LiNbO_3$), sapphire (Al_2O_3), lead zirconate titanate

1

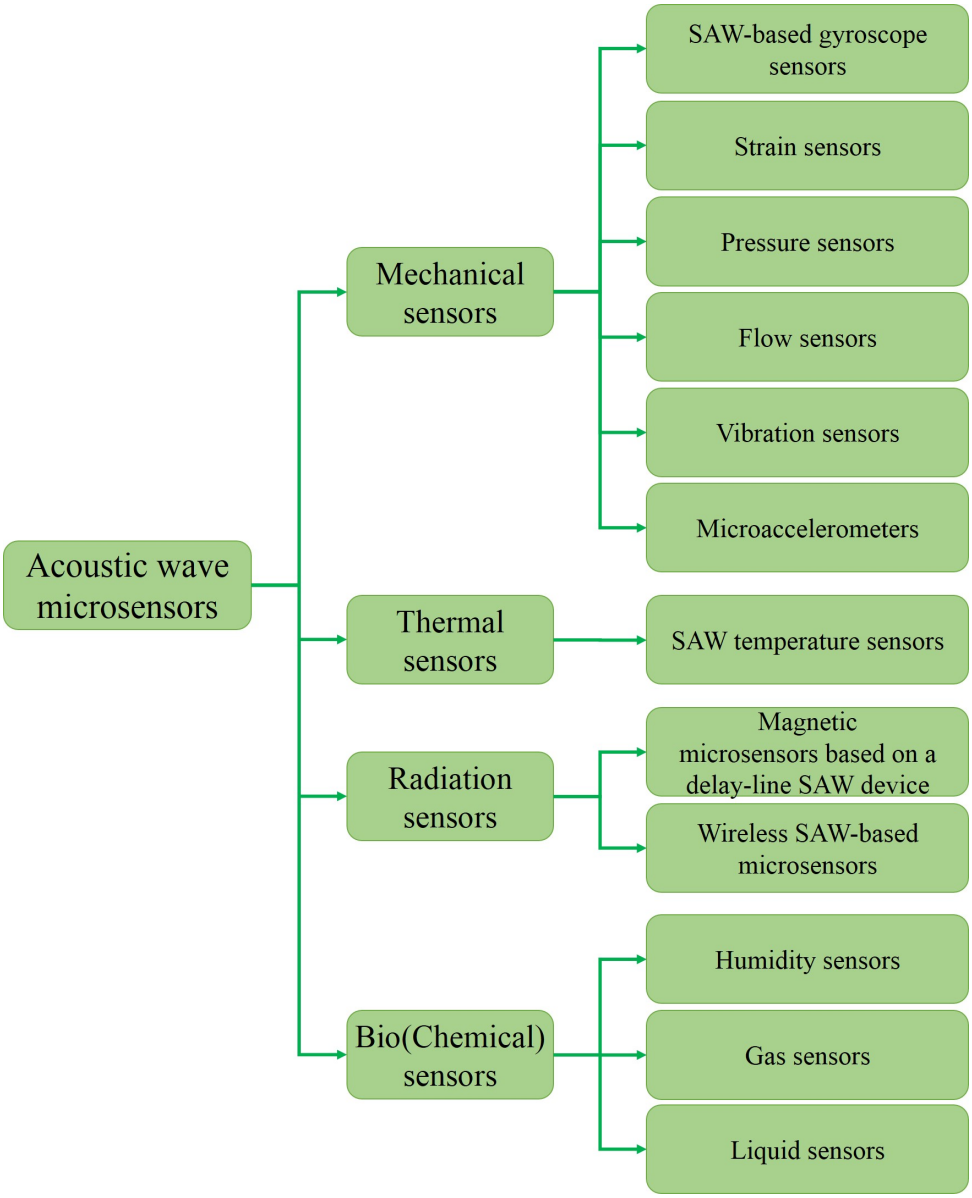

Figure 1.1: Classification of microsensors using acoustic waves and typical examples of microsensors based on acoustic waves [4], [6].

(PZT), zinc oxide (ZnO), and aluminum nitride (AlN) [15], have also contributed to an increase of the use of surface acoustic wave devices in microfluidics applications. Surface acoustic waves can be generated by a crystal or thin film on silicon, glass or flexible PDMS substrate. Parameters of the piezoelectric material, such as velocity, hardness,

piezo-constant d_{31} and d_{33}, effective coupling coefficient, coefficient of thermal expansion and sensitivity to substances, are considered when the material or configuration is selected. For example, for liquid in large volumes, flexural plate wave (FPW) devices are used instead of surface acoustic wave (SAW) devices because of the non-leaky characteristics of FPWs into liquid. However, for micro-volume liquids, SAW devices are often used because of the high sensitivity, easier fabrication, and more robust structure.

1.2. THE CHOICE OF THE SURFACE ACOUSTIC WAVE MODE FOR LIQUID SENSING

IN general, for the configuration and system integration, the SAW device has a simple and rugged structure. The SAW device is extremely sensitive to tiny mass changes and is capable of detecting 100 picogram/cm^2 (approximately 0.01 monolayer of carbon) [12]. Therefore, various commercial SAW devices are applied for sensing temperature or humidity [1, 4, 14].

For liquid applications, more physical effects, such as residual stress, material texture, discrepancies in the thermal expansion coefficients in the used non-CMOS materials, appear and they need to be taken into consideration. So, compatible CMOS materials and CMOS processing technology are preferred for microfluidics applications due to low power, dissipation, current, voltage and high device density that can be achieved. A low velocity and operating frequency are also required for liquid applications. A surface acoustic wave device is a good approach because it can operate at low radio frequency, be fabricated using CMOS compatible materials and in a CMOS-based process. Besides, the SAW device operates as perfect actuator or manipulator for liquid. So it can be designed and implemented both as sensor and as actuator or manipulator.

However, the SAW device has also some disadvantages for liquid sensing. Although a surface acoustic wave mode is quite common for liquid actuation and manipulation, it has some limitations for sensing due to the acoustic streaming and leakage. These phenomena cause excessive energy attenuation into the liquid medium. It leads to no output signal at the IDT receiver of the SAW device. A component of the SAWs causing an energy emission is a longitudinal component. The velocity of this component which is much larger than the velocity of the liquid causes this emission [14]. The attenuated energy of this component depends on the contact area between the piezoelectric material and the liquid medium. The contact area is often used to evaluate the perturbation level of the SAW device and the decay coefficient per propagation path of the longitudinal component into the liquid medium. Therefore, limiting the longitudinal component and the contact area is a potential approach for bypassing the restriction of SAW devices for liquid sensing applications

1.3. RESEARCH OBJECTIVE

THIS thesis focuses on applying a miniaturized SAW chip based on aluminum nitride for liquid sensing at micro-volume level. To achieve the objective of this research, the different parameters of the SAW device have been investigated and optimized by 3D numerical simulation (finite element method) and experimental validations. The inter-

action mechanism and emitted energy between SAWs and micro-size droplets is presented to design a suitable SAW device for a given volume of the liquid. The effect of the evaporation rate, the shape, micro-volume of the liquid and the surface wettability of the piezoelectric material on the SAW response is also reported. The SAW sensor has been developed for identifying liquid samples at microliter volume range. Another design of the miniaturized SAW chip integrated on a printed circuit board (PCB) has been developed for detecting liquid level inside the microhole. For the liquid flowing inside the microhole, the effect of the evaporation phenomenon, the difference in density and pressure are considered and preliminary results of the SAW beam response are reported, further demonstrating the potential capability of SAW devices for liquid sensing. Finally, some new optimized SAW structures, specifically designed for liquid sensing applications are proposed.

1.4. OUTLINE OF THE THESIS

IN the next chapters, the modeling, optimized structures, design, fabrication and liquid characterization of the realized SAW device are presented. Briefly the content of the following chapters is summarized as follows:

Chapter 2: The choice of SAW devices for bio- and microfluidics applications is motivated. Sensing mechanisms in general and applicable mechanisms of SAW sensors for liquid are presented. Besides, to determine the suitable design of the SAW device (such as material, deposition method for achieving the best piezoelectric quality and parameters of IDTs), three-dimension (3D) modeling of SAW devices based on finite element method (FEM) is performed and analyzed.

Chapter 3: The effect of a micro-size droplet shape, specifically the liquid contact angle, radius and area, on the SAW response is described. When a micro-size of the sessile droplet is dropped on the surface of the SAW device, the shape of the micro-size droplet can change during the experiment, due to physical phenomena, such as evaporation, wetting, spreading, and surface tension. It leads to an unstable response of the SAW device for sensing, manipulating and actuating applications. For liquids having a slow evaporation rate (BuAc*<0.8), for example water, and consequently a contact angle shrinking more than the contact radius, the SAW response can be stable for a longer time.

Chapter 4: In this chapter, a simple experiment to further prove sensing capability of the SAW device for microfluidic applications is shown. Taking advantage of the changeable SAW response related to the different shrinking shape and stagnant liquid molecules of each liquid, it is possible to detect samples in the microliter volume range. The mechanisms for identifying the liquid are physical properties (liquid density sound speed in liquid and evaporation rate) and mass loading (concentration of stagnant liquid molecules).

Chapter 5: This chapter shows a novel interrupted structure of the SAW device for sensing liquid. The device is miniaturized to be integrated on a printed circuit board (PCB). From the probable impacts happening at the nozzle during the liquid flowing,

* The term BuAc is n-butyl acetate which is a general reference material for evaluating evaporation rates. It is commonly abbreviated as BuAc and its relative evaporation rate is 1.0. When other materials, compared to BuAc = 1.0, have an evaporation rate smaller than 0.8, they are defined having slow evaporation speed.

individual studies of the on-chip SAW device, including sensing the changing density and pressure of the liquid inside the interrupted propagation path, are presented. Preliminary experiments are performed by sensing liquid inside the chamber of the SAW structure during the evaporation process.

Chapter 6: Optimized structures of the SAW device are proposed for liquid sensing applications. Comparison to the conventional SAW transducer shows that the focused IDT structure has a more concentrated acoustic wave beam at the center of the propagation path. This is determined by the more excessive loss due to the obstacles on the propagation path. Also in this chapter, a mixing IDT structure for the SAW device is presented. It shows the sensing potential of the SAW device based on the phase shift, while conventional devices cannot receive an output signal due to leaky energy of the longitudinal component inside the liquid medium.

Chapter 7: Main conclusions and suggestions for future work are given in this chapter.

REFERENCES

[1] V. Ferrari and R. Lucklum, *Overview of acoustic-wave microsensors,* (Berlin, Heidelberg: Springer Berlin Heidelberg, 2008) Chap. Piezoelectric Transducers and Applications, pp. 39–62.

[2] M. Elwenspoek and R. J. Wiegerink, *Mechanical Microsensors* (Springer, 2001).

[3] J. K. Luo, Y. Q. Fu, and W. I. Milne, *Acoustic wave based microfluidics and lab-on-a-chip,* (Rijeka: InTech, 2013) Chap. Modeling and Measurement Methods for Acoustic Waves and for Acoustic Microdevices.

[4] J. W. Gardner, V. K. Varadan, and O. O. Awadelkarim, *Microsensors, MEMS and Smart Devices* (JOHN WILEY & SONS, LTD, 2002).

[5] J. W. Gardner, *Microsensors: principles and applications* (Wiley, 1994).

[6] P. Malcovati and F. Maloberti, *Mems: A practical guide of design, analysis, and applications,* (Springer-Verlag Berlin Heidelberg, 2006) Chap. Chapter 17: Interface Circuitry and Microsystems.

[7] T. A. Kinney, *Application Engineer*, Tech. Rep. (Baumer Electric, 9/2001).

[8] J. Z. Chen, A. A. Darhuber, S. M. Troian, and a. S. Wagner, *Capacitive sensing of droplets for micro?uidic devices based on thermocapillary actuation,* MINIATURISATION FOR CHEMISTRY, BIOLOGY & BIOENGINEERING (2004).

[9] N. Blaz, A. Mari, S. Toskov, G. Miskovic, G. Radosavljevi, and L. Zivanov, *Capacitive sensor for quantity detection of known liquid present in distilled water,* in *International Spring Seminar on Electronics Technology 37th* (2014).

[10] Baumer, *Capacitive sensors*, Tech. Rep. (Baumer).

[11] S. Lanka and S. Hanumanthaiah, *Capacitive sensor challenges and solutions for liquid-level sensing,* in *Cypress Semiconductor* (12/2017).

[12] N. R. Council, *Expanding the vision of sensor materials,* (Washington, DC: The National Academies Press, 1995) Chap. Chapter 6: CHEMICAL SENSORS.

[13] Panasonic, *Photoelectric sensors*, Tech. Rep. (Panasonic).

[14] J. Ballantine, R. M. White, S. I. Martin, A. J. Ricco, E. T. Zellers, G. C. Frye, and et al., *Acoustic Wave Sensors, 1st Edition: Theory, Design, & Physico-Chemical Applications* (USA: ACADEMIC PRESS, 1997).

[15] J. Gualtieri, J. A. Kosinski, and a. A. Ballato, *Piezoelectric materials for acoustic wave applications,* IEEE Transactions on Ultrasonics, Ferroelectrics, and Frequency Control (1994).

[16] Prime_Faraday_Technology_Watch, *An Introduction to MEMS (Microelectromechanical Systems)*, Tech. Rep. (PRIME Faraday Partnership, 2002).

[17] N. G. Durmus, R. L. Linb, M. Kozberg, D. Dermici, A. Khademhosseinie, and U. Demircie, *Encyclopedia of microfluidics and nanofluidics,* (Springer New York, 2015) Chap. Acoustic-Based Biosensors.

[18] M. M. Alghane, *SURFACE ACOUSTIC WAVE STREAMING IN A MICROFLUIDIC SYSTEM*, Ph.D. thesis, School of Engineering and Physical Sciences Heriot-Watt University (2013).

[19] T. A. F. Clemens and C. W. Ruppel, *Advances in surface acoustic wave technology, systems and applications* (Singapore: World Scientific, 2000).

[20] D. R. Morgan, *Surface acoustic wave devices and applications,* Ultrasonics (1973).

[21] A. V. Carazo, *50 years of piezoelectric transformers. trends in the technology,* in *MRS Proceedings* (2003).

[22] S. Kumar, G.-H. Kim, K. Sreenivas, and R. P. Tandon, *Zno based surface acoustic wave ultraviolet photo sensor,* Journal of Electroceramics (2009).

[23] B. Li, O. Yassine, and J. Kosel, *A surface acoustic wave passive and wireless sensor for magnetic fields, temperature, and humidity,* IEEE Sensors Journal (2015).

[24] L. Y. Yeo and J. R. Friend, *Surface acoustic wave microfluidics,* Annual Review of Fluid Mechanics (2014).

[25] A. Rezk, J. Friend, and L. Yeo, *Microfluidic devices for biomedical applications,* (Woodhead Publishing, 2013) Chap. 3 - Actuation mechanisms for microfluidic biomedical devices, pp. 100–138.

[26] Y. Q. Fu, J. S. Cherng, J. K. Luo, M. P. Y. Desmulliez, A. J. Walton, Y. Li, and a. F. Placido, *Acoustic waves,* (2010) Chap. Aluminium Nitride thin Film Acoustic Wave Device for Microfluidic and Biosensing Applications.

2

CHEMICAL SAW SENSORS

This chapter presents the advantages of using SAW devices based on aluminum nitride (AlN) for liquid sensing compared to other kinds of acoustic wave devices. A classification of the mechanism of common SAW sensors in general and applicable sensing mechanisms in liquid are presented. Also, the reason of choosing a CMOS compatible material like AlN is motivated. Thence, three-dimension modeling of SAW devices based on finite element method (FEM) is performed to determine the behavior of generated surface acoustic waves for specifically designed structures of the interdigital electrodes, and the attenuation caused by internal (topography of SAW devices) or external (liquid or gas samples, additional film or environment) effects on the device.

2.1. INTRODUCTION

BASED on modes of the acoustic waves, microsensors are classified into two main groups, bulk waves and surface waves based on the main energy concentration through the piezoelectric substrate. Bulk waves are a group of acoustic waves mostly generated and propagating through the substrate bulk whereas surface waves are generated and travelling mainly on the surface. Some are categorized into groups of bulk waves and surface waves, because they have displacement components traveling on the surface and through the piezoelectric bulk, like shear-horizontal acoustic plate waves (SH-APWs), flexural plate waves (FPWs) of Lamb waves as shown in Fig 2.1. In general, bulk acoustic waves include longitudinal waves (also referred to as compressional or extensional waves) and transverse waves (also referred to as shear waves) traveling mostly underneath the surface. Surface waves propagate mainly on the surface of the piezoelectric substrate. Commonly applied modes of the acoustic wave for microsensors are thickness-shear mode (TSM), SH-APW, SAW, and FPW (also called asymmetrical Lamb wave mode) [1–4]. The primary acoustic wave sensor for liquid sensing is a TSM resonator [1]. Since 1990s, research and utilization of the other acoustic wave modes, like shear-horizontal plate wave mode and flexural plate wave mode of SH-APM and FPW devices, which are not excessively damping into liquid, has led to a wide range of acoustic sensors for liquid applications.

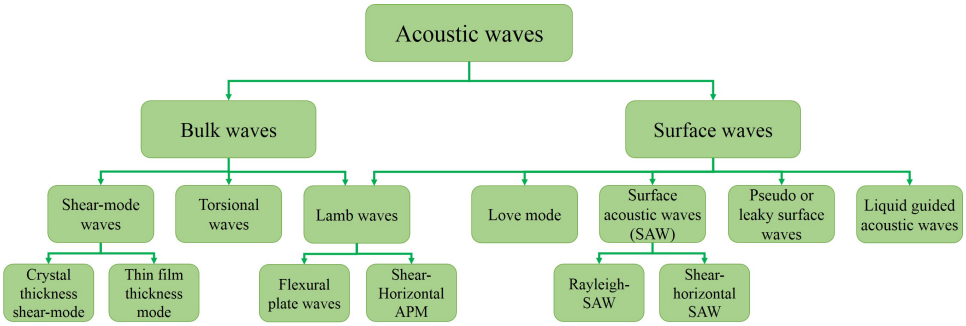

Figure 2.1: Classification of acoustic wave types [1, 4, 5].

Depending on the substance, size, shape, material, sensitivity level and operation frequency suitable to a specific application, one of the available types of acoustic wave is chosen. For example, surface acoustic wave sensors are often used for pressure sensors because of the high sensitivity to changes generated by small effects on the surface. Bulk waves are used for vibration sensors, like quartz crystals because the device is fabricated by a thicker film or crystal and consequently more robust and resistant to stronger forces than surface wave devices. However, these applications rarely use flexural acoustic wave devices because the thickness of the substrate can be only a few micrometers, thus still fragile for external forces. But for liquid sensing applications based on acoustic waves, the flexural acoustic wave device is one of the best choices [4].

A typical piezoelectric structure is an interdigital transducer (IDT), which includes input and output comb-shaped arrays of metallic electrodes, and generates several acous-

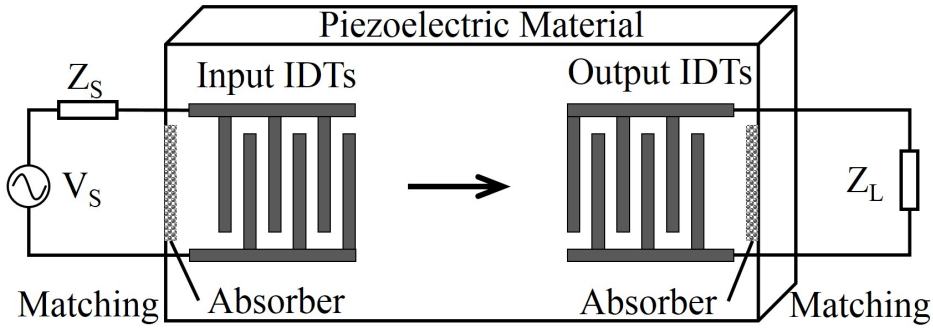

Figure 2.2: Basic interdigital transducer with a pair of IDT arrays.

tic wave modes as shown in Fig 2.2. The most used electrodes are aluminum (Al), gold/chrome (Au/Cr), and gold/titanium (Au/Ti). An applied voltage on the input IDTs excites mechanical waves by the piezoelectric effect. The signal is in the radio frequency range (several decades of kHz to a decade of GHz) [1–4, 6]. These waves travel through the piezoelectric substrate to the output IDTs. Depending on the structure of the device, different modes of mechanical waves are generated. Commonly used modes using a thin piezoelectric film, like thin-film shear-mode bulk acoustic wave (thin-film shear-mode BAW), shear horizontal acoustic plate mode (SH-APM), surface acoustic wave (SAW) mode and flexural plate wave (FPW) mode, have been utilized for many microfluidic applications [4, 7, 8] as summarized in Table 2.1. The reason is that it can provide higher sensitivity, integrated circuit (IC) compatibility and lower cost [9].

Table 2.1: Development of thin-film acoustic wave microsensors [4, 5, 8, 10–12].

Type	**Example**	**Discovery**	**Sensing Application**	**Substance**	
				Gas	**Liquid**
Thin-film shear-mode BAW	Thin film bulk wave resonator	1959	2000s	X	X
Shear-horizontal acoustic plate sensors	Immunosensor, urease biosensor	1908s	1990s	X	X
Flexural plate wave sensors	Liquid sensor	1917	1988		X
Surface acoustic wave (SAW)	SAW vapor, pressure and humidity sensors	1978	1970s	X	

2.2. ACOUSTIC MODES FOR LIQUID APPLICATIONS

2.2.1. THIN-FILM SHEAR-MODE BAW

THE first idea using a thin film for shear mode BAW sensors is from the assumption of Sauerbrey in 1959 [13] and King in 1964 [14]. It is employed for a micro-gravimetric in the gas phase as equivalent mass change on the quartz crystal sensor. Later Thompson proposed a liquid-phase thickness shear mode (TSM) sensor using Langmuir-Blodgett film of stearic acid [11, 15]. Then, a new technique for the thin film deposition was employed, namely epitaxial growth, which had some limitations in crystalline orientation control. Lattice mismatch between the piezoelectric film and the substrate results in poor quality of the piezoelectric layer. By selecting the most appropriate ion beam deposition techniques (evaporation, sputtering), the orientation mismatch between in- and out-of- plane could be solved and opened a new era for the thin-film based piezoelectric sensors [9]. Common materials for the thin film TSMs are ZnO and AlN due to their wurtzite structure. The first commercial products, such as viscosity sensors and biosensors with c-axis tilted ZnO or AlN films, appeared in 2000s [9].

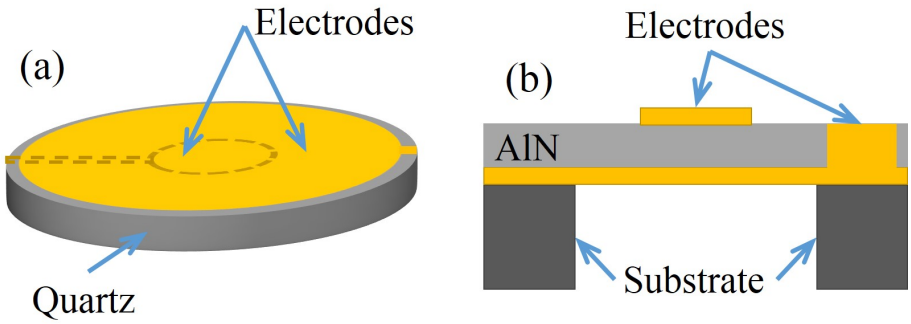

Figure 2.3: Schematic view of a TSM resonator based on (a) Quartz crystal and (b) AlN thin film (also called thin film bulk acoustic resonator – FBAR).

A crystal TSM sensor includes a metal electrode at the bottom and at the top of the quartz, while a thin film bulk acoustic resonator (FBAR) is placed on a silicon substrate as shown in Fig 2.3. Shear mode FBAR structures are used for gas and liquid sensing, especially highly sensitive to liquid biosensors [16]. Compared to the crystal TSM, the FBAR has some advantages such as a scalable fabrication using an IC-compatible process, smaller size, larger operation frequency range (from few hundred MHz to several GHz) and easily selectable operation frequency. The thickness of the thin film ranging from several micrometres to tenth of micrometres is relative to the frequency ranging from 100 MHz to 10 GHz.

A disadvantage of the thin-film shear-mode BAW device is the crystalline orientation control for both in- and out-of-plane direction to excite more shear waves and reduce longitudinal waves [9]. A c-axis inclined piezoelectric thin film (like ZnO and AlN) is the best way to avoid this attenuation [9, 17]. Besides, to attain the extremely high resonant frequency of the FBAR device, e.g. several GHz, it is necessary to reduce the thickness

of the piezoelectric layer to tens of nanometres. This also leads to reducing significantly the electromechanical coupling coefficient (k^2) and the quality factor (Q). For a low resonant frequency, e.g. several MHz, the thickness of the piezoelectric film should be high, but this can increase stress and uniformity of the piezoelectric thin film [18]. Therefore, when the thin film TSM (or FBAR) device is used, the more relevant parameters to consider are the control of the crystal direction, limitation of the thin-film thickness, requirements of the read-out ICs, noises and Q factors.

2.2.2. SHEAR-HORIZONTAL ACOUSTIC PLATE MODE (SH-APM)

SHEAR-HORIZONTAL acoustic plate mode (SH-APM) sensors, first introduced in 1980s, can be made from a thin plate of piezoelectric materials or crystal [19]. It combines shear horizontal waves on the surface and bulk waves through the plate. Energy is therefore spreading at the top and bottom of the substrate as shown in Fig 2.4. It can be applied for both gas and liquid applications, but is mostly used for liquid applications because of lower energy loss into liquid medium. The typical range of the operation frequency is 25-200 MHz [19]. The most commonly used thin plate for the SH-APM sensors is a 0.5 mm Z-X $LiNbO_3$ [5].

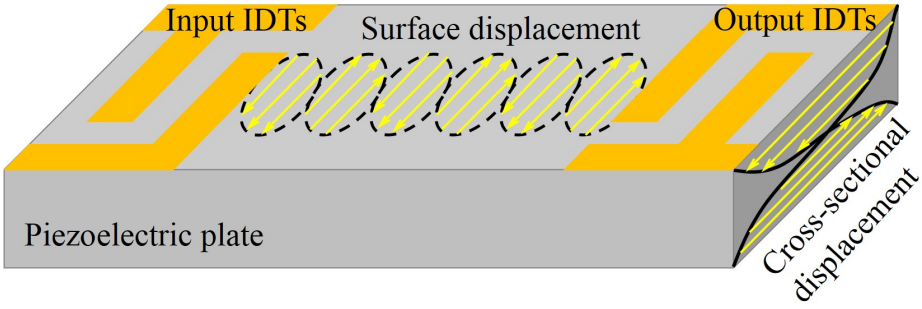

Figure 2.4: 3D SH-APM device with the schematic diagram of the wave motions on the surface and inside the plate.

Like BAW devices, its sensitivity is inversely proportional to the substrate thickness but it can work better in the higher frequency ranger than BAW devices [4].

The structure of the SH-APM device is quite similar to the SAW device which is configured by in- and output IDT arrays. This electric part can be placed at the bottom of the piezoelectric plate to isolate it from the liquid medium, thus avoiding possible metal corrosion and contamination problems from samples. However, both high and low order modes are excited simultaneously, while the frequency separation of modes is restricted. Besides, the acoustic wave response is affected by the mechanical and electrical loading of the piezoelectric surface. These are reasons that SH-APM is not really compatible to standard oscillator circuit [19]. Some reports indicate possible improvement by a guiding layer such as an AlN thin film [19, 20] placed on the bare silicon. However, compared to SAW devices, it is less sensitive because the energy of SH-APM waves at the surface does not reach the maximum at the surface.

2.2.3. LAMB WAVE OR FLEXURAL PLATE WAVE (FPW)

FLEXURAL plate waves are antisymmetric Lamb waves. Like longitudinal and shear-vertical components of SAWs, its particles travel in elliptical shape. The typical structure of the FPW device is similar to the SAW device as shown in Fig 2.5. The only difference is that the piezoelectric thin film is often placed on a layer of several micron oxide, nitride, or directly on the thick silicon substrate. The frequency range is from hundreds kHz to few MHz [1]. The operation mechanism of the FPW device is based on added mass to membrane instead of detecting changes in the operating frequency, like for the other acoustic devices [19]. Typically, FPW chips, operating at low frequency, often have larger size than other devices, so they would get benefit from integration. FPW sensors can analyze samples in real-time and compatibly with aqueous sample and changes in surface chemistry [19].

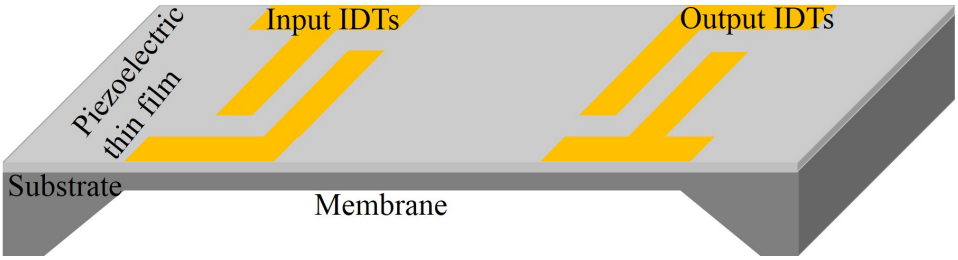

Figure 2.5: 3D schematic drawing of the flexural plate wave (FPW) device.

2.2.4. SURFACE ACOUSTIC WAVE (SAW)

SAW devices are developed and applied originally for filters and delay line devices in the 1970s [8, 21]. Integrated SAW chips have scaled from tens of mm^2 in the 1990s to a few mm^2 nowadays [22]. The surface acoustic wave (SAW) device has two typical modes, Rayleigh-SAW (R-SAW) and shear-horizontal SAW (SH-SAW) as shown in Fig 2.6. R-SAWs have particles moving in elliptic shape and perpendicularly to the propagation path, whereas SH-SAWs, also referred to as surface transverse waves (STWs), have particles moving perpendicularly to the wave direction [4]. The energy of the SAW device concentrates mostly on the surface. A possible furthest penetration of the SAW beam into the substrate is smaller than several wavelengths and the penetration energy is inversely proportional to the frequency [1]. However, the higher the operating frequency is, the higher the sensitivity of SAW devices can reach.

Compared to the above thin film acoustic devices, SAW devices can work at much higher frequency and is more sensitive to perturbations on the surface [18, 21].

The first SAW sensors for detecting gas was reported in 1979 and then some attempts for liquid substance were engaged, but severe attenuation and high insertion losses of the compressional waves radiated into liquid medium were observed [19].

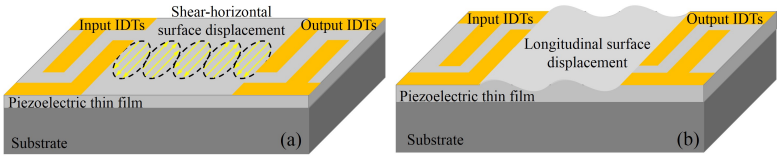

Figure 2.6: 3D schematic drawing of two types of the surface acoustic wave (SAW) device: (a) shear horizontal mode and (b) longitudinal mode.

2.2.5. COMPARISONS OF SENSORS FOR LIQUID APPLICATIONS

THE SAW sensors have a higher stability, resolution and sensitivity than other acoustic sensors because energy of the SAW beam focuses mainly on the surface, making them more sensitive to perturbation on the propagation path [23, 24]. Specially, perturbations on the surface can be induced by factors in the environment, such as ambient temperature, heavy molecular particles, humidity and small external force (or pressure) [25–27]. Besides, the structure of the SAW device is more simple and easy to be fabricated with thin film technology, thus making them economically more attractive than devices manufactured by piezoelectric bulk materials.

The SAW device has some disadvantages when it is applied for liquid sensing applications because of the excessive radiation of the longitudinal component. Therefore, it is rarely applied for liquid sensing applications. TSM, SH-APM or FPW devices have been used instead. Liquid samples are droplets (several decades of microliters) or a flow [1, 3, 28]. Therefore, the devices often need to be large in size, 2 mm x 2 mm or more, to provide sufficient interaction area for the liquid samples [1, 3].

SAW devices are commonly used for actuation or manipulation of micro-size droplets [2]. The energy of SAWs radiates into droplets and becomes kinetic energy. For low input power, if there are particles like polystyrenes inside the droplet, they will move in ellipse shape. For higher input power, this kinetic energy can make the droplet move. How fast the droplet moves depends on the size of the droplet and the type of liquid. Some researches show it is possible to measure the position and sound velocity of the droplet, measure evaporation rate of the liquid, or biochemical recognition by SAW devices [2, 29, 30]. This means that the energy of SAWs is not completely absorbed into liquid medium and therefore, it is possible to use SAW devices as sensors for detection of a micro-volume liquid medium.

2.3. DETECTION MECHANISMS OF SAW MICROSENSORS

IN all commonly used biosensors for microfluidic applications, such as interdigital sensors (SH-APM and FPW mode [31]), transducer resonators [32] and capacitive sensors [33, 34], the detection mechanisms of the SAW device include mass loading (effects on an operation frequency) [1], physical properties (changes in operating frequency and attenuation effects induced by rheological properties or thermal effects of any liquid medium in contact with the piezoelectric layer) [1, 35], resistance and capacitance properties (changes induced by the dielectric constant of the medium between the plates or fluidic pressure variation) [33, 34]. For SAW sensors, besides the common mechanisms as

mentioned above, electrical properties are also used as the detection mechanism. Classification of SAW microsensors can be listed as shown in Table 2.2.

Table 2.2: Mechanisms of SAW microsensors [1, 4].

Type	Affected SAW factor	Perturbation	Application	
			Gas	Liquid
Mass loading	surface mass, displacement	frequency	X	X
Mechanical properties	viscous, elastic, viscoelastic	magnitude and frequency	X	X
Rheological properties	displacement, electric output	magnitude and frequency	X	
Thermal effect	substrate density, acoustic wave velocity	mostly frequency	X	X

2.3.1. MASS LOADING

MASS loading is the most used mechanism of the SAW sensor, and is due to translation of the surface mass, or the surface displacement of SAWs. It can be caused by mass addition or removal at the surface of the sensor. However these perturbations do not produce an attenuation effect on the wave velocity [1]. Changes in surface mass or surface displacement of SAWs only result in a frequency or phase velocity shift of the signal. Surface mass changes in gas or liquid sensing applications can be due to sorption (adsorption or absorption), or chemical reaction. The first sensor using SAW devices based on this mechanism is a gravimetric sensor. Mass changes, caused by a thin isotropic film overlaying the propagation path or sorption of the vapor on the polymer top-layer, drive the phase velocity shift [36, 37].

It is also used for detecting heavy gases that cause an increase in mass density and produce a decrease in frequency without any attenuation in magnitude [38]. The adsorption of gas molecules on the thin film is linearly dependent on the mass/density change of the film surface as written below [1]:

$$\Delta f \sim S_m \Delta m \tag{2.1}$$

where S_m is the device-specific coefficient which depends on the nature of the piezoelectric substrate, device dimension, operating frequency, and the acoustic mode while Δm is the change in mass per area of the SAW surface. For mass loading applications, only phase velocity or frequency shift is considered here during the measurement. Attenuation in magnitude can be ignored because the loss is insignificant.

2.3.2.

PERTURBATIONS in the mechanical properties of the surface are related to film deformations. These perturbations generate changes in both magnitude and frequency [1]. The properties of a thin film that can be affected are elastic, viscous or viscoelastic

(both elastic and viscous). In practice, the viscous and elastic parameters are often considered together, thus this mechanism is also referred to as viscoelastic effect of the SAW sensor [1, 24]. The typical polymer-coated SAW sensors based on mechanical properties changes are used for sensing gas molecules and gas concentration [39]. The polymer coating on the sensing area is considered as a sublayer of the viscoelastic film. The SAW response is induced by the shear modulus G, the bulk modulus K, film thickness h and mass density ρ. The change in SAW propagation induced by this perturbation is given by [1]:

$$\frac{\Delta\gamma}{k_0} = \frac{\Delta\alpha}{k_0} - j\frac{\Delta v}{v_0} = j\omega h \sum_{i=1}^{3} c_i(\rho - \frac{E^{(i)}}{v_0^2}) \tag{2.2}$$

where $E^{(i)}$ is the complex modulus of K and G; $\Delta\gamma$ is the complex propagation factor which has $\frac{\Delta v}{\Delta v_0}$ and $\frac{\Delta\alpha}{k_0}$ as real and imaginary part, respectively. This change is induced by two parts, one (proportional to ρ) caused by kinetic energy relative to the film translation and another (proportional to $E^{(i)}$) caused by potential energy relative to the film strain. Kinetic energy arises from the mass loading mechanism. Therefore, two mechanisms, mass loading and mechanical properties, are often studied together in gas sensors because the reaction or impact of gas molecules can lead to a deformation of the sublayer on the propagation path of the SAW sensors [39, 40]. For the elastic films, elastic properties and the thickness of the sublayer influence the SAW velocity change. Sometimes, it only influences either the operating frequency or phase velocity without magnitude attenuation or with insignificant loss. For example, the operation range of the pressure SAW sensors can be 0-200 kPa [41].

For sensing liquid viscosity, when the concentration of the sample increases, it leads to changes in density and viscosity. The magnitude of Rayleigh waves is a function of the viscosity of the liquid while both its magnitude and phase depend on the acoustic impedance of the liquid [42, 43]. For example, the sensitivity of a low-frequency viscosity SAW sensor (29.7 MHz) is 171.9 Hz (% glycerin) or 5.57 kHz (kg/m$^2\sqrt{}$s) in frequency shifts, 0.09° (% glycerin) or 0.92° (kg/m$^2\sqrt{}$s) in phase difference while that of the high-frequency device (86.1 MHz) is 937.5 Hz (% glycerin) or 37.15 kHz (kg/m$^2\sqrt{}$s) in absolute frequency shifts, 0.37° (% glycerin) or 14.7° (kg/m$^2\sqrt{}$s) in phase difference [42].

2.3.3. RHEOLOGICAL PROPERTIES

THE rheologically-based detection mechanism implies changes in properties of the sensing medium in contact with the piezoelectric surface. For chemical sensing applications, changes in physics properties of the liquid, such as flow, density, viscosity and concentration, which result in attenuation of SAW sensors, are often considered. This attenuation can be caused by both mechanical and electric perturbations [44, 45]. The used mode of the SAW sensors is often shear horizontal mode instead of Rayleigh mode because Rayleigh mode waves are significantly leaky into the liquid medium with the attenuation coefficient larger than the ratio of piezoelectric velocity to liquid velocity. Other physics properties of the liquid medium, such as evaporation or vaporization rate, are also investigated using SAW sensors [30, 46, 47].

2.3.4. ELECTRICAL PROPERTIES

AN electrical field which accompanies propagating waves through the substrate can interact with the mobile charge carriers on the surface. This affects both velocity and amplitude of the waves. Therefore, it is also called acoustoelectric interaction in SAW sensors [39, 48]. For example, the acoustoelectric interaction between electric fields is generated by SAWs and charge carriers in a conductive film. This property is mostly used in telecommunication applications where the carrier waves, as mobile charger carriers, cause perturbations on surface waves. Another example, a conductive thin film SAW sensor is used for sensing conductive gas. The sorption of the water molecules in gas phase on the conductive material makes the film change its electrical conductivity [1]. The magnitude of the acoustoelectric response depends on the electromechanical coupling coefficient K^2, the bulk conductivity σ and the film thickness h. Bilayer structures, such as ZnO/WO_3 on Y-X $LiTaO_3$; or copper, nickel, metal freephthalocyanine layer and palladium film on Y-Z $LiNbO_3$ substrate are utilized for detecting hydrogen [49–51]. This perturbation can result in more attenuation in magnitude than in operating frequency, which is considered a better effect than the mass effect. Another example for uncoated SAW sensors still using this mechanism is humidity sensors. The humidity in ambient condition can affect this electric field through electrical leakage between the electrode pairs.

2.3.5. THERMAL EFFECT

IN general, the velocity of acoustic waves in the piezoelectric media is affected by temperature [1]. The piezoelectric crystals or thin films have high coefficient of thermal expansion. In most practical sensors, temperature influences the acoustic wave velocity on the propagation path [52, 53]. Temperature sensors using SAW technology nowadays have become commercial device without battery [54, 55]. Technically, an electromagnetic wave sent by the interrogator is received and then converted into an acoustic wave. Temperature variations in the environment directly influence physical properties of the acoustic waves propagating along the surface. The modified acoustic waves are transformed back into an electromagnetic waves to be retrieved by the receiver. For another example, a temperature sensor based on the SAW device was proposed for a small volume liquid medium like a droplet. The liquid temperature, heated by the radiated energy of the longitudinal waves, can be measured and controlled by the applied voltage [56]. The operation range of SAW sensors is from 20 to 100^0C [41].

For applications with liquid volumes in the microliter range, there is no deformation of the SAW device and no mobile charge carriers, thus mechanical and electrical properties are not considered here. It is not easy to control the temperature of a large volume liquid medium, so thermal mechanism is also rarely used. Mass loading and rheological property are instead often used and will be considered in this work. Next, we need to identify suitable piezoelectric materials for liquid sensing using SAW devices. In the next section, the main characteristics, advantages and drawbacks of common piezoelectric materials are discussed.

2.4. PIEZOELECTRIC MATERIALS FOR SAW SENSORS

THERE are plenty of materials for piezoelectric applications, such as quartz (SiO_2), lithium tanlalate ($LiTaO_3$), lithium niobate ($LiNaO_3$), PZT (lead titanate $PbTiO_3$ and lead zirconate titanate $Pb[Zr_xTi_{1-x}]O_3$, $0 < x < 1$ known more commonly), zinc oxide (ZnO), and aluminum nitride (AlN) [19]. Depending on operating frequency, samples to be studied, thickness of materials possible, thermal resistance and flexural strength, the most suitable material is selected. For example, quartz, lithium tantalite, lithium niobate and sapphire (Al_2O_3) are often used for bulk piezoelectric devices while PZT, ZnO and AlN are considered as good piezoelectric layers for thin film devices. Although bulk piezoelectric materials are often used for bio- and microfluidics applications based on BAW or SAW technology, they show disadvantages. In fact, most of bulk piezoelectric materials are non-CMOS compatible materials, more complicated to integrate with electronics (needed for control and signal processing); expensive and have a low wave velocity. Piezoelectric thin films are preferred because of being suitable for CMOS-based process fabrication and advanced MEMS technology (deposition on silicon wafer, sputtering, evaporation, photolithography, etc.) [57, 58].

Among the available thin film piezoelectric materials, the most promising for bio/fluidic applications are PZT with its high piezoelectric coefficient, ZnO and AlN, which are CMOS compatible and suitable for mass production, thus reducing costs [59]. They can grow on a variety of substrates, especially bare silicon wafers. The main properties of these materials are shown in Table 2.3. Advantages and disadvantages are briefly discussed below.

Table 2.3: Main properties of common thin-film piezoelectric materials [60, 61].

Material	**PZT**	**ZnO**	**AlN**
Density (g/cm^3)	7.8	5.6	3.3
Modulus (GPa)	61	110-140	300-350
Hardness (GPa)	4-5	15	7-18
SAW velocity (m/s)	4500	6336	5000-6000
Coupling coefficient, k	0.49	0.15-0.33	0.17-0.5
Electromechanical coupling coefficient K^2 (%)	20-35	1.5-1.7	3.1-8

Ceramic PZT, a perovskite crystal structure, is one of the most common piezoelectric materials in acoustic wave devices because it has the highest piezoelectric constant, electromechanical coupling coefficient, density and hardness [19, 58–62]. Another remarkable advantage of the PZT is its ferroelectricity. As its polarization can be reoriented along different directions, PZT does not require a specific step during deposition to obtain alignment of the polarization direction, but needs poling after deposition to achieve a good piezoelectric effect [59]. However, for biosensing and liquid applications, it shows some disadvantages such as higher acoustic wave attenuation, lower sound wave velocities, lower mechanical stability and poorer biocompatibility than ZnO and AlN. Besides, the high temperature sintering and high electric field polarization required, make PZT unsuitable for monolithic integration with electronics [19].

Zinc oxide is a piezoelectric material with a wurtzite-structure with polar direction, which can be grown in thin film form with stable structure, high crystal quality, good stoichiometry, smooth surface, low roughness and uniform structure and thickness. Most of its piezoelectric properties, such as high piezoelectric coupling, high dielectric constant, large transverse piezoelectric coefficient $e_{31,f}$, high quality factor Q and coefficient of thermal expansion are similar to AlN [59]. Being a nonferroelectric film, its grain growth during deposition has to be controlled to obtain the expected polar direction. ZnO is also considered as a biocompatible material and suitable for biomedical applications because of high sensitivity, selectivity of surface to samples and the possibility to immobilize and modify biomolecules on it [59, 61]. However, ZnO shows some limitations. As a semiconductor, any off-stoichiometry in ZnO deposition can drive to increased conductivity. It means high dielectric loss at the low frequency range due to interstitials of the zinc material [59]. Finally, some works reported that it is reactive in air, resulting in an unstable sensor signal [59].

Aluminum nitride, although it is has slightly lower piezoelectric coupling than PZT, is considered as an attractive alternative for its high frequency response, sensitivity and stability [59, 61]. It also offers a better signal to noise ratio (SNR), large output voltage, high thermal conductivity, good electrical isolation, wide band gap and high thermal expansion coefficient [61]. In addition, AlN has all advantages offered by ZnO in bio- and microfluidics applications. The Rayleigh wave velocity of ZnO is smaller than AlN, especially c-plane AlN. The operating frequency of ZnO is also smaller than that of AlN [63]. Finally, AlN is considered a harder material, with very large volume resistivity and the most compatible piezoelectric material with microelectronic CMOS processes. One concern (or point of attention) is that AlN has a stronger internal stress which can lead to rather critical microcracking [63].

Considering the physical and chemical properties of AlN and the possibility to integrate these films in a silicon based manufacturing process, AlN is a promising material for active, passive bio- microfluidics applications, in bulk and thin film structure. The rest of this chapter will focus on the morphologic and piezoelectric properties of thin films of AlN deposited by RF sputtering.

2.4.1. ALN THIN FILMS

ALN thin films can be deposited by reactive evaporation, molecular beam epitaxy (MBE), pulsed lased deposition (PLD), chemical vapour deposition (CVD), and sputtering [61, 64]. MBE was first used for the AlN deposition in 1980s [65] and then further developed in 1990s [66, 67]. It can grow a single-crystal epitaxial AlN film. However, this method has a low growth rate, requires an expensive equipment and extremely higher temperature (up to 950^0C) than others methods [66, 68]. CVD, including metal organic chemical vapor deposition (MOCVD) or plasma-enhanced chemical vapor deposition (PECVD), is considered as a better solution for AlN thin film deposition at lower temperature, with high-qualify crystallinity [68]. However, the temperature is still higher than what desirable for CMOS compatible processes [61]. PLD is a better solution for depositing AlN thin films on other substrates, like Si or sapphire, at temperature between 300 – 750^0C [69, 70]. Another issue is the residual compressive stress due to the oxygen incorporation and the substrate temperature lower than that of the target during deposition

[71]. This stress appears when the AlN thin film is deposited at 600^0C, on high resistivity silicon wafers.

Sputtering is a physical vapor deposition (PVD) process where atoms of the solid target are rejected by the bombardment of accelerated ions and impact energetically on the substrate. When a chemical reaction happens between atoms from the target and reactive gases inside the sputtering chamber before coating the substrate, the process is referred to as reactive sputtering. Reactive magnetron sputtering is a better method for the deposition of AlN thin films over a large area and at lower temperatures (25 – 500^0C) [61, 71, 72]. Thanks to the magnets, electrons are trapped towards the cathode region and more ionizing collisions lead a higher deposition rate.

The reactive sputtering deposition provides films with a fairly smooth surface, uniform grain size, stable and reproducible quality. It is a commonly used technique in CMOS processing, thus largely available and suitable for large volume manufacturing [64, 72, 73]. Moreover, it uses lower deposition temperature (25-500^0C), provides higher deposition rates and lower residual stress than other methods. The best deposition method of AlN thin film (crystallizes in a hexagonal wurtzite structure) uses both RF and pulsed-direct current (DC) reactive sputtering deposition on bare silicon wafers [61].

In this study, a pulsed Trikon Sigma DC magnetron sputtering reactor is used for depositing AlN thin film in TUD-EKL lab. Using the reactive sputtering mode, the power, with the frequency of 250 kHz and pulse width of 1616 ns, was used and the value can be set up to 3 kW. As known, AlN deposition by sputtering is affected by nitrogen concentration, plasma pressure, temperature, and sputtering power [72]. Two recipes, shown in Table 2.4, are tested to evaluate piezoelectric quality and uniformity of AlN thin films through the performance of SAW devices fabricated using these films.

Before sputtering AlN thin films, the native oxide layer on the top of the bare silicon is removed by a quick radio frequency (RF) etching step in the same sputtering system. During the long sputtering deposition for the 1 µm upper AlN layer, gas molecules, like argon (Ar^+) and nitrogen (N_2), can be incorporated inside the layer. A short annealing is a good way to release them from the film. For thicker AlN films (more than 1 µm), an extra cleaning step of the chamber between deposition steps has been employed to avoid this inclusion, however this can affect the uniformity of the piezoelectric characteristic of the layer, for example non-uniform grains on image of 2-µm AlN film as shown in Fig 2.7.

Table 2.4: The main parameters for AlN thin film deposition by pulsed DC sputtering method.

Parameter	**Substrate temperature** (^{0}C)	**Sputtering power** (kW)	**Platen RF power** (W)	**Argon (Ar^+)** (sccm)	**Nitrogen (N_2)** (sccm)
Recipe 1	50	1	0	19	38
Recipe 2	400	3	40	20	80

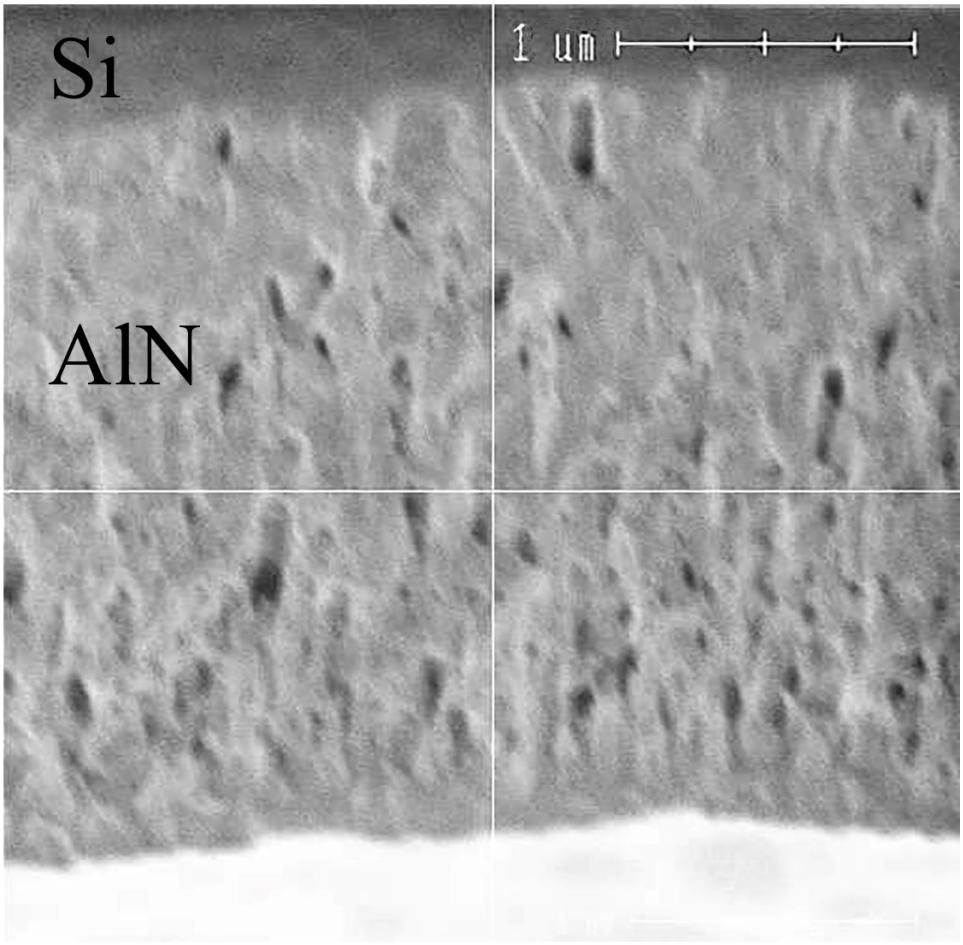

Figure 2.7: Cross-sectional SEM image of a 2-µm AlN film on bare silicon with intermediate cleaning steps.

2.4.2. TEST SAW DEVICES

To evaluate the quality of the AlN sputtered films, we investigate the insertion loss of SAW devices fabricated by the recipes above with and without an extra cleaning step during deposition, and the attenuation of the SAW signal on the propagation path for films deposited on bare silicon wafers with different resistivity.

The SAW device used for this test includes 50 x 50 pairs of input and output Al IDT fingers (see Fig 2.8), which was repeated twelve times on the wafer. It only consists of three layers (Al/SiN/AlN) deposited on bare silicon wafers. Al electrodes are chosen because of the low resistivity, low acoustic impedance, and high Q factor. Therefore, the theoretical operating frequency is 126.7 MHz when the velocity is about 5068 m/s.

The measured data is reported in Fig 2.9 For a 1-µm AlN film sputtered with recipe 1 (the lower substrate temperature and gas rate of N_2/Ar), the magnitude fluctuation of

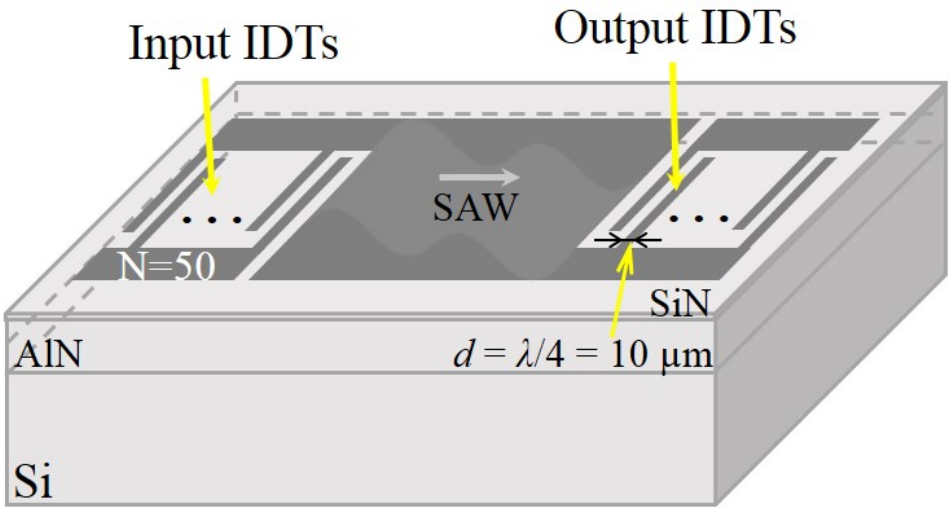

Figure 2.8: Schematic drawing of the test SAW device with the pitch (the finger width) d = 10 µm.

the insertion loss S_21 is weaker than that of 0.5 and 1 µm AlN films sputtered by recipe 2. From the data in Fig 2.9, it is clear that when the grains of AlN thin film are not grown continuously, the signal is slightly weaker. For the SAW device with 1-µm AlN film sputtered by recipe 2 (see Fig 2.9d), the cleaning step after depositing 0.5 µm AlN was performed. Only five dies among the tested twelve dies of the whole wafer have an output signal as expected.

Fig 2.10 shows the insertion loss of SAW devices fabricated with different thickness of AlN thin films. For a 1 µm AlN thin film SAW device, the best signal was measured because of two reasons. Firstly, as mentioned before, the penetration depth of the SAWs into the substrate is inversely proportional to the operating frequency and the energy is concentrated mostly in half wavelength close to the surface, so the SAW device with the thinner AlN film can have a weaker signal. However, in practice, the SAW device with the thicker (2 µm) AlN film is worse than the 1 µm AlN film. The reason is that the longer reactive sputtering process negatively influences the AlN quality due to residual particles from the target or abundant gases stagnant on the AlN layers. To remove these particles, we tried both a final annealing and a cleaning step after each 1 µm of deposition. However, these make the signal of the SAW weaker because the grain growth of the AlN film is interrupted as shown in plots (a) and (b) of Fig 2.10 and visible in Fig 2.7.

AlN thin film sputtered on low resistivity silicon wafers using recipe 2 result in stable and smooth layers. The higher sputtering temperature requires a shorter deposition time. Fig 2.11 shows AFM images of a 1 µm x 1 µm area, indicating an average roughness of 37 nm.

Besides the grain uniformity and the surface smoothness, other parameters evaluated are residual stress, and piezoelectric coefficients. Piezoelectric characteristic de-

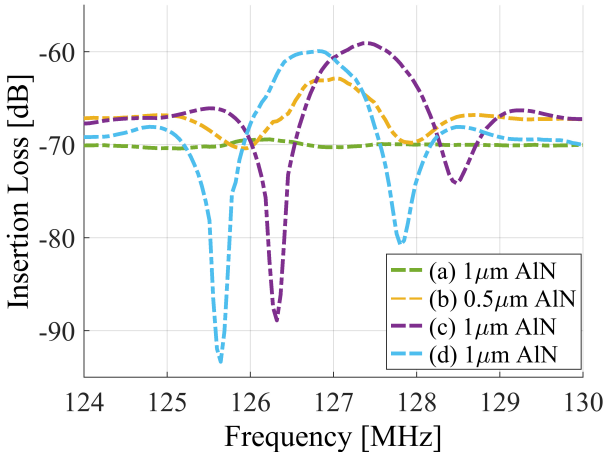

Figure 2.9: AlN thin films of different thickness and sputtered at different temperatures (a) 50^0C (recipe 1), (b), (c) and (d) 400^0C (recipe 2). The (c) AlN sample is sputtered continuously whereas the (d) film is sputtered discontinuously and interrupted by the extra cleaning step for the target.

pends on the resistivity of the bare silicon wafer. When AlN thin film is sputtered on the high resistivity wafer, the SAW signal is stronger because the longitudinal and transverse coefficient d_{33} and d_{31} are larger [73, 74]. However, sputtering AlN thin film on the high resistivity wafer increases the stress in the layer. The results of sputtering different thickness of AlN thin films on different wafers are shown in Table 2.5. The thicker AlN films suffer from larger compressive stress.

Table 2.5: Stress measurement by Tencor Flexus stress meter.

Type of silicon	**AlN thickness** (nm)	**Radius**[2] (µm)	**Bow**[3] (µm)	**Stress** (MPa)
P-type <100>(1 – 5 Ω.cm)	933 ± 13	30.8	- 26.2	100.8
P-type <100>(1 – 5 Ω.cm)	933 ± 13	30.8	- 26.2	100.8
P-type <100>(1 – 5 Ω.cm)	2812 ± 47	17.0	- 45.4	227.4
P-type <100>(>500 Ω.cm)	950 ± 14	69.2	-13.5	68.8
P-type <100>(>500 Ω.cm)	6000	3.5	- 235.2	
P-type <100>(>1000 Ω.cm)	898.8 ± 13	124.3	- 15.0	45.6
P-type <100>(>1000 Ω.cm)	1884.5 ± 27	32.2	- 35.5	152.2
P-type <100>(>1000 Ω.cm)	2819.4 ± 42	14.3	- 57.7	234.4

The piezoelectric quality of AlN thin film deposited by sputtering on the higher resistivity wafer is better as indicated by the piezoelectric coefficient d_{33}, a longitudinal

[2] Radius of the substrate curvature after deposition.
[3] Bow of the substrate after deposition.

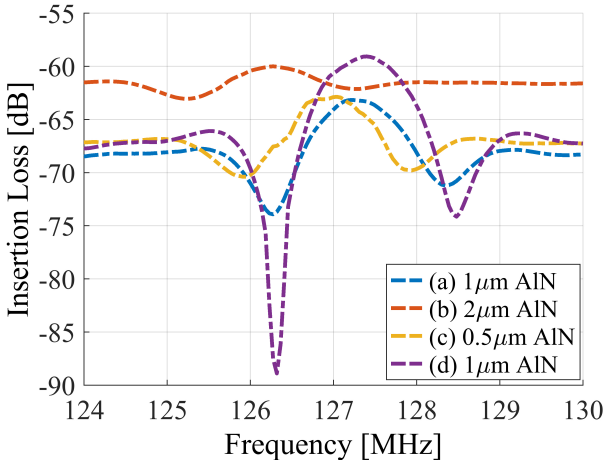

Figure 2.10: AlN thin films with different thickness sputtered on (a), (b) silicon wafer resistivity >500 Ω.cm, (c), (d) silicon wafer resistivity >1000 Ω.cm.

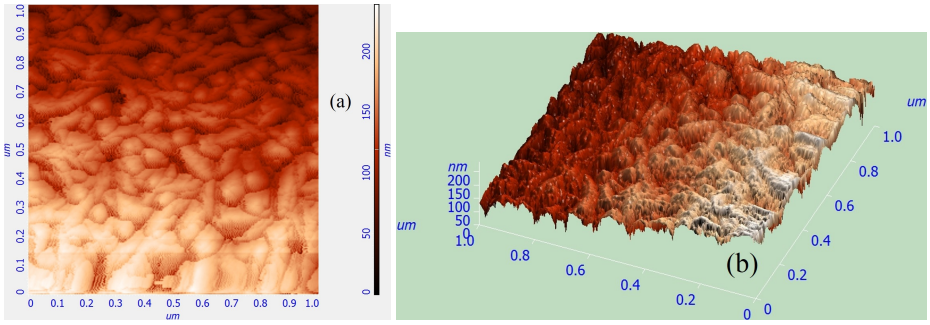

Figure 2.11: AFM images of the top surface of the AlN thin film on bare silicon (P-type <100> (1 – 5 Ω.cm)) in (a) 2 dimensions and (b) 3 dimensions.

coefficient, which evaluates magnitude of the Rayleigh component of the SAW beam propagating on the AlN thin film, which is higher[75]. Measurements of the piezoelectric characteristics are performed in piezoresponse force microscopy (PFM) mode with a commercial AFM (NTEGRA PRIMA NT-MDT AFM). A conductive AFM tip (CSG11/Pt) in contact interaction mode is used to evaluate the piezoelectric characteristic of the AlN layer. An effective longitudinal piezoelectric constant d_{33} is measured by the tip deflection signal sent to a lock-in amplifier. Amplitude A and phase φ of the normal oscillation are with respect to the vertical piezoresponse as shown in Fig 2.12. A bias voltage of 10 V is applied to the 1 µm x 1 µm area between the bottom electrode and the SPM tip, and the piezoresponse $A\cos\varphi$ is studied in the bias voltage range from -10 to 10 V. This AFM spectroscopy data of AlN films on silicon wafers with the different resistivity is obtained by the bias voltage excitation as shown in Fig 2.12. For AlN thin films on the higher resistivity silicon wafer, signal variations of the amplitude, phase and piezoresponse are more

pronounced. The strongest piezoresponse belongs to the 1 µm AlN film on the highest resistivity wafer.

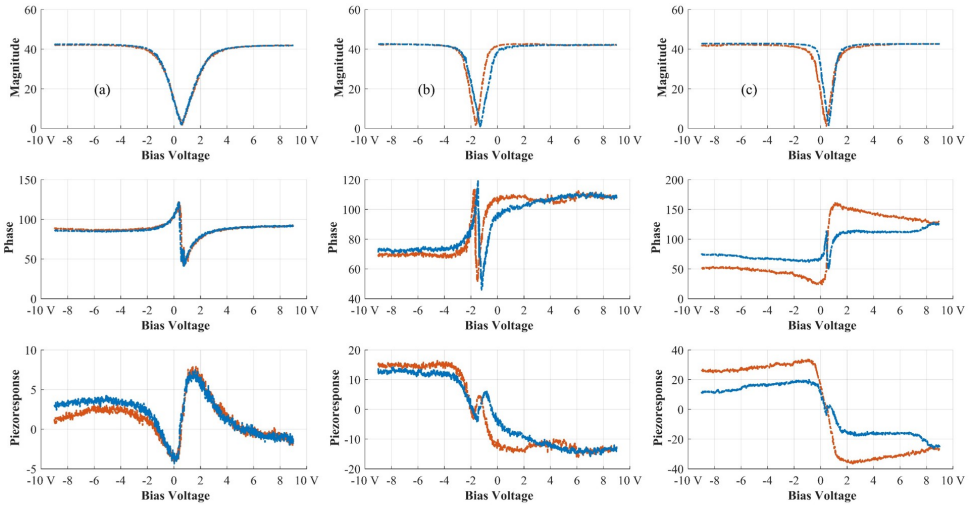

Figure 2.12: PFM spectroscopy curves: vertical PFM amplitude, phase, and piezoresponse versus bias voltage. They are measured on AlN thin films on bare silicon wafer with resistivity of (a) 1 – 5 Ω.cm, (b) 10 – 20 Ω.cm and (c) 1000 – 104 Ω.cm. An electric excitation of 10 V at 51 kHz was applied to all samples. The bias sweep originated in the left corner follows the red trace, while the blue trace is for the reverse sweep.

2.5. MODELLING SAW DEVICES

MODELING M SAW devices is needed to determine the major parameters and suitable dimensions, namely size, shape, number of the finger pairs, finger width and spacing, delay line distance, and mode of wave propagation, for the design definition. It is also possible to have an initial evaluation of internal (topography of SAW devices) or external (liquid or gas samples, additional film or environment) effects on the device [76, 77].

There are several analytical modeling methods for SAW devices, such as impulse response model [78], delta function model [79], the crossed-field and in-line equivalent circuit models [80, 81], the coupling-of-mode (COM) model [82] or conventional P-matrix model, angular spectrum of wave models [21] and finite element method (FEM) model [83].

The impulse response model and delta function model are the earliest and basic modeling techniques of SAW devices. The impulse response model is known as an approach for transducers where IDT arrays are assumed to have a constant aperture, spacing and finger width as shown in Fig 2.13. The main aim is to analyze baselines such as frequency response, loss, admittance, and parameters for the circuit simulation of SAW devices [78, 83]. This first order model can show mechanical and electrical character-

istics of the SAW device in general. However, if the layered-structure SAW filter has a velocity dispersion, the equation of the null frequency band width is not suitable. This method is only valid for symmetrical designs of SAW devices [80]. Although for the delta function model, an impedance level and second order effects of the SAW devices are not considered [82], it still provides relevant information about bandwidth, insertion loss, rejection level, and side lobes.

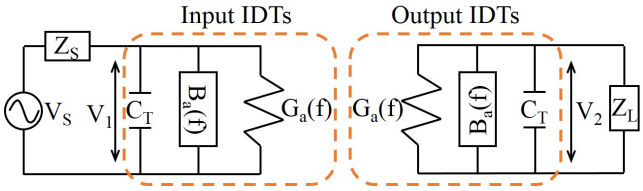

Figure 2.13: Circuit model based on the impulse response method where C_T is the transducer capacitance, $B_a(f)$ is the acoustic susceptance, and $G_a(f)$ is the radiation conductance.

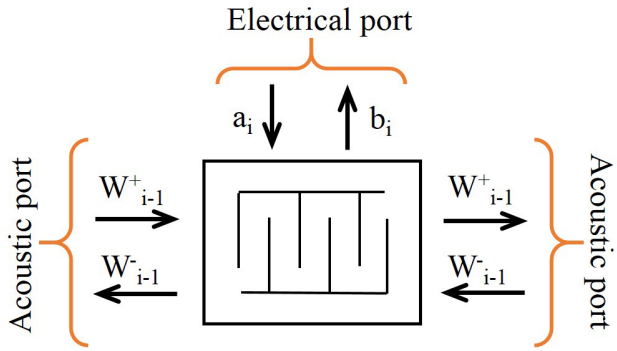

Figure 2.14: Mason equivalent circuit based on P-matrix method for an IDT array.

For the COM model, various wave phenomena in periodic structures are shown clearly, such as electromagnetic waves in periodic grating, ultrasonic and optical waves in multi-layered media and so on. It provides parameters for the next P-matrix model like velocity, reflectivity, attenuation, transduction coefficient and capacitance. The conventional P-matrix, the first model describing IDT arrays, is equivalent to a three-port network with two acoustical ports and a third electrical port as shown in Fig 2.14 [82, 83]. After that, this conventional method was extended to obtain more accurate results and called equivalent circuit model. The matrix of the SAW device in general can be given by the multiplication of the matrices for input and output IDTs and the delay line or space between IDT arrays by:

$$[SAW(f)] = [IDT_{in}(f)].[D(f)].[IDT_{out}(f)] \tag{2.3}$$

Therefore, it is considered as the best option to analyze transmission of the SAW devices in the equivalent circuit model, which accounts for mechanic and electric proper-

ties of devices such as wave velocity, electromechanical coupling coefficient, operating frequency, and number of electrode pairs. A more recent method for modeling SAW devices is a FEM, a combination of COM and equivalent circuit model.

2.5.1. FINITE ELEMENT MODEL

THE finite element model is a numerical solution method for one layer or multilayer SAW devices. Like the above mentioned methods, it is also based on the major dimensions of the IDT structures (number of fingers, finger width, aperture, and shape) to obtain frequency response and impedance. This model shows the relations among mechanical and electrical variables. These relations are between strain – stress, stress – displacement, displacement – electric field, electric field – strain, through elasticity, direct piezoelectric effect, permittivity and converse piezoelectric effect [1]. From equations of the elastic constitutive and piezoelectric constitutive relations, general equations about wave displacement components $u_i(x, y, z, t)$ and electrical potential $\phi(x, y, z, t)$ are given by [1]:

$$\sum_{i,j,k=1}^{3} c_{ijkl} \frac{\partial^2 u_l}{\partial x_k \partial x_j} + \sum_{j,k=1}^{3} e_{ijk} \frac{\partial^2 \phi}{\partial x_k \partial x_j} = \rho \frac{\partial^2 u_i}{\partial t^2} \tag{2.4}$$

$$\sum_{i,k,l=1}^{3} e_{ikl} \frac{\partial^2 u_l}{\partial x_k \partial x_i} - \sum_{i,k=1}^{3} \varepsilon_{ik} \frac{\partial^2 \phi}{\partial x_k \partial x_i} = 0$$

where c_{ijkl}, e_{ikl}, ε_k, ρ are the elastic tensor, the piezoelectric tensor, the dielectric tensor and the mass density of the piezoelectric material, respectively. Advantages of the FEM model are the modeling of arbitrary geometries for undisturbed SAW propagation and even excitation, detection and scattering of mechanical and electrostatic problems of the SAW during the experiment. Unlike other methods, mechanical and electrical field varied at the boundary of layers, wave velocity, displacement components and electromechanical coupling factor are considered and analyzed as well. The FEM model provides a good first evaluation for designing SAW devices because of the presence of both acoustic and electric properties to acoustoelectric interaction. It is also the most common numerical model for design, calculation and analysist of SAW devices in 3D domain and commercial simulation software like COMSOL, ANSYS and Convertor is available [82, 84].

2.5.2. 3D SAW MODELING

TO understand the acoustoelectric interactions that take place on the piezoelectric material and closely investigate different topographies of IDTs and the corresponding SAW response, COMSOL software with FEM analysis is used to model the SAW device. In COMSOL software, the simulation for SAW devices can be performed by electromechanical or magnetomechanical transduction.

The structure proposed in this study is a typical in-output IDT array with a microhole in the middle of the propagation path. This microhole can be filled of liquids with different properties, water in this example. A 3D model of the SAW device has defining parameters and is meshed as shown in Fig 2.15. This device based on aluminum nitride (AlN) can be simulated by Multiphysics (solid mechanics and electrostatic) in

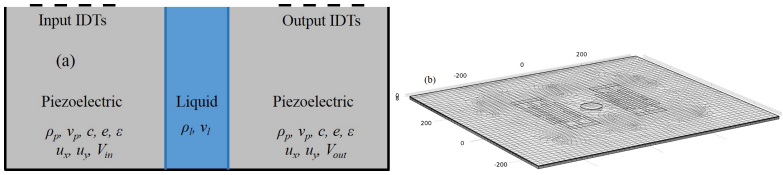

Figure 2.15: (a) 2D SAW device with the microhole. SAWs generated by the input transducer travel in $+x$ direction and through the piezoelectric medium and the liquid medium. For the piezoelectric medium, density (ρ_p), SAW velocity (v_p), elasticity matrix (c), coupling matrix (e), and relative permittivity matrix (ε) are constants whereas density (ρ_l) and sound velocity (v_l) are constants for the liquid medium (see Appendix-A: Parameters of piezoelectric and some liquids). At the contact between the two media, Rayleigh component of SAWs is attenuated with the absorption coefficient $\alpha = \frac{\rho_l v_l}{\rho_p v_p \lambda}$ (parameters see Appendix-A: Parameters of piezoelectric and some liquids); and (b) meshed SAW model.

COMSOL. Components of the piezoelectric device are simplified and the piezoelectric effect is induced by the coupled interface between electric and solid mechanic domain. Multiphysics component is a solution for configuration of the expected acoustic wave mode and electrical and mechanical conversion of the piezoelectric characteristics. The used mode is here Rayleigh damping on the piezoelectric material. The wave velocity on the aluminum nitride is calculated as 5049 m/s. The parameters used for modeling the SAW device are given in Table 2.6. A sine voltage of 10 V is applied to the input IDTs. The edges of the piezoelectric substrate are setup as a low-reflecting boundary to avoid the reflected waves as shown in Fig 2.16. In FEM calculations, all parameters and characteristics of the considered materials, like the elastic tensor, the piezoelectric tensor, the dielectric tensor and the mass density as well as pseudo number of IDT pairs and mesh can be modified and simplified.

Table 2.6: Simulation parameters and device dimensions.

Substrate	**Electrode pairs** (N)	**Electrode width** (d)	**Wavelength** (λ)	**Depth** (h)	**Aperture** (A)	**Microhole** (D)
AlN	3	10 µm	40 µm	8 µm	150 µm	50 µm in diameter

In the case of this study, when the incident waves from the piezoelectric media travel to the microhole, there are two types of losses, attenuation by Rayleigh component of SAWs and frictional loss. The Rayleigh component and density changes between two media cause an emission whereas the transversal component leads to frictional loss determined by the viscosity of the liquid medium. At the studying frequency of 126 MHz, the frictional loss is much smaller than the attenuation by Rayleigh component, thus it is not often considered in calculation of interaction between the liquid and the piezoelectric media [84–86]. SAWs traveling through liquid medium are attenuated by the absorption coefficient α of 1.35 dB/cm. When the size of the hole equals to 1/3 the size

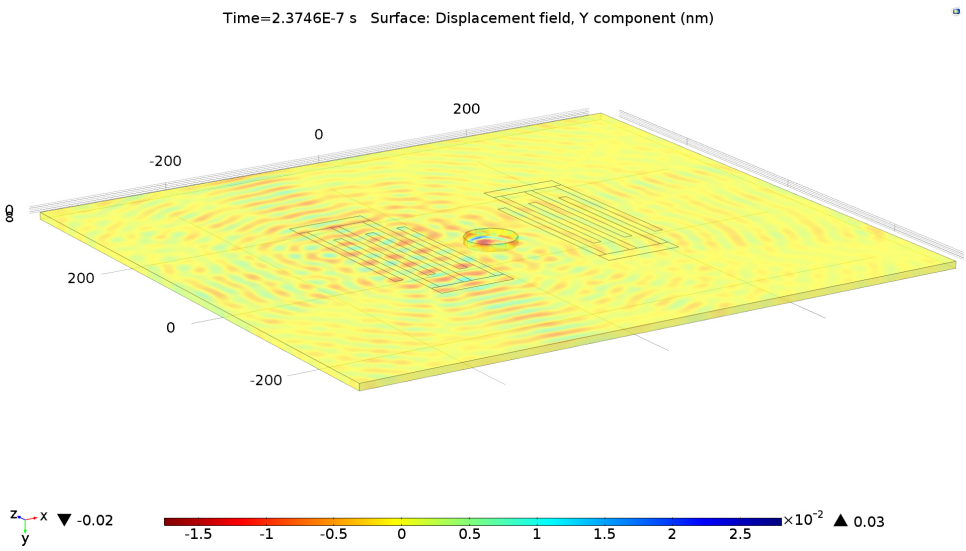

Figure 2.16: Y-component displacement of SAWs at time t = 237 ns.

of the SAW aperture, the output voltage of the SAW device with water inside the hole is reduced 10 times compared to the one without the hole as shown in Fig 2.17. When the density of the assumed liquid is double to water inside the hole, its output signal is smaller than that of the water.

2.6. CONCLUSION

THIS chapter gives a general view of the acoustic wave devices used for bio- microfluidics applications and motivates our choice for SAW devices. Detection mechanisms of the SAW devices are often used for sensing liquid. Aluminum nitride thin film is chosen as an attractive promising material for SAW applications due to the good material properties, compatibility with the microelectronic process, high acoustic velocity and high electromechanical coupling coefficient. From a dedicated investigation of the process parameters and substrate, AlN layers with a thickness of 1 µm, sputtered on high-resistivity silicon wafers were selected as they offer the best quality of piezoelectric characteristics and the strongest fluctuation in insertion loss.

The equivalent circuit model of the SAW device is a quick design in 2D and has been used for the transmission of IDT arrays and the delay line into the scattering matrix. It is also used for modeling obstacles on the delay line which generates attenuation in phase, magnitude or frequency shift. The FEM model is a common way for expanding the design in 3D and explaining better the relations among mechanical and electrical variables. In this thesis, FEM (with commercial COMSOL software) was used for designing and simulating novel SAW devices and configurations to observe acoustic wave generation and signal response of these SAW devices.

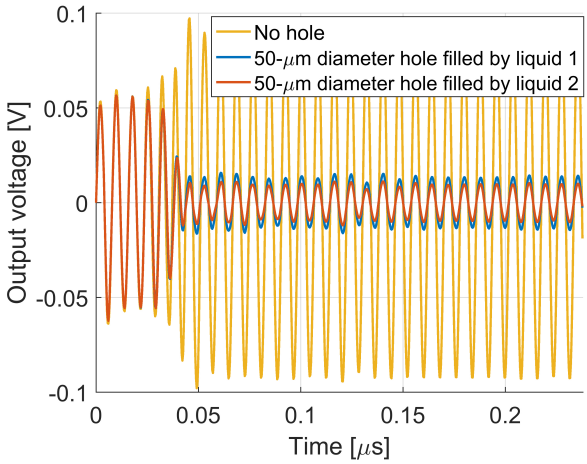

Figure 2.17: Output voltages of the SAW device with and without the hole in the middle of the propagation path. Liquid 1 is water with density ρ while liquid 2 is another liquid with the density 2ρ.

REFERENCES

[1] J. Ballantine, R. M. White, S. I. Martin, A. J. Ricco, E. T. Zellers, G. C. Frye, and et al., *Acoustic Wave Sensors, 1st Edition: Theory, Design, & Physico-Chemical Applications* (USA: ACADEMIC PRESS, 1997).

[2] K. Lange, B. E. Rapp, and M. Rapp, *Surface acoustic wave biosensors: a review,* Analytical and Bioanalytical Chemistry (2008).

[3] R. M. Lec, *Piezoelectric biosensors: recent advances and applications,* in *Proceedings of the 2001 IEEE International Frequency Control Symposium and PDA Exhibition* (2001).

[4] V. Ferrari and R. Lucklum, *Overview of acoustic-wave microsensors,* (Berlin, Heidelberg: Springer Berlin Heidelberg, 2008) Chap. Piezoelectric Transducers and Applications, pp. 39–62.

[5] N. G. Durmus, R. L. Linb, M. Kozberg, D. Dermici, A. Khademhosseinie, and U. Demircie, *Encyclopedia of microfluidics and nanofluidics,* (Springer New York, 2015) Chap. Acoustic-Based Biosensors.

[6] K. Yamanouchi, Y. Wagatsuma, K. Aoki, and T. Tsuji, *10 ghz-range surface acoustic wave inter-digital transducers and low loss filters using anodic oxidation technology,* in *Proceedings of 1996 IEEE International Frequency Control Symposium* (1996).

[7] R. Brunig, A. Winkler, G. Guhr, and H. Schmidt, *Active mixing in microfluidic systems using surface acoustic waves,* in *2011 IEEE International Ultrasonics Symposium* (2011).

[8] W. G. David, R. S. Patrick, A. V. Kevin, and D. M. Russell, *Surface acoustic wave microsensors and applications,* Smart Materials and Structures (1997).

[9] T. Yanagitani, *Microdevices to helioseismology,* (intechopen, 2011) Chap. Shear Mode Piezoelectric Thin Film Resonators, Acoustic Waves.

[10] A. V. Mamishev, K. Sundara-Rajan, Y. Fumin, D. Yanqing, and M. Zahn, *Interdigital sensors and transducers,* in *Proceedings of the IEEE* (2004).

[11] M. Thompson, A. L. Kipling, W. C. Duncan-Hewitt, L. V. Rajakovic, and B. A. Cavic-Vlasak, *Thickness-shear-mode acoustic wave sensors in the liquid phase. a review,* Analyst (1991).

[12] G. Wingqvist, *Thin film electroacoustic devices for biosensor applications*, Ph.D. thesis, Uppsala Universite (2009).

[13] G. Sauerbrey, *Zeitschrift fur physik,* (1959) Chap. Verwendung von Schwingquarzen zur Wagung dunner Schichten und zur Mikrowagung.

[14] W. H. King, *Piezoelectric sorption detector,* Analytical Chemistry (1964).

[15] M. Thompson, C. L. Arthur, and G. K. Dhaliwal, *Liquid-phase piezoelectric and acoustic transmission studies of interfacial immunochemistry,* Analytical Chemistry (1986).

[16] J. Weber, W. M. Albers, J. Tuppurainen, M. Link, R. Gabl, W. Wersing, and M. Schreiter, *Shear mode fbars as highly sensitive liquid biosensors,* Sensors and Actuators A: Physical (2006).

[17] M. Nirschl, A. Rantala, K. Tukkiniemi, S. Auer, A.-C. Hellgren, D. Pitzer, and et al., *Cmos-integrated film bulk acoustic resonators for label-free biosensing,* Sensors (Basel, Switzerland) (2010).

[18] Y. Q. Fu, J. K. Luo, N. T. Nguyen, A. J. Walton, A. J. Flewitt, X. T. Zu, and et al., *Advances in piezoelectric thin films for acoustic biosensors, acousticfluidics and lab-on-chip applications,* Progress in Materials Science (2017).

[19] M. I. Rocha-Gaso, C. March-Iborra, A. Montoya-Baides, and A. Arnau-Vives, *Surface generated acoustic wave biosensors for the detection of pathogens: A review,* Sensors (Basel, Switzerland) (2009).

[20] F. Martin and P. Muralt, *Aln thin film as waveguide for shear acoustic waves,* Applied Physics Letters (2006).

[21] D. Morgan, *Surface Acoustic Wave Filters: With Applications to Electronic Communications and Signal Processing* (Elsevier Ltd., 2007).

[22] P. Selmeier, R. Grunwald, A. Przadka, H. Kruger, G. Feiertag, and C. Ruppel, *Recent advances in saw packaging,* in *2001 IEEE Ultrasonics Symposium* (2001).

[23] E. Benes, M. Groschl, F. Seifert, and A. Pohl, *Comparison between baw and saw sensor principles,* in *Proceedings of International Frequency Control Symposium* (1997).

[24] B. Drafts, *Acoustic wave technology sensors,* IEEE Transactions on Microwave Theory and Techniques (2001).

[25] C. M. Harris, *Product review: Seeing saw potential,* Analytical Chemistry (2003).

[26] J. P. Smith and V. Hinson-Smith, *The new era of saw devices,* Analytical Chemistry (2006).

[27] Y. Tang, Z. Li, J. Ma, L. Wang, J. Yang, B. Du, and et al., *Highly sensitive surface acoustic wave (saw) humidity sensors based on sol_gel sio2 films: Investigations on the sensing property and mechanism,* Sensors and Actuators B: Chemical (2015).

[28] C. Wen-Yang, L. Yu-Cheng, K. Wen-Wang, N. Hsiao-Lung, and S. Po-Hsun, *Phase detection of the two-port fpw sensor for biosensing,* in *2005 IEEE Engineering in Medicine and Biology 27th Annual Conference* (2005).

[29] J. Kondoh, M. Yamada, and K. Sugiura, *Novel measurement method of position and sound velocity of a liquid droplet using a surface acoustic wave device,* in *2016 IEEE SENSORS* (2016).

[30] P. Kostial, *Surface acoustic wave measurements of evaporation rate,* Applied Acoustics (1996).

[31] S. Showko and K. Jun, *Surface acoustic wave sensors,* Japanese Journal of Applied Physics (2004).

[32] S. J. Martin, A. J. Ricco, T. M. Niemczyk, and G. C. Frye, *Characterization of sh acoustic plate mode liquid sensors,* Sensors and Actuators (1989).

[33] J. Wei, P. M. Sarro, and T. C. Duc, *A piezoresistive sensor for pressure monitoring at inkjet nozzle,* 2010 IEEE sensors (2010).

[34] N. Blaz, A. Mari, S. Toskov, G. Miskovic, G. Radosavljevi, and L. Zivanov, *Capacitive sensor for quantity detection of known liquid present in distilled water,* in *International Spring Seminar on Electronics Technology 37th* (2014).

[35] S. Semenov, V. Starov, and R. G. Rubio, *Droplet wetting and evaporation,* (Oxford: Academic Press, 2015) Chap. Chapter 21 - Droplets with Surfactants A2, pp. 315–337.

[36] K. Bodenhofer, A. Hierlemann, G. Noetzel, U. Weimar, and W. Gopel, *Performances of mass sensitive devices for gas sensing: Thickness shear mode and surface acoustic wave transducers,* Analytical ChemistryAnalyAnalytical Chemistrytical Chemistry (1996).

[37] G. Feuillard, Y. Janin, F. Teston, L. Tessier, and M. Lethiecq, *Sensitivities of surface acoustic wave sensors based on fine grain ceramics,* in *Quality Measurement: The Indispensable Bridge between Theory and Reality. 1996 IEEE Instrumentation and Measurement Technology Conference and IMEKO Tec* (1996).

[38] S. Subhashini and A. V. Juliet, *Computer networks & communications (netcom): Proceedings of the fourth international conference on networks & communications,,* in *Computer Networks & Communications (NetCom): Proceedings of the Fourth International Conference on Networks & Communications*, edited by N. Chaki, N. Meghanathan, and D. Nagamalai (Springer New York, 2013) Chap. CO2 Gas Sensor Using Resonant Frequency Changes in Micro-Cantilever.

[39] N. M. Tashtoush, *SAW HUMIDITY SENSOR AND AN ENVIRONMENTAL ELECTRONIC NOSE SYSTEM*, Ph.D. thesis, Physics Concordia University (1996).

[40] Z. Liron, N. Kaushansky, G. Frishman, D. Kaplan, and J. Greenblatt, *The polymer coated saw sensor as a gravimetric sensor,* Analytical Chemistry (1997).

[41] T. Li, H. Hu, G. Xu, K. Zhu, and a. L. Fang, *Acoustic waves,* (IntechOpen, 2010) Chap. Pressure and Temperature Microsensor Based on Surface Acoustic Wave in TPMS.

[42] B. Yildirim, S. U. Senveli, R. W. R. L. Gajasinghe, and O. Tigli, *Surface acoustic wave viscosity sensor with integrated microfluidics on a pcb platform,* IEEE Sensors Journal (2018).

[43] M. Takeshi, S. Mitsunori, and K. Jun, *Measurements of standard-viscosity liquids using shear horizontal surface acoustic wave sensors,* Japanese Journal of Applied Physics (2009).

[44] J. Kondoh, Y. Okiyama, S. Mikuni, Y. Matsui, H. Yatsuda, and M. Nara, *Development of sh-saw sensing system for liquids,* in *Frequency Control Symposium, 2007 Joint with the 21st European Frequency and Time Forum. IEEE International* (2007).

[45] J. Kondoh, T. Muramatsu, T. Nakanishi, Y. Matsui, and S. Shiokawa, *Development of practical surface acoustic wave liquid sensing system and its application for measurement of japanese tea,* Sensors and Actuators B: Chemical (2003).

[46] J. Devkota, P. Ohodnicki, and D. Greve, *Saw sensors for chemical vapors and gases,* Sensors (2017).

[47] T. Bui, B. Morana, A. Tran, T. Scholtes, T. C. Duc, and a. P. M. Sarro, *Saw device for liquid vaporization rate and remaining molecule sensing,* in *IEEE-SENSORS2015* (2015).

[48] T. Xie and B. M. Wilamowski, *Fundamentals of industrial electronics,* (CRC Press, Taylor & Francis Group, 2011) Chap. Physical Phenomena Used in Sensors.

[49] S. J. Ippolito, S. Kandasamy, K. Kalantar-Zadeh, and W. Wlodarski, *Layered saw hydrogen sensor with modified tungsten trioxide selective layer,* Sensors and Actuators B: Chemical (2005).

[50] S. J. Ippolito, S. Kandasamy, K. Kalantar-Zadeh, A. Trinchi, and W. Wlodarski, *A layered surface acoustic wave zno/litao3 structure with a wo3 selective layer for hydrogen sensing,* Sensor Letters (2003).

[51] W. P. Jakubik and M. W. Urbanczyk, *Saw hydrogen sensor with a bilayer structure based on interaction speed,* Sensors and Actuators B: Chemical (2005).

[52] Z. Liron, J. Greenblatt, G. F. N. Gratziani, and A. Biran, *Temperature effect and chemical response of surface acoustic wave (saw) single-delay-line chemosensors,* Sensors and Actuators B: Chemical (1993).

[53] E. T. Zellers and M. Han, *Effects of temperature and humidity on the performance of polymer-coated surface acoustic wave vapor sensor arrays,* Analytical Chemistry (1996).

[54] SENSeOR, *New Wireless SAW Temperature Sensors without Battery*, Tech. Rep. (http://www.sensorsportal.com, 2013).

[55] Sengenuity, *Wireless SAW Temperature Sensor System*, Tech. Rep. (Sengenuity).

[56] J. Kondoh, N. Shimizu, Y. Matsui, M. Sugimoto, and S. Shiokawa, *Development of temperature-control system for liquid droplet using surface acoustic wave devices,* Sensors and Actuators A: Physical (2009).

[57] Y. Q. Fu, J. S. Cherng, J. K. Luo, M. P. Y. Desmulliez, A. J. Walton, Y. Li, and a. F. Placido, *Acoustic waves,* (2010) Chap. Aluminium Nitride thin Film Acoustic Wave Device for Microfluidic and Biosensing Applications.

[58] T. Hdiji, H. Mnif, and M. Loulou, *Future trends of saw filters,* in *3rd International Design and Test Workshop* (2008).

[59] N. Bassiri-Gharb, *Piezoelectric and acoustic materials for transducer applications,* (Springer-Verlag US, 2008) Chap. Piezoelectric MEMS: Materials and Devices.

[60] P. Dineva, D. Gross, R. Muller, and T. Rangelov, *Dynamic fracture of piezoelectric materials: Solution of time-harmonic problems via biem,* (Springer International Publishing, 2014) Chap. Piezoelectric Materials.

[61] Y. Fu, J. K. Luo, A. J. F. abd A. J. Walton, M. Y. Desmulliez, and W. I. Milne, *Biological and biomedical coatings handbook,* (CRC Press, 2011) Chap. Piezoelectric Zinc Oxide and Aluminum Nitride Films for Microfluidic and Biosensing Applications.

[62] J. Gualtieri, J. A. Kosinski, and a. A. Ballato, *Piezoelectric materials for acoustic wave applications,* IEEE Transactions on Ultrasonics, Ferroelectrics, and Frequency Control (1994).

[63] G. F. IRIARTE, *AlN Thin Film Electroacoustic Devices*, Ph.D. thesis, Faculty of Science and Technology, Uppsala University (2003).

[64] J. P. Kar and a. G. Bose, *Acoustic waves - from microdevices to helioseismology,* (Intech, 2011) Chap. Aluminum Nitride (AlN) Film Based Acoustic Devices: Material Synthesis and Device Fabrication.

[65] H. Amano, *Growth of gan on sapphire via low-temperature deposited buffer layer and realization of p-type gan by mg doping followed by low-energy electron beam irradiation,* Annalen der Physik **527**, 327 (2015), https://onlinelibrary.wiley.com/doi/pdf/10.1002/andp.201500802 .

[66] M. Gross, G. Henn, and H. Schroder, *Growth of gan and aln thin films by laser induced molecular beam epitaxy,* Materials Science and Engineering: B (1997).

[67] R. S. Kern, L. B. Rowland, S. Tanaka, and R. F. Davis, *Aluminum nitride-silicon carbide solid solutions grown by plasma-assisted, gas-source molecular beam epitaxy,* Journal of Materials Research (2011).

[68] J. N. Kidder, H. K. Yun, J. W. Rogers, and T. P. Pearsall, *Chemical composition of aln thin films deposited at 523_723 k using dimethylethylamine alane and ammonia,* Chemistry of Materials (1998).

[69] C. Cibert, F. Tetard, P. Djemia, C. Champeaux, A. Catherinot, and D. Tetard, *Mechanical and physicochemical properties of aln thin films obtained by pulsed laser deposition,* Superlattices and Microstructures (2004).

[70] D. Feiler, R. S. Williams, A. A. Talin, H. Yoon, and M. S. Goorsky, *Pulsed laser deposition of epitaxial aln, gan, and inn thin films on sapphire(0001),* Journal of Crystal Growth (1997).

[71] K. Jagannadham, A. K. Sharma, Q. Wei, R. Kalyanraman, and J. Narayan, *Structural characteristics of aln films deposited by pulsed laser deposition and reactive magnetron sputtering: A comparative study,* Journal of Vacuum Science & Technology A: Vacuum, Surfaces, and Films (1998).

[72] A. T. Tran, *AlN piezoelectric films for sensing and actuations*, Ph.D. thesis, Electrical Engineering, Mathematics and Computer Science, Delft University of Technology (2014).

[73] A. L. Kholkin, N. A. Pertsev, and A. V. Goltsev, *Piezoelectric and acoustic materials for transducer applications,* (Boston, MA: Springer US, 2008) Chap. Piezoelectricity and Crystal Symmetry, pp. 17–38.

[74] Q. Guo, G. Z. Cao, and I. Y. Shen, *Measurements of piezoelectric coefficient d33 of lead zirconate titanate thin films using a mini force hammer,* Journal of Vibration and Acoustics (2013).

[75] S. Magonov, *Piezoresponse Force Microscopy in Its Applications*, Tech. Rep. (NT-MDT spectrum instruments).

[76] O. Tigli and M. E. Zaghloul, *A novel saw device in cmos: Design, modeling, and fabrication,* IEEE Sensors Journal (2007).

[77] T. Hoang, *Design and realization of SAW pressure sensor using Aluminum Nitride*, Ph.D. thesis, University Joseph-Fourier - Grenoble I (2009).

[78] J. H. Hines, D. C. Malocha, and R. B. Brown, *Saw device impulse response modeling using broadband diffraction theory,* in *Proceedings., IEEE Ultrasonics Symposium* (1989).

[79] T. L. Szabo, K. R. Laker, and E. Cohen, *Interdigital transducer models: Their impact on filter synthesis,* IEEE Transactions on Sonics and Ultrasonics (1979).

[80] A. Hachigo and D. C. Malocha, *Saw device modeling including velocity dispersion based on zno/diamond/si layered structures,* IEEE Transactions on Ultrasonics, Ferroelectrics, and Frequency Control (1998).

[81] W. R. Smith, H. M. Gerard, J. H. Collins, T. M. Reeder, and H. J. Shaw, *Equivalent curcuit_analysis of interdigital surface wave transducers by use of equivalent circuit model,* IEEE TRANSACTIONS ON MICROWAVE THEORY AND TECHNIQUES (1969).

[82] M. E. Gowini and W. Moussa, *A reduced three dimensional model for saw sensors using finite element analysis,* Sensors (2009).

[83] W. c. Wilson and G. M. Atkinson, *A comparison of surface acoustic wave modeling methods,* in *Nanotech Conference and Exposition* (2009).

[84] T. Hoang, *Microdevices to helioseismology,* (InTech, 2011) Chap. SAW Parameters Analysis and Equivalent Circuit of SAW Device.

[85] T. Bui, A. Tran, B. Morana, J. Wei, T. C. Duc, and P. M. Sarro, *Effect of the interruption of the propagation path on the response of surface acoustic wave transducers,* in *2016 IEEE SENSORS* (2016).

[86] K. Dransfeld and E. Salzmann, *Physical acoustics,* (New York: Academic press, 1970) Chap. Excitation, detection and attenuation of high-frequency elastic surface waves, pp. 219–272.

3

SURFACE ACOUSTIC WAVE RESPONSE TO MICRO-SIZE DROPLET

This chapter presents the effect of a micro-size droplet shape, specifically the liquid contact angle, radius and area, on the SAW response. Besides, when a micro-size droplet is dripped on the surface of the SAW device, the shape of the micro-size droplet can also changes due to physical phenomena, such as evaporation, wetting, spreading, and surface tension. It leads to a change in the fractional coefficient of the SAW response. This change depends on the contact area between the sessile micro-size droplet and the SAW device more than the contact angle of the droplet. Besides, the effect of the hydrophobicity versus hydrophilicity of the contact surface on the duration of the fractional coefficient change is studied by comparisons of SAW devices coated with and without a silicon oxide or hexamethyldisilazane (HMDS) thin layer. It indicates a probable unstable response of the SAW device for micro-size liquid samples in sensing, manipulating and actuating applications. This chapter also shows that for liquids having a slow evaporation rate (BuAc < 0.8), e.g. water, the SAW response can be stable for a longer time due to the shrinking if the contact angle more than the contact radius.

3.1. INTRODUCTION

LEAKAGE phenomena of surface acoustic waves into a liquid medium form a significant limitation for the employment of SAW devices in liquid applications. However, if the propagation path of typical SAW devices is surrounded by inlimited liquid medium, most of the SAW energy is emitted into the liquid medium [1, 2]. This emitted energy is related to the longitudinal component of the SAWs which is referred to as compressional waves, Rayleigh surface acoustic waves, or longitudinal waves [3–5]. In practice, when the liquid medium has an insignificant volume (less than a microliter) like a small droplet, the emitted kinetic energy can transport and manipulate fluids such as separating, trapping, driving, mixing, jetting and atomizing [6–8]. Diverse mechanisms, such as microfluidic sensor, actuation and manipulation of micro-objects have been studied [7–10]. Depending on the envisioned SAW microfluidic application, the applied power and operating frequency need to be determined. For example, the centre frequency of the SAW fluid actuation and manipulation at microscale can be in the range of 0.01 – 1000 MHz. Low input power (in the order of mWatts) generates a preliminary acoustic streaming on the free surface of the sessile droplet for vibration, mixing and driving applications while higher input power (from 1 Watt) leads to breakup of the steady state of the sessile droplet [11, 12].

For a micro-size sessile droplet, typical phenomena in the sensor, actuation and manipulation are acoustic streaming flow, acoustic radiation force, jetting which are influenced by the formation of the droplet on the surface. Besides, evaporation plays a crucial role in microfluidic SAW applications owing to the presence of the changeable contact angle and contact area between the liquid and the piezoelectric substrate in a short transient time [8, 10, 13]. One obvious aspect of the droplet evaporation is an unstable SAW response during and after the short duration of the evaporation. Therefore, the shrinking sessile droplet placed on the propagation path can have a relevant effect on the microfluidic-actuation and -manipulation applications of the SAW device. The presence of energy from the adjacent liquid-solid interface is influenced by the behaviour of the droplet (surface tension, density, contact area and shape of the shrinking droplet) [14] and the properties of the piezoelectric device (surface wettability, surface roughness, input power and centre frequency) [7, 8]. The shrinking of the sessile droplet related to the contact angle and radius between the piezoelectric and liquid media has a direct effect on the SAW response. This is expressed by changes in the fractional coefficient of the SAW response before and after dropping the liquid and during the evaporation process of the droplet. Next, the theoretical analysis and experimental results show how the shrinking behaviour of both the contact angle and droplet radius during the droplet evaporation process can influence the variation of the SAW response.

3.2. EMISSION OF THE SAW ENERGY INTO EVOLVING MICRO-DROPLET

ACOUSTIC waves are radiated from the denser medium to the less dense one. Rayleigh surface acoustic waves are emitted at the Rayleigh angle because the sound of speed in the liquid is much smaller than that of the longitudinal waves [15, 16]. This refracted angle in the liquid medium is given by [17]:

$$\sin(\theta_R) = \frac{v_f}{v_R} = \frac{\lambda_f}{\lambda} \tag{3.1}$$

where v_f, λ_f are the velocity and wavelength of the liquid; while v_R and λ are related to the piezoelectric material. At the contact surface of the piezoelectric material, the amplitude of the normal particle displacement is at a maximum and is equal to that in the liquid medium [16, 17]. For a liquid medium with rectangle-shape domain $V_1(a,b,\lambda)$, the average SAW energy is transported from the contact surface to a maximum depth (up to λ) and to a width b because its energy concentrates mostly on the surface and can spread below the surface up to one [5] or a few wavelengths [18]. For an ideal, homogenous and isotropic piezoelectric surface, the fractional coefficient α is calculated using the following relationship:

$$\alpha \sim \frac{ba}{b\lambda}\frac{\rho_f v_f}{\rho v_R} \tag{3.2}$$

where ρ, ρ_f and a are the piezoelectric density, the liquid density and the length of the liquid medium, respectively. The attenuation of the SAW beam into each micrometre length of the liquid domain is expressed by α/a [dB/µm]. As indicated in Eq. 3.2, this attenuation depends on the properties of the liquid and piezoelectric material (density, sound speed and wavelength) considered. The larger volume of liquid is, the larger the attenuation of acoustic waves at the boundary of the two media is.

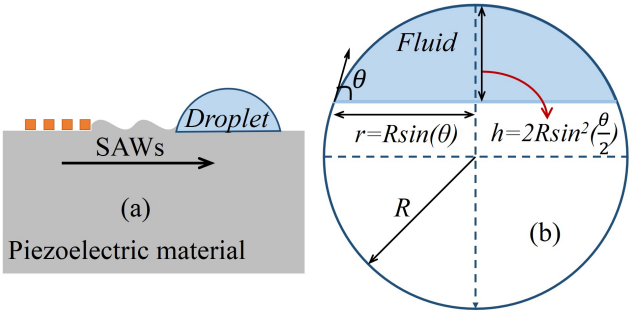

Figure 3.1: A schematic view (a) of the cross-section of a typical SAW-based microfluidic device and (b) the geometrical parameters of the (zoomed-in) 2D droplet view.

If we consider a microliter droplet, the droplet height is much smaller than the liquid wavelength (See Fig 3.1a). However, it becomes a dynamic medium due to the evaporation process. For example, if the considered droplet has a height h, a contact radius r and a contact angle θ as shown in Fig 3.1b, the liquid volume V_0 is then given by:

$$V_0 = \frac{\pi}{3} r^3 \frac{\sin\theta(2+\cos\theta)}{(1+\cos\theta)^2} \tag{3.3}$$

As the above fractional coefficient is relative to the space domain $V_1(2r,2r,\lambda) = 4r^2\lambda$, the fractional coefficient for the sessile droplet with a volume V_0 is rewritten as:

$$\alpha(r,\theta) \sim (\frac{\pi}{6}\frac{\rho_f v_f}{\lambda^2 \rho v_R}) r^2 \frac{\sin\theta(2+\cos\theta)}{(1+\cos\theta)^2} \sim kr^2 \frac{\sin\theta(2+\cos\theta)}{(1+\cos\theta)^2} \tag{3.4}$$

with the condition $\pi > \theta > 0$. The fraction coefficient depends on the both contact angle and radius of the droplet.

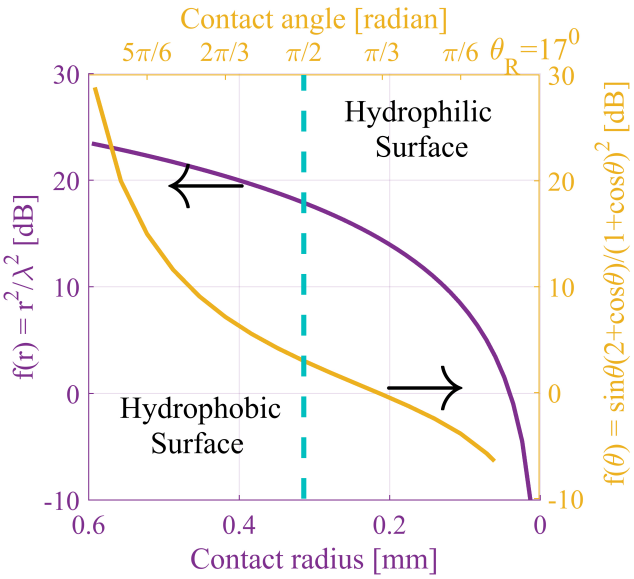

Figure 3.2: The fractional coefficient corresponding to the variation of the contact angle and radius of the droplet on a hydrophilic ($\theta_0 < 90^0$) and hydrophobic ($\theta_0 \geq 90^0$) surface.

Therefore, the fractional coefficient changes during the evaporation process. The variation of the fractional coefficient in the shrinking contact angle case is slower than that in the shrinking contact radius as shown in Fig 3.2, especially for a hydrophilic surface ($\theta < 90^0$). Averagely, for a 1-mm decrease of the contact radius, the descending velocity equals 4.39 times that of the 1-radian decrease of the contact angle. The variation of the contact angle can be neglected for hydrophilic and super-hydrophilic surfaces ($\theta_R < \theta < 90^0$) when the droplet volume decreases mainly due to the contact radius change [14]. The two evaporation cases of droplets often investigated are the shrinking droplet with a constant contact angle and a variable contact radius, and the one with variable contact angle and radius.

3.2.1. IDEAL CASE: CONSTANT CONTACT ANGLE AND VARIABLE CONTACT RADIUS

IF only the contact radius changes, the fractional coefficient for the sessile droplet with volume V_0 is rewritten as:

$$\alpha(r) \sim \frac{\pi}{2\lambda r_0}\frac{\rho_f v_f}{\rho v_R} r^2 \tag{3.5}$$

where λ, r_0, ρ_f, ρ, v_f and v_R are the wavelength of SAWs, the initial radius of the droplet, the liquid density, the piezoelectric density, the sound of speed in liquid and the SAW velocity, respectively. As the contact angle $\theta = \theta_0$ is assumed to be almost constant and always larger than the Rayleigh angle, the change in droplet radius is related to the energy loss during the evaporation process. With each liquid, the initial contact angle is different and measured by the video-based optical contact angle measuring instrument. The droplet radius is a function of the time as given by [19, 20]:

$$r^2 = r_0^2 - \frac{2D(c_s - c_\infty)}{\rho_f} g(\theta_0) f(\theta_0) t \tag{3.6}$$

where $r_0 = (\frac{3}{\pi} V_0 \frac{(1+\cos\theta_0)^2}{\sin\theta_0(2+\cos\theta_0)})^{1/3}$, $g(\theta_0) = \frac{\sin^3(\theta_0)}{(1-\cos\theta_0)^2(2+\cos\theta_0)}$, and $f(\theta_0) = \frac{\sin\theta_0}{1+\cos\theta_0} + 4\int_0^\infty \frac{1+\cosh(2\theta_0\tau)}{\sinh(2\pi\tau)} \tanh[(\pi - \theta_0)\tau] d\tau$. θ_0, r_0 and V_0 are the initial contact angle, the radius and the volume of the droplet, respectively. Parameters depending on the liquid medium are the diffusion coefficient of the vapor in the atmosphere D, the vapor concentration in the saturation atmosphere c_s and at infinity $c_\infty = Hc$. These parameters depend on the ambient temperature T and humidity H during the evaporation time.

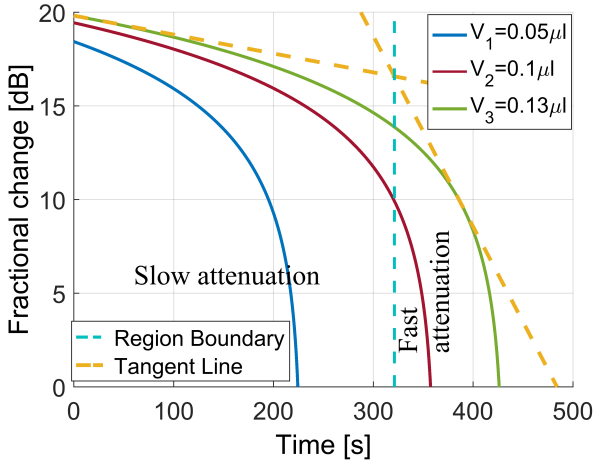

Figure 3.3: The dependence of the fractional change on the evaporation time of deionized water which has the initial contact angle of $\pi/6$ and different initial volumes of 0.05, 0.1 and 0.13 µl.

Fig 3.3 shows an example, an evaporation process of the micro-size deionized water on the hydrophilic surface ($\theta_0 < 90^0$). The larger the droplet volume is, the longer the evaporation duration is. The decay is divided into two parts: a gradual decay called slow attenuation, and a dramatic decay called fast attenuation. The duration of the slow attenuation is related to the initial volume of the sessile droplet.

3.2.2. VARIABLE CONTACT ANGLE AND RADIUS

DURING the evaporation process of the sessile droplet, the domain of the liquid medium varies continuously because of the shrinking contact angle, radius and height. There-

fore, the measured insertion loss changes during the evaporation process. To analyse this variation, the evolution of the droplet in the time domain and the variable fractional coefficient of the lost energy are considered. To investigate emission of the SAW beam into the micro-size droplet at time t, the evolution of the droplet during the evaporation process needs to be considered.

The evolution of a droplet is the variation of the contact radius and contact angle to reach a quasi-equilibrium shape at the transient instance. This variation is due to one or two parameters. If only the contact radius changes, it is called constant contact angle (CA) mode and if only the contact angle change, it is constant contact radius (CR) mode. If both parameters change, it is a stick-slide (SS) mode [19]. Based on the rate of the mass loss as reported by Popov [20–22], the time derivative equation for any contact angle and radius is:

$$\frac{1}{g(\theta)f(\theta)}\frac{dr^2}{dt}+\frac{r^2}{(1+\cos\theta)^2 f(\theta)}\frac{d\theta}{dt}=\frac{D(c_s-c_\infty)}{\rho_f} \tag{3.7}$$

where $f(\theta)=\frac{\sin\theta}{1+\cos\theta}+4\int_0^\infty \frac{1+\cosh(2\theta\tau)}{\sinh(2\pi\tau)}\tanh[(\pi-\theta)\tau]d\tau$ is a function of the variable θ and $g(\theta)=\frac{\sin^3(\theta)}{(1-\cos\theta)^2(2+\cos\theta)}$ with c_s, c_∞ and D being the saturation concentration, the ambient concentration and the diffusion coefficient of the liquid vapour in the atmosphere, respectively [21]. When the evaporation process is on a hydrophilic surface and under a homogeneous environment, the most commonly reported form is a serial order of the three modes, CR ($r=r_0$ and $\theta=\theta_0\rightarrow\theta_1^*$), SS ($r=r_0\rightarrow r_1$ and $\theta=\theta_1^*\rightarrow_2^*$) and CA ($r=r_1\rightarrow 0$ and $\theta=\theta_2^*$) [22, 23]. Sometimes, it is simplified into two modes (CR and CA) as shown in Fig 3.4.

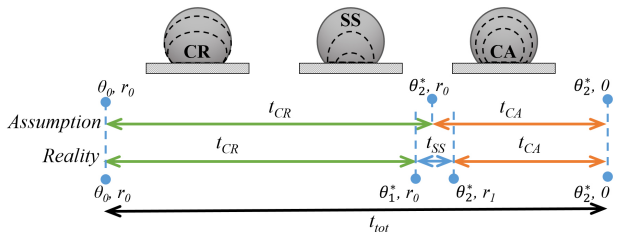

Figure 3.4: The lifetime of the common real and assumed droplet evaporation process on a hydrophilic surface.

The lifetime of the liquid evaporation process, t_{tot}, is the total of three modes ($t_{tot}=t_{CR}+t_{SS}+t_{CA}$) when $\theta=\theta_0\rightarrow\theta_2^*$ and $r=r_0\rightarrow 0$. It can be simplified as the lifetime of the droplet evaporation includes only CA ($\theta=\theta_0\rightarrow\theta_2^*$ and $r=r_0$) and CR ($\theta=\theta_2^*$ and $r=r_0\rightarrow 0$) modes; thus the total time is calculated as:

$$t_{tot}=\int_{\theta_2^*}^{\theta_0}\frac{\rho_f r_0^2}{D(c_s-c_\infty)(1+\cos\theta)^2 f(\theta)}d\theta+\frac{\rho_f r_0^2}{2D(c_s-c_\infty)g(\theta_2^*)f(\theta_2^*)} \tag{3.8}$$

For the CR mode, the contact angle recedes from $\theta=\theta_0$ to $\theta=\theta_1^*$. From Eq.3.8, the duration of a droplet related to the variable contact angle is calculated as:

$$t_{CR} = \int_{\theta_1^*}^{\theta_0} \frac{\rho_f r_0^2}{D(c_s - c_\infty)(1+\cos\theta)^2 f(\theta)} d\theta \tag{3.9}$$

For the CA mode ($\theta = \theta_2^*$ and $r = r_1 \to 0$), the change in the contact radius leads to a decrease of the liquid volume. This duration related to the variable contact radius is rewritten as:

$$t_{CA} = \frac{\rho_f r_1^2}{2D(c_s - c_\infty) g(\theta_2^*) f(\theta_2^*)} \tag{3.10}$$

For the SS mode, $\theta(t)$, $r(t)$ decreases and the volume reduces until the contact angle reaches the minimum value $\theta_2^* (\theta_R \le \theta_2^* \le \theta_1^* \le \theta_0)$ and the contact radius reaches . The duration for the SS mode is t_{SS}.

$$t_{SS} = \int_{\theta_2^*}^{\theta_1^*} \frac{\rho_f r_0^2}{D(c_s - c_\infty)(1+\cos\theta)^2 f(\theta)} d\theta + \frac{\rho_f (r_0^2 - r_1^2)}{2D(c_s - c_\infty) g(\theta_2^*) f(\theta_2^*)} \tag{3.11}$$

The relationship among θ_0, θ_1^* and θ_2^* is based on the unbalanced surface tension or unbalanced Young's force. It is determined by the maximum pinning force f_p which is a ratio of the practical pinning force at the reachable minimum angle and the preliminary pinning force at the initial angle. It depends on surface roughness, substrate-fluid interface and the constant surface tension of the fluid vapour [19]. The contact angle θ shrinks until it reaches $\theta = \arccos(f_p + \cos\theta_0)$with f_p in the range of (0, 2) [19]. For the CR mode, the contact angle with the maximum pinning force $f_{p,1}$ varies until it reaches the critical contact angle $\theta_1^* = \arccos(f_{p,1} + \cos(\theta_0))$ with the condition $0 < f_{p,1} \le 1 - \cos\theta_0$. For the SS mode, the contact angle corresponding to $f_{p,2}$ continues to vary until a new minimum critical contact angle value $\theta_2^* = \arccos(f_{p,2} + \cos\theta_1)$ is reached. The duration of the CR mode depends on the first pinning force $f_{p,1}$ while that of the SS mode depends on the second pinning force $f_{p,2}$. The condition $0 < f_{p,1} + f_{p,2} \le 1 - \cos\theta_0$ has to be satisfied because θ_1^* and θ_2^* are real numbers. The pinning force ratio $\frac{f_{p,2}}{f_{p,1}}$ depends on the hydrophilic or hydrophobic characteristic of the contact surface, the liquid properties (like surface tension and density), the contact area of the liquid on the surface and the ambient conditions. A few values of the maximum pinning forces ($f_{p,1}$; $f_{p,2}$) are shown in Fig 3.5.

The smaller the ratio is, the shorter the SS mode duration. For the super-hydrophobic surface corresponding to the infinitely small values of this ratio, only two distinct modes (CR and CA) appear, corresponding to $f_{p,2} = 0$. When the angle ratio θ_2^*/θ_1^* approaches to one, the pinning force ratio $f_{p,2}$ is close to zero and the duration of the SS mode goes to 0. In case, the pinning force ratio goes to infinite or the first pinning force equals 0 ($f_{p,1} = 0$), only SS and CA modes occur. When the second pinning force $f_{p,2}$ is larger than the first one $f_{p,1}$, the angle ratio θ_2^*/θ_1^* always lies in the small range bounded by the red ($f_{p,2}/f_{p,1} = 1$) and green ($f_{p,2}/f_{p,1} = \infty$) line. It also means that the SS mode lasts longer.

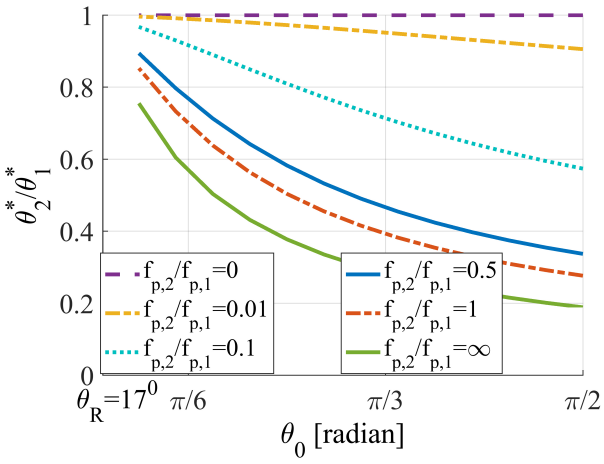

Figure 3.5: The dependence of the critical contact angle ratio $\frac{\theta_2^*}{\theta_1^*}$ on the initial contact angle corresponding to various values of the pinning forces.

From the analysist above, the fraction coefficient of the SAW device depends on each evaporation period of the droplet. For a hydrophilic surface, the evaporation process normally has three modes, thus the fractional coefficient varies through three modes. From the above equations (Eqs. 3.4, 3.9), (Eqs. 3.4, 3.10) and (Eqs. 3.4, 3.11), the fractional coefficient of the SAW energy emission in the CR, SS, CA modes is calculated (simply referred to as CR, SS, CA modes for brevity). The whole dynamic microdroplet evaporation process is then rewritten as:

$$\alpha(t) = \alpha_{CR(t=0\rightarrow t_{CR})} + \alpha_{SS(t=t_{CR}\rightarrow t_{CR}+t_{SS})+\alpha_{CA(t=t_{CR}+t_{SS}\rightarrow t_{CR}+t_{SS}+t_{CA})}} \tag{3.12}$$

The attenuation duration of each mode is relative to the evaporation time of the droplet. For example, all probable cases of the droplet evaporation process are shown in Fig 3.6a, and the corresponding attenuation behavior of the fractional coefficient are reported in Fig 3.6b. The CR mode takes place more quickly than the other modes while the CA mode is the slowest one. The fractional coefficient in the CA mode reduces slightly at first and then considerably at the end. It is relative to the physical behaviour of the dramatically shrinking contact radius in the end of the droplet evaporation process. Fig 3.6 also shows that the droplet volume is affected by the descending contact angle whereas the faster attenuation of the fractional coefficient is caused by the shrinking contact radius in the CA mode. The slope of the fractional coefficient is similar when the CR and SS mode in the droplet evaporation occurs. The shrinking of the sessile droplet in the CR and SS modes leads to a slow attenuation duration of the fractional coefficient, while in the CA mode, it causes fast attenuation duration.

The values of the pinning forces ($f_{p,1}$; $f_{p,2}$) are also shown in Fig 3.6b. If the pinning forces ($f_{p,1}$ and $f_{p,2}$) are generally similar, the total evaporation duration is similar like CR-SS-CA, CR-SS and SS case, thus the variation duration of the fractional coefficient is

mostly equal (for example, CR-SS, SS and CR-SS-CA case; CR-CA and SS-CA case). If the total pinning forces is small, it leads to a long evaporation process and a long variation duration of the fractional coefficient. For example, the CA case ($f_{p,1} = f_{p,2} = 0$) is the longest case whereas the CR case ($f_{p,1} + f_{p,2} = 0.04$) is the shortest one.

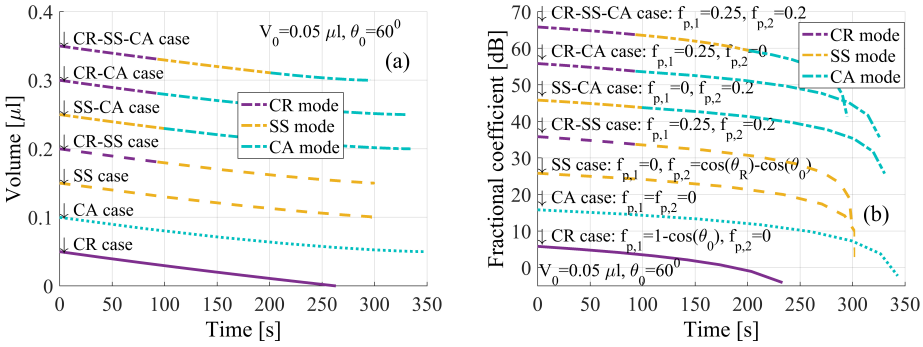

Figure 3.6: (a) Evolution with time of the droplet volume during the evaporation sequence and (b) fractional coefficient of the SAW response in all probable modes (10 dB and 0.05 µl offset in Y axis has been added to separate (a) the fractional coefficients and (b) the volume in modes).

Fig. 3.7a shows the variation of the fractional coefficient corresponding to different initial contact angles. For the hydrophilic surface, the smaller the initial contact angle is, the shorter the CR and SS modes are, whereas the longer the CA mode is. For the hydrophobic surface, if the initial contact angle is larger, the CR mode is shorter, whereas the SS and CA modes are longer. The total attenuation duration of the fractional coefficient is also longer. When the CR and SS modes are simplified into the CR mode, the attenuation duration of the fractional coefficients in the same initial contact angle ($\theta_0 = 60^0$) are approximately similar. If the surface of the liquid-solid interface is hydrophobic ($\theta_0 > 90^0$), the variation duration of the SAW response is longer than that on the hydrophilic surface ($\theta_0 \leq 90^0$).

In practice, the values θ_1^* and θ_2^* can be simplified into a single value if there is a small change in the contact radius in the SS mode on the hydrophilic surface. For example, the radius reduces only to 95 % in the SS mode of the CR-SS-CA and the simplified CR-CA case in Fig 3.7a. On the super-hydrophobic surface, only the CA and CR mode exist [13]. The transformation duration from θ_1^* to θ_2^* sometimes occurs quickly, especially for a liquid having a high evaporation rate and weak surface tension (for example: acetone, ethanol, isopropyl alcohol) [13, 24] or for the hydrophobic surface [13, 22]. These angles depend on the characteristic of the substrate surface, the liquid, the ambient atmosphere. Note that the case $\theta_1^* = \theta_2^*$ is a common example for the droplet evaporation process on a super-hydrophobic surface including two modes (CA and CR mode).

The droplet volume also causes the variation of the fractional coefficient (Fig 3.7b). If the physical parameters (for example, pinning forces, and contact angle) change, all modes get affected. The attenuation duration of the fractional coefficient in the CR, SS, CA modes is longer, namely 55, 118 and 174 seconds if the droplet volume increases from 0.05 to 0.1 µl. It means that the larger the droplet volume placed in the propagation path

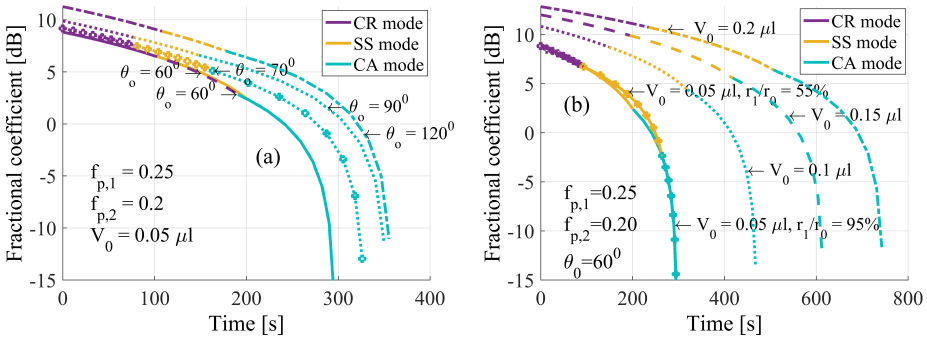

Figure 3.7: (a) Fractional coefficient corresponding to various values of the initial contact angle, namely 60^0, 90^0, and 120^0. (b) Various ascending values of the initial volume V_0 = 0.05, 0.1, 0.13 and 0.2 µl; r_1/r_0 = 95 % and the spinning forces $(f_{p,1}; f_{p,2})$ = (0.25; 0.20).

is, the longer the variation of the insertion loss S_{21} lasts.

The SS mode in the droplet evaporation process depends not only on the second pinning force $f_{p,2}$ but also on the contact radius decrease ($r = r_0 \rightarrow r_1$). It can occur for a longer time and affect the slope of the fractional coefficient more if the decrease of the contact radius is larger as shown in Fig 3.7b. For the 95 % decrease of the shrinking contact radius in the SS mode, the whole attenuation duration of the fractional coefficient is constant but in the CA mode is more tilted.

Consequently, the variation duration of the SAW response is caused by the surface properties (expressed by the total of the pinning forces and the initial contact angle) and the liquid properties (expressed by volume, density, sound velocity, evaporation rate and surface tension). The physical shrinking of the contact angle and radius in the CR, SS and CA modes in the droplet evaporation rate is the cause of the small and fast slope of the fractional coefficient.

3.3. EXPERIMENTAL PROCEDURE

3.3.1. CONFIGURATION OF THE SAW DEVICE

THE fabrication procedure for the SAW device includes two main parts, namely patterning the interdigital transducer (IDT) fingers on a 1 µm aluminium nitride (AlN) thin film and two top-surfaces (one hydrophilic and one hydrophobic surface).

For the 125.7 MHz SAW device, a 50-Ω IDT impedance requires an acoustic aperture of 50 wavelengths [5]. The IDTs of 40 straight electrode pairs are patterned by the optical photolithography on a silicon nitride (SiN) layer (Fig 3.8a), added to protect the piezoelectric surface during the inductively coupled plasma-reactive ion etching [24]. The other parameters are summarized in Table 3.1.

The hydrophilic surface used in the experiments is a 6.9 μm-thick silicon oxide (SiO_2) thin film, deposited by PECVD (Fig 3.8b). A cavity of 2 mm x 2.5 mm is created in the oxide to form a dip at the centre of the band. This means that the in-band response is distorted one time at the centre frequency as shown in the comparison of the conventional

Table 3.1: Parameters of the SAW transducer.

Parameters	Value	Unit
Number of the input and output fingers	40x40	
The aperture of input and output IDTs	2	mm
IDT finger width $d = \lambda/4$	10	µm
IDT finger height h	0.5	µm
The propagation path between input and output IDTs	1000	µm

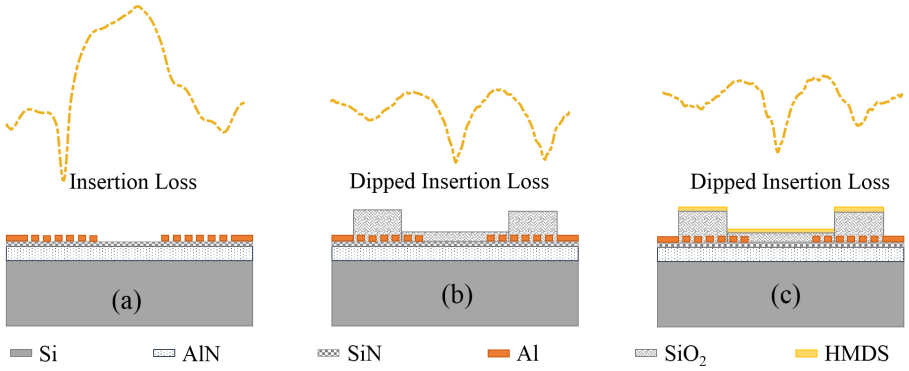

Figure 3.8: (a) Conventional and experimental SAW structure with the typical and dipped insertion loss caused by (b) the SiO_2 and (c) HMDS thin-film cavity.

and dipped insertion loss of Fig 3.8. For the conventional SAW device, the insertion loss after dropping the liquid varies around the primary insertion loss measured before dropping the liquid [24]. For the dipped SAW device, the variation of the insertion loss after dropping stays at one side of the primary insertion loss. Hence, this variation during the shrinking process of the droplet is easier to observe. To increase the contact angle of the sessile droplet, a thin layer (a few monolayers) hexamethyldisilazane (HMDS) is applied by exposing the surface of the sample to HMDS vapour for 15 minutes in a controlled oven. The insertion loss before liquid dropping for the SAW device covered by HMDS is similar to that of the SAW device with only the SiO_2 thin film (Fig 3.8b, c).

3.3.2. MEASUREMENT SETUP

THE scattering matrix data of the SAW device is measured by HP 8753E RF vector network analyzer and collected continuously every 10 seconds by using the Cascade Microtech software. The applied power (5 dBm) is small enough not to influence significantly the evaporation process. The droplet is applied with a pipette (Rainin Classic Pipette PR-2). The samples are placed in a closed chamber to keep a stable measurement environment. The experiments are performed in a controlled laboratory environment (humidity 68 ± 2 % and temperature 19 ± 0.5 ^{0}C) so to have a controlled evaporation

process.

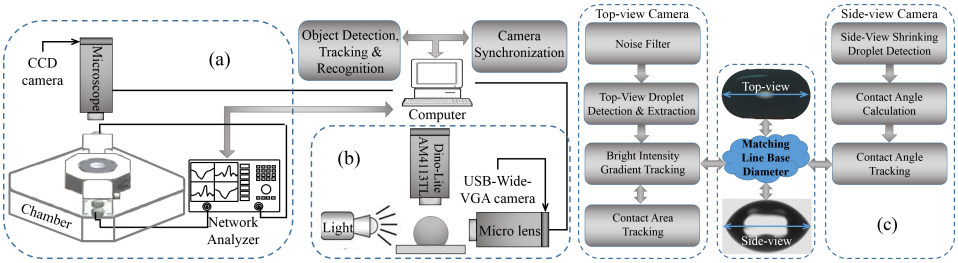

Figure 3.9: Measurement setup for (a) the electrical data and the contact area; (b) the contact angle; and (c) camera synchronization algorithm.

Deionized water (DW) with a volume in the range of 0.05 – 0.13 µl is used in the experiments. This volume is selected to study the lower limit of detection of our SAW device and to avoid overflow from the cavity to the electrical contacts to take place. The droplet evaporation process is tracked by a top-view camera as shown in Fig 3.9a. The contact radius and the bright intensity are recorded by this camera. The propagation path is a reference for measuring the droplet contact area, width and length. The top-view optical images, collected by the CCD camera in Fig 3.9a, are converted into grayscale images and their salt-and-pepper noise is filtered. Before processing the image, the ambient background of the droplet is removed. The brightness intensity of the spot is related to the number of pixels with a grey intensity smaller than the threshold. The threshold is adapted to the average threshold of the individual optical image and ranges from 35 to 90 because of the automatic focus mode of the recorded video. The contact area is limited by the boundary black pixels.

The second system has a top-view and a side-view camera (Fig 3.9b). The contact angle, temperature and line base diameter are recorded and measured by the contact angle system OCA20. The DINO top-view camera recorded initial optical images which are compared to those of the CCD top-view camera. The optical images of the top-view and CCD side-view cameras are synchronized by the line base diameter during the droplet evaporation process (see Fig 3.9c).

As an example, data for the droplet volume of 0.13 µl are reported in Table 3.2. The data extracted from the top-view optical images is processed to remove noise and background before contact area, length and width of the sessile droplet are measured. The contact angle is found after the synchronization of the side-view and top-view cameras. The initial data of the optical images, such as contact angle θ_0, droplet volume V_0, are used for the theoretical data. The variation of the contact angle is also considered and possibly anticipated by the bright intensity of the droplet which is processed by the optical images of the top-view camera. Based on the optical image data, the fractional coefficient is approximately rewritten as $\alpha(s,\theta) = \frac{s}{\lambda^2}\frac{\sin\theta(2+\cos\theta)}{(1+\cos\theta)^2}\frac{\pi\rho_f v_f}{6\rho v_R}$ where s the contact area of the sessile droplet at time t.

Table 3.2: Matching line base diameters of the synchronized cameras for the 0.13 µl sessile droplet case.

Time (seconds)	Top-view camera			Side-view camera
	Contact Area S (mm^2)	Length$L$ (mm)	Width W (mm)	Contact Angle θ (^{0})
0	1.31647	1.52419	1	65.5
100	1.30187	1.51210	0.991935	57.0
200	1.2992	1.47984	0.983871	49.1
300	1.29834	1.47984	0.983871	39.6
400	1.29761	1.47984	0.983871	26.7
500	1.29709	1.47581	0.983871	19.0
600	1.29619	1.47581	0.983871	17.5
700	1.04996	1.21774	0.9717740	16.8
730	0.0036583	0.20161	3 0.0322581	16.7
750	0	0	0	0

3.4. RESULTS AND DISCUSSIONS

3.4.1. MICRO-SIZE DROPLET ON HYDROPHILIC SURFACE

THE data from the top-view optical image and the corresponding SAW response are shown in Fig 3.10a. In the first 450 seconds, the contact area of the sessile droplet (1.45 % evaporated contact area) is mostly constant, thus the insertion loss does not change significantly. We refer to this situation as the CR mode which has a constant radius and changeable contact angle (from 65.5^0 down to 20.0^0). This contact angle change can also be observed by the bright spot on the optical images, caused by the reflected light of the top-view microscope. The SS mode is lightly stronger receding from 450 to 680 seconds because of only 3.07 % reduced contact area and slightly reduced contact angle (from 20.0^0 down to 16.7^0). During the first 680 seconds, corresponding to 4.52 % reduced contact area, the intensity of the bright spots changes continuously because of the changeable contact angle. Afterwards, the colour observation of the bright intensity of the sessile droplet shows that the contact angle is mostly constant while the contact radius changes quickly. Here, the insertion loss starts to have a small fluctuation and then quickly returns to the initial status.

The parameters of the deionized water for the theoretical data are based on physical properties, and specific conditions as indicated in Table 3.3.

Fig 3.10c shows that the measured electrical data are in better agreement with the theoretical data than the optical image data. The reason is that the automatic focus mode of the top-view camera can produce small nonlinear values of the contact area. A pseudo-increase error is eliminated by the nonlinear filtering using the comparison of the contiguous values. However, errors caused by the pseudo-decrease values or the synchronization process of the top-view and side-view cameras can still occur. It is a limitation of the optical image processing.

The bright intensity observed by the top-view camera shows the droplet evaporation

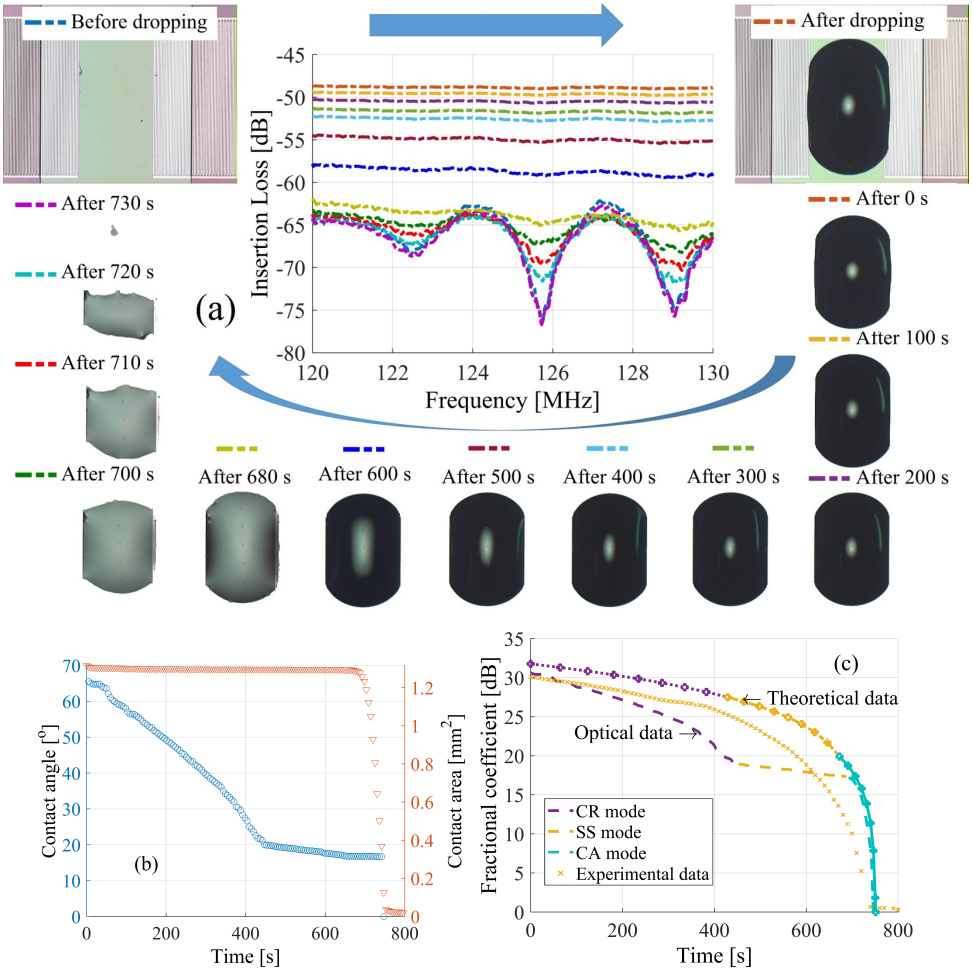

Figure 3.10: (a) The variation of the insertion loss and the optical images from the top-view camera at several times of the 0.13 µl droplet on the hydrophilic surface. (b) The contact angle and radius change during the evaporation process of the sessile droplet recorded by the top-view camera. (c) Comparison of the variation of the fractional coefficient calculated using the theoretical data, optical-image data and electrical data.

experiences the CA-SS-CR mode sequence and at the end, the dramatic drop is related to the shrinking contact radius of the CR mode. The evaporation time of the same size droplet on the hydrophobic surface is longer than that on the hydrophilic surface [13] because the pinning forces are larger. It means the variation duration of the contact angle can last longer. Similarly, if two droplets of the same volume but with the different contact angle and area are placed on the same surface, the one with the larger contact area evaporates faster because of the smaller pinning forces. The droplet keeps a similar shape as the contact area until the contact angle reaches a critical value θ_2^*. For a 0.05 µl droplet on the same hydrophilic surface, as the initial contact area of the sessile

Table 3.3: Parameters of the sessile droplet used for the theoretical data.

Parameter	Value	Unit
Diffusion coefficient D at 20^0C	22.56 x 10^{-6}	m^2/s
Saturated vapor concentration c_s	0.015	kg/m^3
Initial contact angle θ_0	66	^{0}
Spinning force $f_{p,1}$	0.447	
Spinning force $f_{p,2}$	0.125	
Radius ratio (r_1/r_0)	95	%

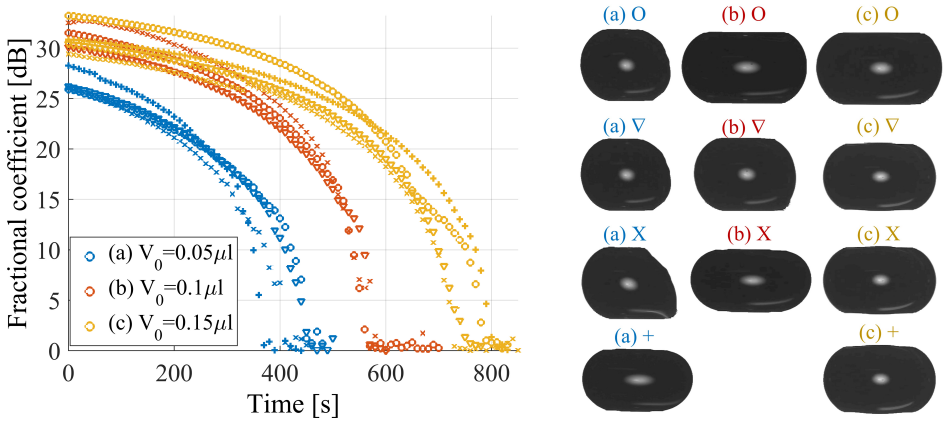

Figure 3.11: The scatter plot of the variation of the fractional coefficient in the time domain when deionized water is dropped on the hydrophilic SAW surface (O, X,∇, + from different experiments; blue scatters for the volume of 0.05 µl, red ones for the volume of 0.1 µl and yellow ones for the volume of 0.13 µl). (a), (b), (c) Optical images from the top-view camera corresponding to the droplet volume of 0.05, 0.10 and 0.13 µl.

droplet (see image (a) + in Fig 3.11) is 1.41 times that of the droplet (see image (a) O in Fig 3.11), and its initial contact angle is smaller, its evaporation time is faster. Therefore, the fractional coefficient returns to zero more quickly. Fig 3.11 also shows that the evaporation duration of the bigger droplet volume results in longer duration of the fractional coefficient variation, namely 420, 573 and 760 seconds for 0.05, 0.1, 0.13 µl. It is caused by the longer duration of the shrinking contact angle when the bigger droplet evaporates on the propagation path of the SAW device. In all cases, the fast attenuation of the fractional coefficient is caused by the dramatically decrease of the contact radius in the droplet evaporation process.

3.4.2. MICRO-SIZE DROPLET ON THE HYDROPHOBIC SURFACE

THE same volume droplet is experimented on the hydrophobic surface of the SAW device when covered by a thin layer of HMDS layer.

In Fig 3.12, results related to the same-volume droplet on the hydrophilic ($\theta << 90^0$

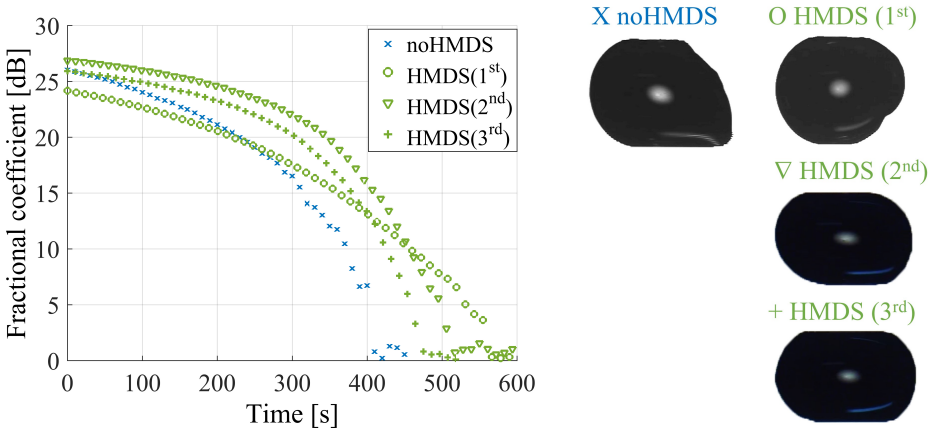

Figure 3.12: The variation of the fractional coefficient during the 0.05 µl droplet evaporation on the hydrophobic (HMDS) and hydrophilic (no HMDS) surface of the SAW device.

because of the silicon oxide film) and hydrophobic surface ($\theta > 90^0$ because of the HMDS layer) are shown. The contact angle of the droplet on the hydrophobic surface is larger because this contact area is smaller (91 % to 98 % contact area of the sessile droplet on the hydrophilic surface). The magnitude of the bright spot on the CCD top-view optical image shows the larger initial contact angle on the hydrophobic surface (O, ∇ and +). The droplet evaporation time is influenced by the contact angle because if the contact angle is smaller, the contact area is larger and the liquid layer is thinner. The saturation vapour pressure at the droplet surface is increased. The pinning force of the hydrophilic surface becomes smaller, the pinning time becomes longer; thus the evaporation time is shorter [13, 25]. The measured variation duration of the fractional coefficient for the hydrophobic surface (HMDS film) is 110 seconds longer than for the hydrophilic surface (SiO_2 film).

3.5. CONCLUSION

THE energy emitted into the liquid medium is different for the dissimilar contact area between the sessile droplet and the piezoelectric material. In additions, the evaporation phenomenon of the sessile droplet contributes as well. The dynamic change caused by the contact angle and radius of the sessile droplet occurs during the evaporation process. The change in contact radius influences the insertion loss more than the change in contact angle, especially on the hydrophilic ($\theta < 90^0$) and super-hydrophilic surface ($\theta << 90^0$). The variation duration of the fractional coefficient is proportional to the droplet volume and the surface wettability. For example, it is 420, 573 and 760 seconds for the 0.05, 0.10 and 0.13 µl sessile deionized water droplet respectively, on the top hydrophilic film (SiO_2 film) of the SAW device. In average, it is 110 seconds longer if the droplet is placed on the hydrophobic layer (HMDS) compared to the hydrophilic layer (SiO_2). This work highlights the need to include, for proper use of SAW devices in microfluidic applications, the shape of the droplet on the surface, the effect of the evap-

oration, the droplet volume and the surface wettability, especially for experiments which requires long-time actuation and manipulation.

REFERENCES

[1] S. Showko and K. Jun, *Surface acoustic wave sensors,* Japanese Journal of Applied Physics (2004).

[2] S. Tamura, R. E. Vines, and J. P. Wolfe, *Effects of liquid loading on surface acoustic waves in solids,* Physical Review B (1996).

[3] T. A. F. Clemens and C. W. Ruppel, *Advances in surface acoustic wave technology, systems and applications* (Singapore: World Scientific, 2000).

[4] S. Biryukov, Y. Gulyaev, V. Krylov, and V. Plessky, *Surface Acoustic Waves in Inhomogeneous Media* (Springer-Verlag Berlin Heidelberg New york, 1995).

[5] J. Ballantine, R. M. White, S. I. Martin, A. J. Ricco, E. T. Zellers, G. C. Frye, and et al., *Acoustic Wave Sensors, 1st Edition: Theory, Design, & Physico-Chemical Applications* (USA: ACADEMIC PRESS, 1997).

[6] A. Qi, L. Y. Yeo, and J. R. Friend, *Interfacial destabilization and atomization driven by surface acoustic waves,* Physics of Fluids (2008).

[7] R. Raghavan, J. Friend, and L. Yeo, *Particle concentration via acoustically driven microcentrifugation: micropiv flow visualization and numerical modelling studies,* Microfluid Nanofluid (2010).

[8] M. K. Tan, J. R. Friend, and L. Y. Yeo, *Microparticle collection and concentration via a miniature surface acoustic wave device,* Lab on a Chip (2007).

[9] G. Destgeer and H. J. Sung, *Recent advances in microfluidic actuation and micro-object manipulation via surface acoustic waves,* Lab on a Chip (2015).

[10] S. U. Senveli and O. Tigli, *Finite element method analysis of surface acoustic wave devices with microcavities for detection of liquids,* Journal of Applied Physics (2013).

[11] C. Witte, J. Reboud, R. Wilson, J. M. Cooper, and S. L. Neale, *Microfluidic resonant cavities enable acoustophoresis on a disposable superstrate,* Lab on a Chip (2014).

[12] L. Y. Yeo and J. R. Friend, *Ultrafast microfluidics using surface acoustic waves,* Biomicrofluidics (2009).

[13] D. H. Shin, S. H. Lee, J.-Y. Jung, and J. Y. Yoo, *Evaporating characteristics of sessile droplet on hydrophobic and hydrophilic surfaces,* Microelectronic Engineering (2009).

[14] T. Bui, B. Morana, A. Akhnoukh, T. C. Duc, and P. M. Sarro, *Liquid identification by using a micro-electro-mechanical interdigital transducer,* Analyst (2017).

[15] S. Showko, M. Yoshikazu, and M. Toyosaka, *Experimental study on liquid streaming by saw,* Japanese Journal of Applied Physics (1989).

[16] D. Morgan, *Surface Acoustic Wave Filters: With Applications to Electronic Communications and Signal Processing* (Elsevier Ltd., 2007).

[17] K. Dransfeld and E. Salzmann, *Physical acoustics,* (New York: Academic press, 1970) Chap. Excitation, detection and attenuation of high-frequency elastic surface waves, pp. 219–272.

[18] L. Y. Yeo and J. R. Friend, *Surface acoustic wave microfluidics,* Annual Review of Fluid Mechanics (2014).

[19] J. M. Stauber, S. K. Wilson, B. R. Duffy, and K. Sefiane, *On the lifetimes of evaporating droplets with related initial and receding contact angles,* Physics of Fluids (2015).

[20] S. Dash and S. V. Garimella, *Droplet evaporation dynamics on a superhydrophobic surface with negligible hysteresis,* Langmuir (2013).

[21] Y. O. Popov, *Evaporative deposition patterns: Spatial dimensions of the deposit,* Physical Review E (2005).

[22] G. McHale, S. Aqil, N. J. Shirtcliffe, M. I. Newton, and H. Y. Erbil, *Analysis of droplet evaporation on a superhydrophobic surface,* Langmuir (2005).

[23] T. A. Nguyen, A. V. Nguyen, M. A. Hampton, Z. P. Xu, L. Huang, and V. Rudolph, *Theoretical and experimental analysis of droplet evaporation on solid surfaces,* Chemical Engineering Science (2012).

[24] T. Bui, B. Morana, A. Tran, T. Scholtes, T. C. Duc, and a. P. M. Sarro, *Saw device for liquid vaporization rate and remaining molecule sensing,* in *IEEE-SENSORS2015* (2015).

[25] S. Chandra, M. di Marzo, Y. M. Qiao, and P. Tartarini, *Effect of liquid-solid contact angle on droplet evaporation,* Fire Safety Journal (1996).

4

EVAPORATED LIQUID SAW MICROSENSORS

In this chapter, a surface-acoustic-mode Aluminum Nitride (AlN) transducer is utilized to investigate the sensing ability of the SAW device for the detection of liquid types. Taking advantage of the changeable SAW response related to the different shrinking shape and stagnant liquid molecules of each liquid, it is possible to detect small amounts of liquids, in the microliter range. The mechanisms for identifying the nature of the tested samples, are related to both physical-property (liquid density, equilibrium vapor pressures, molecular weights, boiling points, sound speed in liquid and evaporation rate) and mass loading (concentration of stagnant liquid molecules). Eight liquid samples, isopropanol (IPA), ethanol (ETH), deionized-water (DW), tap water (TW), heptane (HEP), propylene glycol monomethyl ether acetate (PGMEA), hexamethyldisilazane (HMDS) and acetone (ACE), with either similar or rather diverse characteristics have been tested.

4.1. INTRODUCTION

As mentioned in section 2.3, the surface acoustic wave (SAW) mode is very appealing for gas sensing applications due to the sensitivity to surface perturbations induced by pressure, environment, or mass loading [1–3]. It is rarely used for liquid sensing because of the leakage phenomenon of the longitudinal wave component into a liquid medium. The signal of the SAW device is not received at the receiver when a large liquid volume is placed on the whole propagation path [3, 4]. However, this component is extremely sensitive to surface mass density induced by the active force of an object, such as a thin gold film [5], a microliter droplet [6], a moving liquid [7–9], microparticles [1, 10, 11] and a contaminated liquid [10] on or through the piezoelectric surface. For liquid applications, a measurable energy loss detects the type of liquid. It is possible to identify the liquid on the propagation path based on stagnant liquid molecules on the surface [6]. Here, we employ physical properties, such as the liquid evaporation rate, density and sound speed, to enhance the accuracy of surface-acoustic-mode Aluminum Nitride (AlN) transducers.

The most common mechanism employs mass loading which results a frequency shift due to the adsorption of chemical substances on the functionalized surface. Another mechanism is the change in operating frequency and attenuation induced by rheological properties or thermal effects of any liquid medium in contact with the piezoelectric material [11, 12]. For example, investigated chemical substances are some teas [13], oil contamination [14] and heavy metal in ground water [15, 16]. Here, we employ both physical properties (liquid density, sound speed in liquids and evaporation rate) and mass loading (concentration of stagnant liquid molecules) during and after the evaporation process to identify the liquid type. Specifically, during this process, a phase transition from liquid to gas phase of the molecules at the droplet surface takes place quickly or slowly depending on the evaporation rate of each liquid [17]. It leads to different attenuation duration for SAWs for each liquid. This attenuation variation depends on the density and sound speed in liquids. When the dynamic equilibrium is reached, the evaporation process stops. There are liquid molecules left on the surface, which alter the mass density of the piezoelectric surface. Taking advantage of these distinct physical properties, we have developed a potential method to identify the type of liquid being studied. This novel method uses a SAW transducer with a large IDT aperture and with a cavity to accommodate small volumes (µl range) of liquids. The oscillation variation and duration in the magnitude of the insertion loss during the evaporation process are analyzed and experimentally recorded. The evaluation of the relation between surface mass loading of the SAW device and stagnant liquid molecules is described. These are validated by experimental results obtained with eight liquids. The chosen substances include liquids that have similar physical properties (evaporation rate and density), such as isopropanol (IPA), ethanol (ETH) and acetone (ACE), as well as with quite different properties (evaporation rate, density, sound speed or chemical bond), like deionized - water (DW), tap water (TW), hexamethyldisilazane (HMDS), heptane (HEP) and propylene glycol monomethyl ether acetate (PGMEA).

4.2. SAW RESPONSE DURING THE LIQUID EVAPORATION

4.2.1. THE ENERGY ATTENUATION OF THE SAW DEVICE

THE deformation of the evaporated droplet can affect the contact angle, radius or both. If the evaporation process of the liquid happens quickly, the evolution of the evaporated droplet is simplified into the shrinking of the contact radius. If the surface for carrying the liquid is hydrophilic, the emitted energy of the SAW device is caused only by the shrinking contact radius. As the evaporation process of micro-size droplet is significantly influenced by the shrinking contact radius, the evolution of the droplet is considered as a constant contact angle (CA) mode.

After the liquid to be identified is dropped on the propagation path of a SAW transducer, the evaporation process of the droplet starts. Before the dynamic equilibrium is reached, the droplet radius decreases and creates a 'blank' area on the surface like a non-leaky medium, and there is a signal at the receiver. Consequently, the transducer response is attenuated due to the smaller energy absorption inside the liquid medium at Rayleigh angle θ_R as shown in Fig 4.1. It changes continuously in correspondence of the variation of the 'blank' area on the surface. The rate of this variation depends on the evaporation rate of the liquid. The power dissipation into the liquid medium is a much more remarkable effect than the frequency shift caused by the change in the surface mass density. The emission energy depends on physical properties of the liquid (see section 3.2). It is calculated approximately by the Eq. 3.5 and the contact radius between the liquid and the piezoelectric media is based on Eq. 3.6 for the constant contact angle mode.

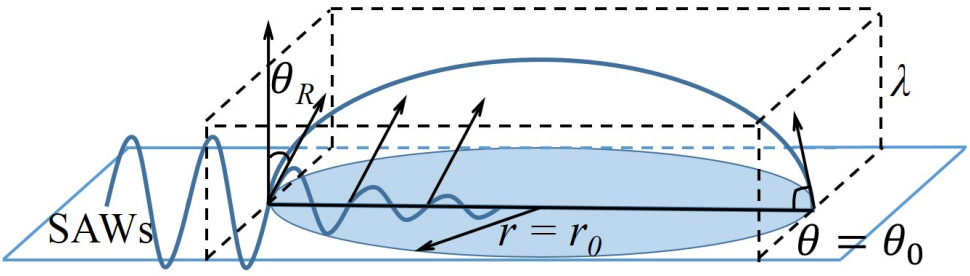

Figure 4.1: Schematic view of the SAW energy radiated at the contact between the piezoelectric surface and liquid media.

The vapor concentration parameters are different for different liquids and sensitive to the ambient temperature T and humidity H during the evaporation time. For example, values of some liquids in air at a temperature of 20^0C are shown in Table 4.1 [18–20].

From Eq. 3.5 ad 3.6, the fractional change depends on physical properties of the liquid such as density, sound speed in the liquid and rate of evaporation. The fractional change of the CA mode in Fig 4.2 is a function of the liquid contact radius related to the initial contact angle $\theta_0 = \pi/3$ and to the liquid volume. It has two descending parts during the transient evaporation time. One refers to a fast attenuation region when the fractional change descends quickly and the other is a slow attenuation region when it

Table 4.1: Diffusivity and vapour concentration of liquids in air at 20^0C.

Liquid	D **(10^{-6} m^2/s)**	c_s **(kg/m^3)**
Water	24.46	0.017
Heptane	7.06	0.0941
Ethanol	12.68	0.0375
Acetone	12.12	0.0522

varies more slowly. These regions are separated by two tangents of the fractional change line, with a factor 10 difference in slope.

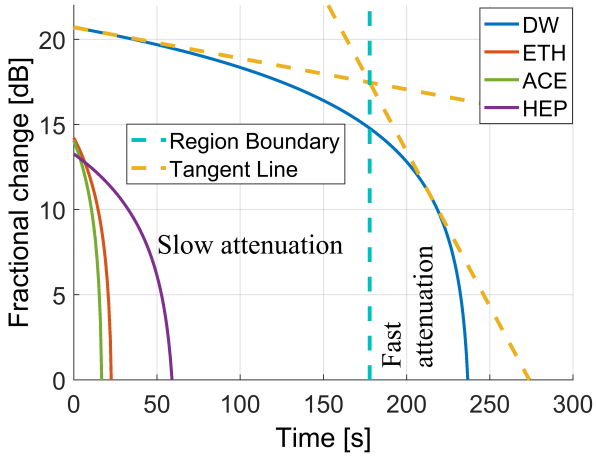

Figure 4.2: The dependence of the fractional change on the evaporation time of some liquids for an initial volume of 0.05 µl.

4.2.2. MASS SENSITIVITY OF THE SAW DEVICE AFTER COMPLETE DROPLET EVAPORATION

THE second detection mechanism employs a comparison of the variation of the transducer response due to the change in the density mass on the surface. When it reaches the equilibrium, there is no change in the amount of liquid or vapor. Ultimately, as liquid molecules are left after the evaporation process, a change in the surface mass density of the piezoelectric surface is observed. Each liquid has a different pattern formation by the self-assembly of the molecules at the end of the evaporation process. For example, when they have rather different properties like the case for IPA or ETH with HEP, or even when the physical properties such as the boiling point, the vapor pressure, and the molecular weight are quite similar (IPA and ETH), the concentration and pattern formation of the stagnant liquid molecules are dissimilar (see Fig 4.3). At the dynamic equilibrium, the measured transducer responses are almost constant. The fractional change $\alpha(r)$ is

approximately zero because the radius of the liquid droplet and the contact angle of the concentrated liquid molecules go to zero (see Eq. 3.6). Therefore, the absorption caused by the leakage phenomenon is ignored. The remaining liquid molecules after the evaporation form dense monolayers or multilayers k_i of molecules [21] which are also referred as clusters. This leads to perturbations on the surface and change the areal mass density. As chosen liquids are pure and are tested in the same condition, this change only depends on the size (molecular weight) and concentration of the molecules. The stagnant liquid molecules on the solid surface refer to hard macromolecules adhering to the thin AlN film, which cause a roughness increase of the film surface. Regarding the formation of the liquid molecule layers on the thin film, the surface mass density, also called areal density, is given by the ratio of the mass to the area. The area includes the AlN surface a_{AlN} which is not covered by the liquid and total meniscus areas a_l of n liquid clusters. The height of the monolayer cluster meniscus is negligible and the meniscus area is approximated to its 2D projection on the thin film surface. Hence, the average areal density is written by:

$$\rho_s = \frac{m_{AlN} + \sum_{i=1}^{n} m_i}{a_{AlN} + a_l} \approx \begin{cases} \dfrac{m_{AlN} + \sum_{i=1}^{n} m_i}{a_s} when & k_i \approx 1 (monolayer) \\ \dfrac{m_{AlN} + \sum_{i=1}^{n} m_i}{a_{AlN} + \sum_{i=1}^{n} \frac{m_i}{\rho d k_i}} when & k_i \gg 1 (multilayer) \end{cases} \tag{4.1}$$

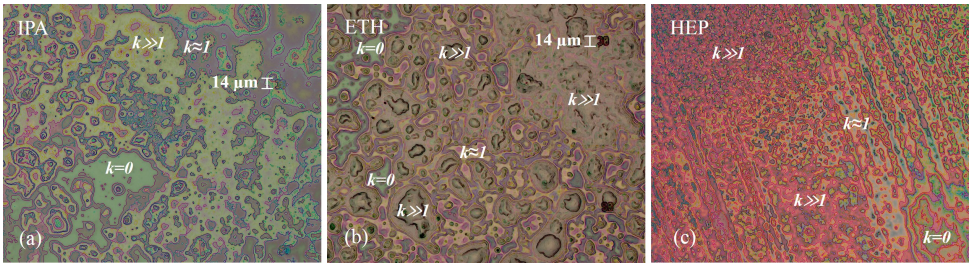

Figure 4.3: The pattern formation for (a) IPA, (b) ETH and (c) HEP after the evaporation process.

where m_{AlN}, m_i, a_s, d are the mass of the AlN thin film and of the stagnant liquid cluster i^{th}, the surface area of the thin film before dropping liquid and the thickness of a layer, respectively. If there are N_i stagnant molecules in the cluster i^{th}, the cluster mass is given by:

$$m_i = \frac{N_i * M}{6.02 * 10^{23}} \tag{4.2}$$

where M is the molecular weight of the liquid and $K = 6.02 * 10^{23}$ (mol^{-1}) is Avogadro's number. So, the average surface mass density is rewritten as:

$$\rho_s \approx \begin{cases} \dfrac{\rho_{AlN}h+\sum_{i=1}^{n}\frac{N_i M}{K}}{a_s} \approx \dfrac{\rho_{AlN}hK+NM}{a_s K} & when \quad k_i \approx 1 \\ \dfrac{\rho_{AlN}h+\sum_{i=1}^{n}\frac{N_i M}{K}}{a_{AlN}+\sum_{i=1}^{n}\frac{N_i M}{K\rho d k_i}} \approx \dfrac{\rho_{AlN}hK+NM}{a_{AlN}K+\frac{M}{\rho d}\sum_{i=1}^{n}\frac{N_i}{k_i}} \approx \dfrac{\rho_{AlN}hK+NM}{a_{AlN}K+\frac{nM}{\rho d}\bar{N}} & when \quad k_i \gg 1 \end{cases} \tag{4.3}$$

where ρ_{AlN}, h, N, $\overline{N}$ are the density and the thickness of the thin film, the total stagnant liquid molecules and the average molecule concertation in the layer of the cluster in contact with the thin film, respectively. After the evaporation process, the variation of the surface mass density leads to the fractional change in the kinetic energy density of SAWs as well as the negative fractional change of the wave velocity and the operating frequency which is given by [21]:

$$\frac{\Delta U}{U_0} = -\frac{\Delta v}{v_0} = \rho_s \frac{v_0}{4P}(v_{x0}^2 + v_{y0}^2 + v_{z0}^2) = \rho_s S_m f_0 \tag{4.4}$$

where v_{x0}, v_{y0} and v_{z0} are the unperturbed SAW velocities on the surface along X, Y, Z axis, respectively while P and U_0 are the power density and the peak of the kinetic energy of SAWs on the AlN thin film. The mass sensitivity factor $S_m = \frac{v_0}{4P}(v_{x0}^2 + v_{y0}^2 + v_{z0}^2)$ only depends on electromechanical properties of the surface material, thus this factor is mostly constant for any liquid. If the remaining liquid molecules on the surface are negligible, like for deionized water, the mass density change is almost constant. Hence, the change in the kinetic energy density only depends on the mass sensitivity factor of the material. On the contrary, if they are rather significant like for IPA, ETH and HEP (see Fig 4.3) the output signal of the SAW device is significantly perturbed. By using a network analyzer in the measurement setup, the SAW device is incorporated as a feedback-loop oscillator; so that, the fractional frequency variation $\frac{\Delta f}{f_0}$ follows the fractional velocity variation $\frac{\Delta v}{v_0}$ [21]. From Eqs. 4.3 and 4.4, the fractional change of the frequency is calculated as:

$$\frac{d\Delta f}{f_0} \approx S_m S_l dN \qquad where \quad S_l = \begin{cases} -\frac{M}{a_s K} & where \quad k_i \approx 1 \\ -\frac{M}{a_{AlN}K+\frac{nM}{\rho d}\bar{N}} & where \quad k_i \gg 1 \end{cases} \tag{4.5}$$

Here, S_l is the molecule sensitivity factor which depends on the type of liquid. Besides the characteristics of the thin film, the fractional change of the SAW frequency caused by surface perturbations is dependent on the molecular weight, the average molecule concentration in the layer of the cluster, the number of clusters and the density of the liquid. Especially, for the monolayer pattern of the liquid molecules, it depends only on the molecular weight and the total number of molecules on the propagation path.

4.3. EXPERIMENTAL PROCEDURE

4.3.1. DESIGN AND FABRICATION OF SAW DEVICES

THE device used for these experiments are shown in Fig 4.4. It is based on our previous design (see section 3.3.1), but optimized by enlarging the aperture size and imple-

menting a deep cavity for containing very small liquid volumes (up to 0.05 µl). With this modified configuration, a more precise detection mechanism based on physical properties and mass loading as presented above, can be experimentally validated. The dry etching method is used for fabricating anisotropic etch profile of small IDT fingers. The aim of the fabrication of the deep cavity using the SiO_2 thick film, a hydrophilic layer, (see Fig 4.4a) is to prevent contact between the measurement probes and the liquid during the measurement process.

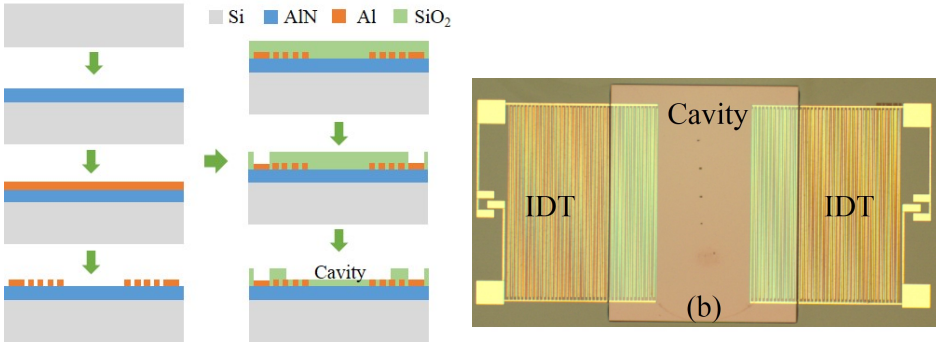

Figure 4.4: (a) Microfabrication process of the device and (b) optical microscope images of the fabricated SAW device.

4.3.2. MEASUREMENT SETUP

THE measurement setup includes an Agilent 8753E network analyzer connected to a RF probe station as illustrated in Fig 4.5. An immediate frequency (IF) bandwidth of 100 Hz is setup to reduce noise sidebands and residual frequency modulation (FM) when the radio frequency (RF) signal is mixed with local oscillator (LO) signal of a local oscillator in the network analyzer. Simultaneously, the highest power, 5 dBm, is applied at the input port, thus the measurement dynamic range is improved [22]. The measured center frequency f_0 is 125.3 MHz.

The evaporation rate of each liquid depends on some physical properties such as boiling point and vapor pressure. In this study, we used eight liquids with different boiling point, vapor pressure and molecule weight, as reported in Fig 4.6a. The evaporation rate and the concentration of the stagnant liquid molecules, ordered from low to high, are shown in Fig 4.6b. Tap water is quite similar to deionized water but the stagnant molecule concentration is denser and the evaporation rate is estimated to be quicker because of the presence of mineral ions (sodium iron, copper, bromide and calcium). Water has the slowest evaporation rate because it has a dipole-dipole interactions O-H with the others molecules. Water molecules are interconnected by the hydrogen bonding O-H which is much stronger than the other hydrogen bonding like H-F or C-H. The dipole-dipole interactions O-C for ACE, IPA and HEP are weaker than for water [17]. All tests are executed at the same environment conditions (like temperature, humidity) and initial conditions for each liquid type (like volume). As the surface tension and the cohesive force of some used liquids are weak, they overflow around the cavity after dropping.

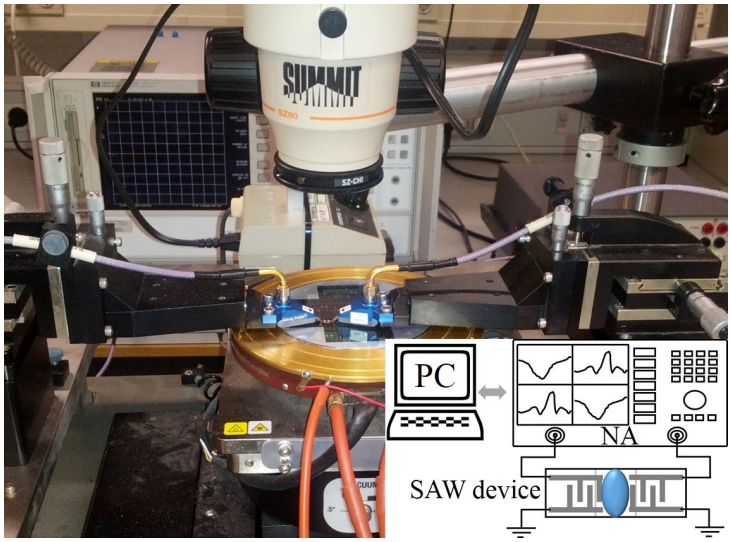

Figure 4.5: The measurement setup of the SAW device for liquid sensing.

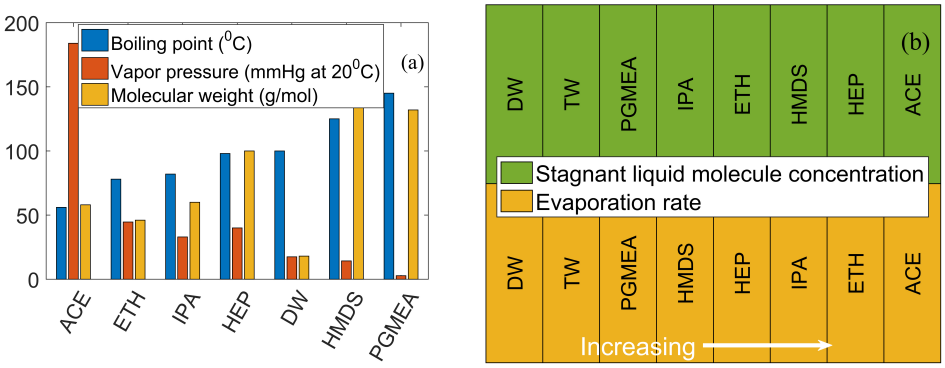

Figure 4.6: (a) Physical properties related to the liquid evaporation and (b) the observed order of the increasing liquid evaporation rate and increasing liquid molecule concentration remaining on the surface, consistent with their physical properties.

4.4. RESULTS AND DISCUSSIONS

OPTICAL micrographs of a droplet evaporation process are shown in Fig 4.7a. For the first 140 seconds, the slow attenuation region, the droplet shape varies rather slowly and then extremely quickly till it evaporates completely in 257 seconds. At the beginning, the measured insertion loss IL has a minor oscillation because of the slight non-uniform energy distribution on the propagation path, the deformation of the contact angle, as well as the slight deformation of the contact radius. In fact, there is a gradual movement of the attenuation. The fraction change of the SAW device is calculated by the difference of sequential insertion losses $\alpha(dB) = \Delta IL = \bar{IL}_i - \bar{IL}_{i-1}$. The fractional

change varies rather slowly like the change of the droplet shape in the slow attenuation region, as shown in Fig 4.7b. When the droplet starts to shrink and changes quickly till it evaporates completely, a fast attenuation occurrence is observed. The duration of these regions depends mostly on contact area deformations of the droplet which is a contact boundary of leaky SAWs from piezoelectric medium to liquid medium. These attenuation regions, in both theoretical and experimental data, are divided by tangent lines with the same factor difference in slope. The region boundary created by a set of tangent lines is a boundary for gradual $d\alpha_1$ and sudden $d\alpha_2$ variation regions of the insertion loss. The comparison of $d\alpha_{1,theory} = -2.78x10^{-1}$ dB to $d\alpha_{1,experiment} = -2.61x10^{-1}$ dB for the first region and $d\alpha_{2,theory} = -6.06x10^{-1}$ dB to $d\alpha_{2,experiment} = -6.75x10^{-1}$ dB for the second region, demonstrates a good match between theory and experiment. The contact area is calculated by theory, experimental data of the fractional change and optical image as illustrated in Fig 4.7c. The Kalman filter method, also called a linear quadratic estimation (LQE), for the object detecting and tracking method is used to calculate contact area of the optical droplet image [23]. The shape of the optical image is a good match compared to the theoretical data and experimental data. Root mean square deviations of the theoretical data with respect to the experimental data are 0.18, 0.3 mm2. If the sensitivity is defined by $S = \frac{d\alpha}{da} = \frac{1}{2}\frac{\rho_f v_f}{\lambda r_0 v_R}$, it is -29.39 dB/μm^2 for DW. This means that for each 1 μm^2 of the evaporated liquid area, the insertion loss will decrease by 29.39 dB. Sensitivities of the device to the rest of liquid samples are shown in Table 4.2.

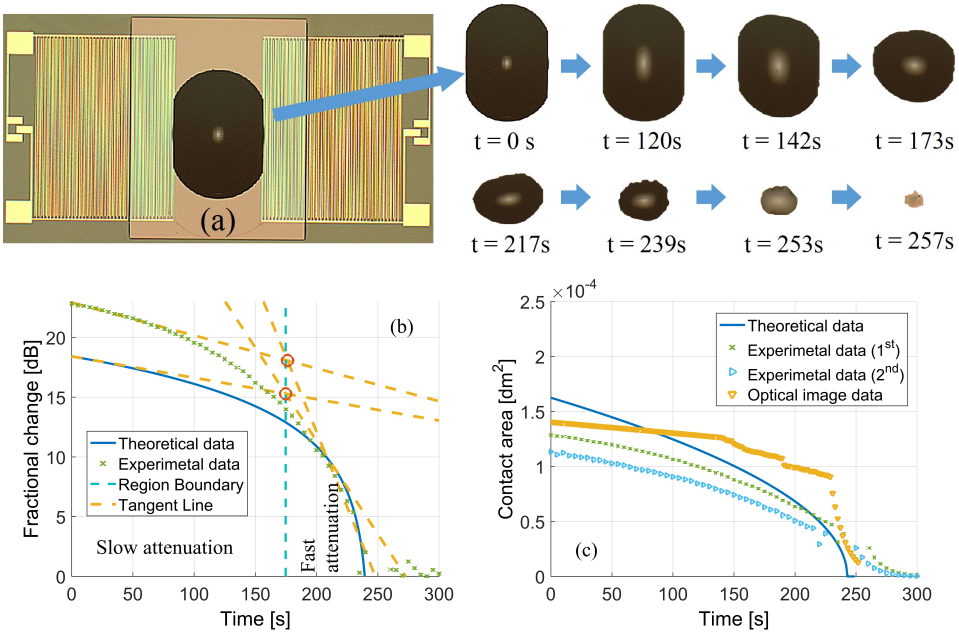

Figure 4.7: (a) The evaporation process of a 0.05 μl droplet, at the middle of the SAW propagation path within 257 seconds. (b) Theoretical and experiment data of the fraction changes in insertion loss. (c) Contact area calculated by theoretical, experimental and optical image data.

This analysis illustrates the fractional change parameter of eight samples in the time domain under the mostly constant ambient conditions as shown in Fig 4.8. Observing the variation of the parameter α of eight liquids in the slow and fast attenuation region during the entire evaporation process, we see that water, which has the slowest evaporation rate, has the longest variation of the insertion loss. Both slow and fast attenuation regions of water are quite evident. The slow attenuation region of DW, TW, PGMEA, HMDS and HEP appears clearly whereas that of IPA, ETH and ACE disappears. Due to the weak surface tension and cohesive force of liquids such as IPA, ETH, ACE and HEP, the droplet fills the entire propagation path. Thus the area contacting the air is larger and makes the evaporation faster. Therefore, the slow attenuation almost disappears and the fast attenuation region is reached quickly. From the fractional change data of each liquid and Eq. 4.5, the deformation of the contact area A can be calculated by $\frac{dA}{dt} = -\frac{2D(c_s - c_\infty)}{\pi \rho_f} g(\theta_0) f(\theta_0)$. For the fast attenuation region, the measured deformation velocities of the contact areas together with the sensitivity values for all liquid tested are reported in Table 4.2. This deformation is caused by the evaporation rate, density, sound speed and shape alteration of the droplet inside the cavity.

Table 4.2: Measured samples of velocity of the shrinking droplet and sensitivity of the SAW device.

Sample	**Deformation velocity of the shrinking contact area ($x10^{-10} m^2/s$)**	**Sensitivity ($dB/\mu m^2$)**
DW	-3.14	-29.39
TW	-3.27	-29.53
PGMEA	-3.76	-31,79
HMDS	-7.84	-34.12
HEP	-8.73	-33.62
IPA	-1.83	-32.87
ETH	-2.92	-32.67
ACE	-4.40	-32.82

The presence of the stagnant liquid molecules leads to change in the mass density on the surface, thus making the output signal frequency shift and the noise increases as compared to the signal before dropping the liquid. Based on the uniform color of recorded micrographs, the form of PGMEA, TW, and DW molecules left are almost monolayer patterns, while that of others has almost multilayer patterns. The variation of the mass density is proportional to the increase of the stagnant liquid molecules on the surface. The generated noise-to-signal ratio (NSR) is shown in Fig 4.9. Micrographs of the propagation path of the SAW device after the evaporation process of IPA, ACE, ETH, HMDS and HEP show rather concentrated molecules. Based on the interference patterns of the liquid meniscus, liquid molecules are packed inside varying multiple layers. Their noise signal ratio oscillates more, especially at the center frequency. Therefore, like the order of the liquids as shown in Fig 4.6b, the noise signal ratio (NSR) of DW, TW and PGMEA is the smallest and sparsest whereas the others have more oscillation at the center frequency, especially ACE because of the obstruction of the many layers of molecules

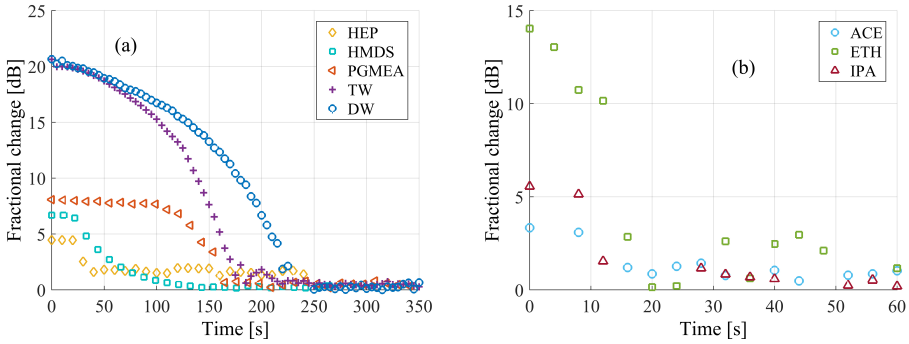

Figure 4.8: Fractional change α in insertion loss for (a) HEP, HMDS, PGMEA, TW and DW; and (b) ACE, ETH and IPA.

and the higher molecule concentration.

Table 4.3: Characteristics of eight liquids identified by the SAW transducer.

Substance	Physical property				Mass loading			
	Slow attenuation		No slow attenuation		Noise		Average frequency shift	
	α_{MAX}	Duration of α>0	α_{MAX}	Duration of α>0	NSR <5dB	NSR >5dB	Δf >100kHz	Δf <100kHz
ACE			14 dB	20 s		x	241 ± 1	
HEP	5 dB	50 s				x	206 ± 9.4	
HMDS	6.6 dB	70 s				x	172 ± 11	
ETH			5 dB	20 s		x		117 ± 4.7
IPA			4 dB	15 s		x		76 ± 8
PGMEA	8 dB	160 s			x			27.3 ± 7.6
TW	20 dB	200 s			x			11.6 ± 4.9
DW	20 dB	250 s			x			0

As the frequency shift is proportional to the molecule concentration of the stagnant liquid on the propagation path, the order of the decreasing frequency shift of ACE, HEP, HMDS, ETH, IPA, PGMEA, TW and DW is in good agreement with the predicted one based on the theoretical analyses presented in chapter4.2.2. The frequency shift is calculated from the frequency difference of the attenuation peaks before and after the liquid evaporation process, and is shown in Fig 4.10. If tap water is referred to a reference sample for noise caused by stagnant liquid molecules on the propagation path, a product (NS_l) of the molecule sensitivity factor and the stagnant liquid molecule, referred to a liquid sensitivity factor, is calculated by the measured frequency shift as shown in Eq. 4.5. Values of 20.66, 17.69, 14.71, 10.29, 6.51, 2.34 and 0 g/cm^2 are in regards to liquid sensitivity factors of ACE, HEP, HMDS, ETH, IPA, PGMEA and DW, respectively. It demonstrates a match of optical images (see Fig 4.9) and experimental data (see Fig 4.10)

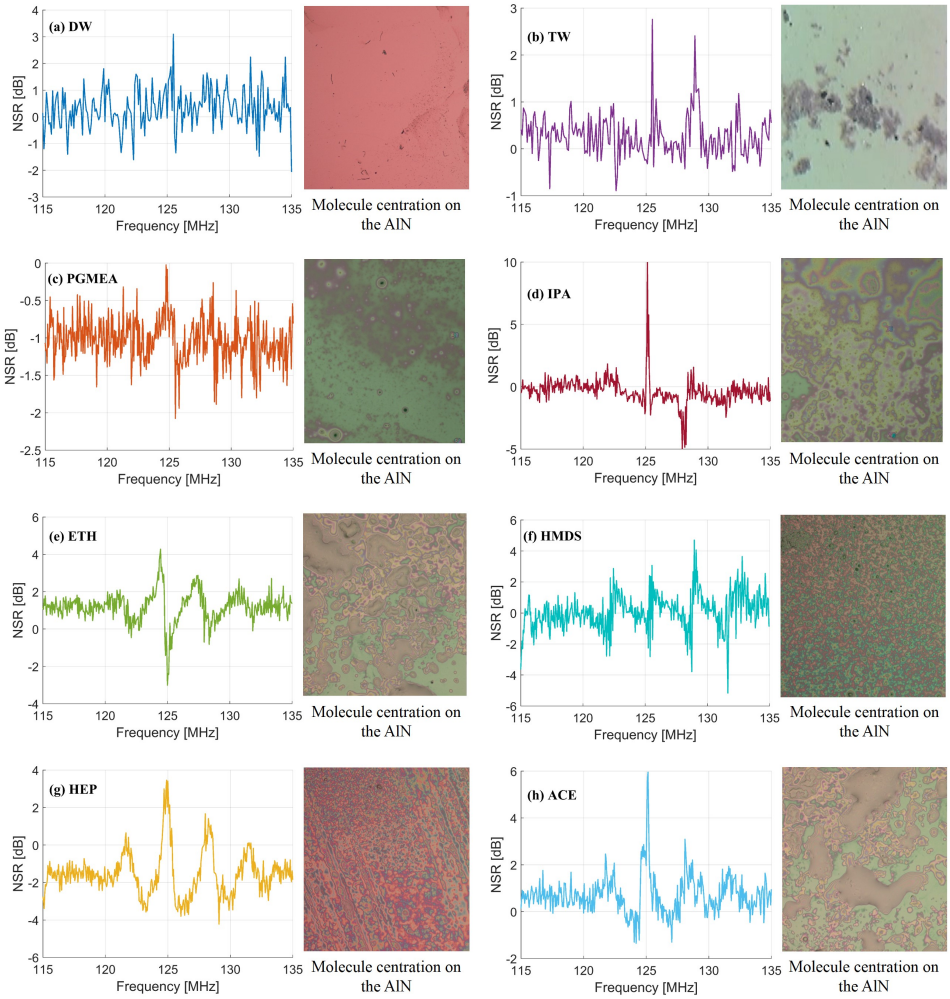

Figure 4.9: Noise signal ratio (NSR) of the output signal before and after dropping the liquid for (a) DW, (b) TW, (c) PGMEA, (d) IPA, (e) ETH, (f) HMDS, (g) HEP and (h) ACE.

of eight liquids. For quite different samples like DW and IPA, it can be detected by a parameter like the presence of slow attenuation region of the fractional change, variation duration of the fractional change or noise. For quite similar samples like ACE and IPA or DW and TW, the detection process needs more observations like deformation velocity of the contact area, noise and frequency shift. Table 4.3 summarizes the characteristics of the eight liquids tested, demonstrating that it is indeed possible to identify these liquids using the AlN-based SAW transducer we developed.

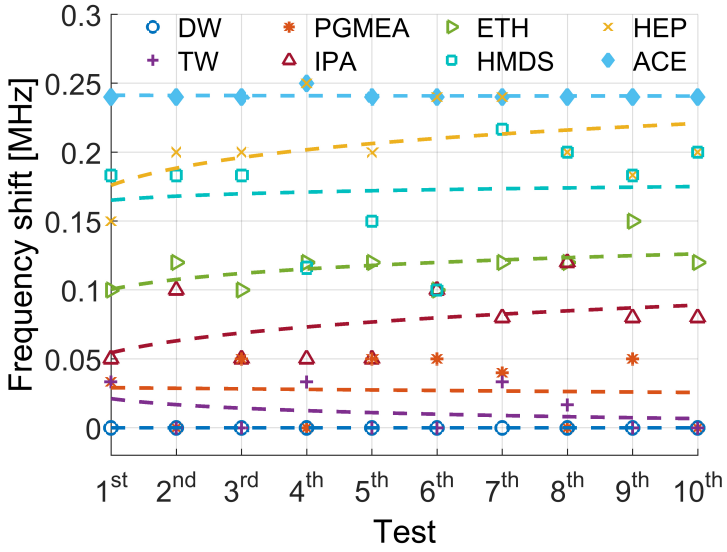

Figure 4.10: Frequency shift of the SAW transducer for different liquids tested.

4.5. CONCLUSION

THIS chapter presents a potential method for identifying liquid samples of microliter volumes in microfluidic biosensors. It is based on a surface-acoustic-mode AlN transducer using two detection mechanisms, physical properties and mass loading, corresponding to the shrinking droplet radius and stagnant liquid molecules during and after the evaporation process of the liquid. The fraction change of the attenuation is proportional to physical properties, such as evaporation rate, sound speed and density of the liquid. The concentration of stagnant liquid molecules produces a change in the surface mass of the micro-electro-mechanical transducer, which causes a frequency shift and increases signal noise at the receiver after the liquid evaporation process. Experimental results of the oscillation magnitude and duration of the fraction change α, noise-to-signal ratio NSR and frequency shift Δf are in good agreement with the theoretical analysis, thus validating the effectiveness of the proposed AlN-based SAW device for the identification of the type of liquid under investigation.

REFERENCES

[1] D. B. Go, M. Z. Atashbar, Z. Ramshani, and H.-C. Chang, *Surface acoustic wave devices for chemical sensing and microfluidics: a review and perspective,* Anal. Methods (2017).

[2] S. J. Martin, A. J. Ricco, G. C. Frye, T. M. Niemczyk, and I. Adhihetty, *Sensing in liquids with sh plate mode devices,* in *Ultrasonics Symposium, 1988. Proceedings IEEE 1988* (1988).

[3] S. Shiokawa and K. Jun, *Surface acoustic wave sensors,* Japanese Journal of Applied Physics (2004).

[4] S. Shiokawa, Y. Matsui, and T. Ueda, *Liquid streaming and droplet formation caused by leaky rayleigh waves,* in *Proceedings, IEEE Ultrasonics Symposium* (1989).

[5] G. Zhang, *Nanostructure-enhanced surface acoustic waves biosensor and its computational modeling,* Journal of Sensors (2009).

[6] T. Bui, B. Morana, A. Tran, T. Scholtes, T. C. Duc, and a. P. M. Sarro, *Saw device for liquid vaporization rate and remaining molecule sensing,* in *IEEE-SENSORS2015* (2015).

[7] T. H. Bui, D. T. Bui, and D. T. Chu, *Microfluidic injector simulation with fsaw sensor for 3-d integration,* Instrumentation and Measurement, IEEE Transactions on (2015).

[8] T. H. Bui and D. T. Chu, *Multilayer saw device for flow rate sensing in a microfluidic channel,* in *SENSORS, 2013 IEEE* (2013).

[9] P. Kostial, *Surface acoustic wave measurements of evaporation rate,* Applied Acoustics (1996).

[10] K. Lange, B. E. Rapp, and M. Rapp, *Surface acoustic wave biosensors: a review,* Analytical and Bioanalytical Chemistry (2008).

[11] J. Ballantine, R. M. White, S. I. Martin, A. J. Ricco, E. T. Zellers, G. C. Frye, and et al., *Acoustic Wave Sensors, 1st Edition: Theory, Design, & Physico-Chemical Applications* (USA: ACADEMIC PRESS, 1997).

[12] S. Semenov, V. Starov, and R. G. Rubio, *Droplet wetting and evaporation,* (Oxford: Academic Press, 2015) Chap. Chapter 21 - Droplets with Surfactants A2, pp. 315–337.

[13] J. Kondoh, N. Shimizu, Y. Matsui, M. Sugimoto, and S. Shiokawa, *Development of temperature-control system for liquid droplet using surface acoustic wave devices,* Sensors and Actuators A: Physical (2009).

[14] J. Kondoh, T. Muramatsu, T. Nakanishi, Y. Matsui, and S. Shiokawa, *Development of practical surface acoustic wave liquid sensing system and its application for measurement of japanese tea,* Sensors and Actuators B: Chemical (2003).

[15] F. Bender, R. E. Mohler, A. J. Ricco, and F. Josse, *Identification and quantification of aqueous aromatic hydrocarbons using sh-surface acoustic wave sensors,* Analytical Chemistry (2014).

[16] Z. Ramshani, A. S. G. Reddy, B. B. Narakathu, J. T. Wabeke, S. O. Obare, and M. Z. Atashbar, *Sh-saw sensor based microfluidic system for the detection of heavy metal compounds in liquid environments,* Sensors and Actuators B: Chemical (2015).

[17] M. Bishop, *Introduction to Chemistry* (Prentice Hall, 2001).

[18] T. L. Berman, A. S. Lavine, F. P. Incropera, and D. P. Dewitt, *Introduction to Heat Transfer* (John Wiley & Sons: New York, 2011).

[19] F. D. Lopez-Hilfiker, C. Mohr, E. L. DAmbro, A. Lutz, T. P. Riedel, and C. J. Gaston, *Molecular composition and volatility of organic aerosol in the southeastern u.s. implications for iepox derived soa,* Environmental Science & Technology (2016).

[20] P. E. Liley, G. H. Thomson, D. G. Friend, T. E. Daubert, and E. Buck, *Physical and Chemical Data* (The McGraw-Hill Company, 1999).

[21] G. Wyllie, *Evaporation and surface structure of liquids,* in *Proceedings of the Royal Society of London A: Mathematical, Physical and Engineering Sciences* (1949).

[22] Agilent, *Agilent Network Analyzer Basics*, Tech. Rep. (Agilent, 2004).

[23] B. S. Yaakov, L. Rong, and K. Thiagalingam, *Estimation with Applications to Tracking and Navigation* (New York: John Wiley & Sons, 2001).

5

INTEGRATED SAW LIQUID SENSING SYSTEM

This chapter presents a novel liquid microsensor based on an on-chip aluminum nitride surface acoustic wave (SAW) device. The device miniaturized and integrated on a printed circuit board (PCB) is used for sensing the liquid flow. The mechanism is based on pressure and liquid density changes of the liquid flowing inside the microhole during the evaporation process. Two experiments are performed to observe each effect, pressure and liquid density change inside the microhole, separately. In the first one the liquid density is varied by inserting samples, such as pure aluminum, gold, and human hair inside the hole. For the second one, the pressure effect is validated by pumping air from a chamber underneath the hole and then detecting the response related to the influence of the pressure on the thick membrane of the SAW device.

5.1. INTRODUCTION

SOME research and our experiment above showed that the SAW device is quite sensitive to the microliter volume liquid [1–4]. For the microliter volume liquid, energy attenuated into liquid medium even can drive, atomize droplet [5, 6]. This transferred energy depends on the density and viscosity of the liquid medium, on the contact area and contact angle between the piezoelectric layer and the liquid medium [3, 7, 8]. Liquid medium is often placed on the propagation path for actuation, manipulation and sensor applications of the SAW device [7, 8]. A cavity is proposed for containing liquid medium [1, 9, 10]. This controls the contact area between the piezoelectric and the liquid medium which makes uniform and stable experimental results. So a hole is proposed for bringing liquid medium which possibly contacts surface acoustic waves at the nozzle. This only uses benefits of the formerly proposed cavity, but also makes manipulation of liquid contacting the piezoelectric substrate easier. It avoids excessive attenuation of Rayleigh component of the SAW device into a liquid medium that leads to no signal at the receiver. If the SAWs are generated on low quality piezoelectric material, the entire SAW energy is attenuated into the liquid medium, which is a disadvantage of the horizontally placed microhole. Besides, the contact of the SAW configuration with the horizontally placed microhole and the liquid medium is often fabricated as a flat configuration, while the shape of the vertically placed microhole is more flexible (eg. circle). It is suitable for applications which have liquid flowing inside a tubular structure (eg. injector).

A propagation path between input and output IDTs of the typical surface acoustic wave (SAW) device is often non-interrupted path. Disturbances placed on the surface of the SAW sensor affect the signal and consequently can be detected. However, in some cases, trapping micro-particles in the droplet and sensing the presence of particles inside a droplet, a vertical impact area like a hole or a cavity placed on the propagation path, is preferred [9–12]. This can make device fabrication more complex. To form the vertical channel, a long etching process is needed. Consequently, a thicker masking layer is applied and subsequently removed, which can cause unwanted edge roughness of the cavity and alter its shape [13, 14]. This can result in unwanted frequency shift, excessive energy loss, non-uniform and rough surface, cracks on the structure of the piezoelectric film. However, this vertical structure crossing the propagation path can be realized in various sizes and shapes of defining the microhole, which makes it possibly to investigate different types of liquids or particles. In the proposed vertical structure, a different attenuation is detected when Raleigh damping is radiated into the contact area between the piezoelectric layer and the liquid medium confined in the microhole.

The novel on-chip vertical structure for microfluidic applications of SAW sensors proposed is schematically shown in Fig 5.1. It consists of an aluminum nitride (AlN) – based SAW sensor with an embedded microhole positioned on the middle of the propagation path. The device in diameter is mounted on a printed circuit board (PCB). The generated acoustic waves from the input IDTs concentrate mainly on the surface and travel to the micro-size hole. The Raleigh component can be perturbed from effects inside the microhole thus changing the SAW response. Therefore, first, we study the expected effects on the microhole filling through the simulation of the liquid evaporation phenomenon. The parameters considered are the pressure on the wall of the microhole and the changeable concentration of the liquid at the nozzle and at the wall caused

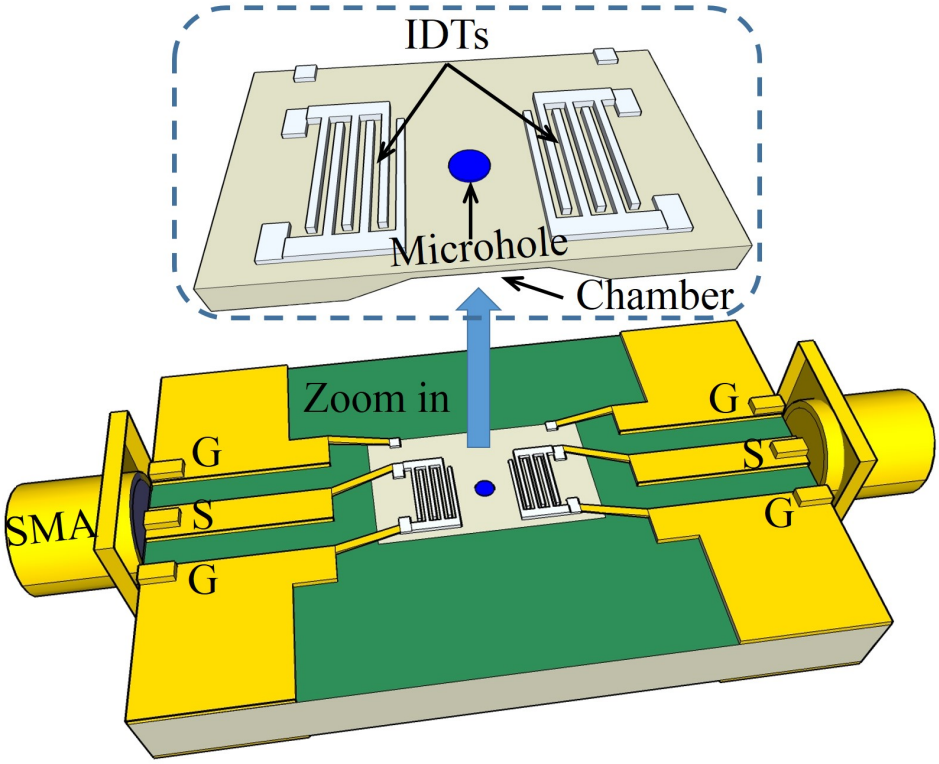

Figure 5.1: 3D schematic of the on-chip SAW device with the vertical microhole on the middle of the propagation path.

by capillary evaporation. Then, the evaporation of the liquid inside the hole is experimentally investigated. It is in fact possible to observe the change of the output voltage during the evaporation of the liquid inside the nozzle. Both the variation in pumping air pressure and the addition of micro-size samples inside the microhole are studied. In this way, the SAW response is correlated to changes of pressure and density of the liquid inside the microhole.

5.2. EFFECT OF THE INTERRUPTED PROPAGATION PATH ON TRANSDUCER RESPONSE

MICROCAVITIES or microholes are rarely implemented in commercial devices as they negatively affect the performance of the SAW devices which is strongly dependent on the smoothness of the piezoelectric surface and the anisotropy of the etched profile. In fact, the etching of these deep microcavities or microholes causes unwanted surface roughness in the piezoelectric thin film as illustrated in Fig 5.2. Moreover, over-etching of the layer or lack of anisotropy of the cavity sidewalls result in the diffracted SAW beam being fed back to the input IDTs or being disturbed, thus leading to unwanted changes

in both signal magnitude and operating frequency.

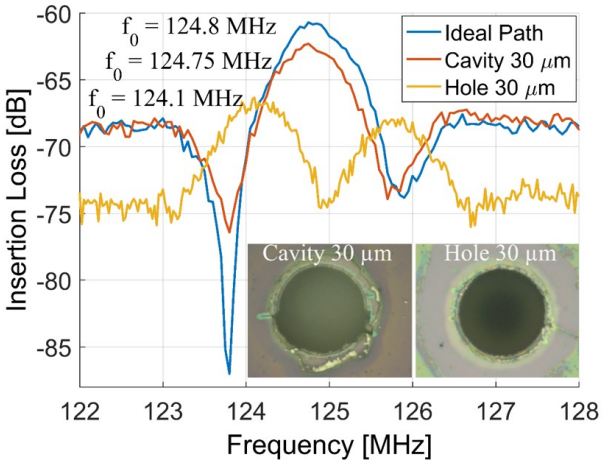

Figure 5.2: Frequency shift of SAW devices having a 30 µm diameter microcavity or microhole as interruption on the surface, compared to the ideal SAW device.

However, by using protecting sublayers patterned on the piezoelectric layer, it is possible to fabricate deep microcavities and microholes with an acceptable attenuation in signal magnitude and without the frequency shift. Interruptions such as microholes with a diameter of 30, 50 and 100 µm placed on the propagation path of the Aluminum Nitride SAW devices are prepared and the sensor response is compared to the one of a conventional SAW device in both simulation and experiments.

The SAW device based on the AlN thin film is modeled in three-dimensional geometry in the time domain. As the medium inside the microholes is air, Rayleigh waves travel through the contact coupling the air and piezoelectric medium. The model with 3 finger pairs on each IDT is meshed and computed by the finite element analysis (FEA) method. To reduce the high nonlinearity of the computation and the large storage in memory required, only an AlN film with a thickness much smaller than the wavelength, is set as substrate.

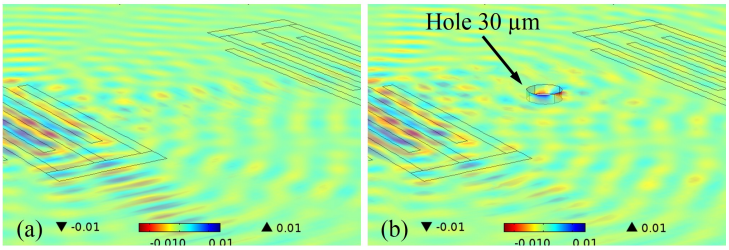

Figure 5.3: Rayleigh displacement of the SAW device with (a) the ideal propagation path and (b) the path interrupted by a 30 µm diameter microhole.

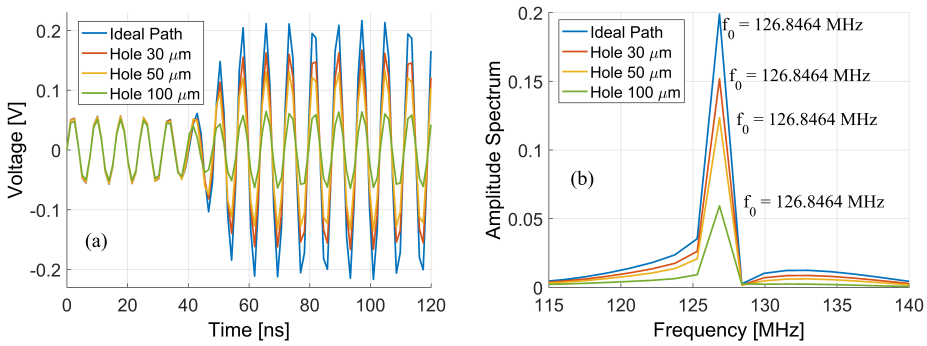

Figure 5.4: The output voltage in the (a) time and (b) frequency domain corresponding to the ideal path, and to the path interrupted by the microholes of 30, 50 and 100 µm in diameter.

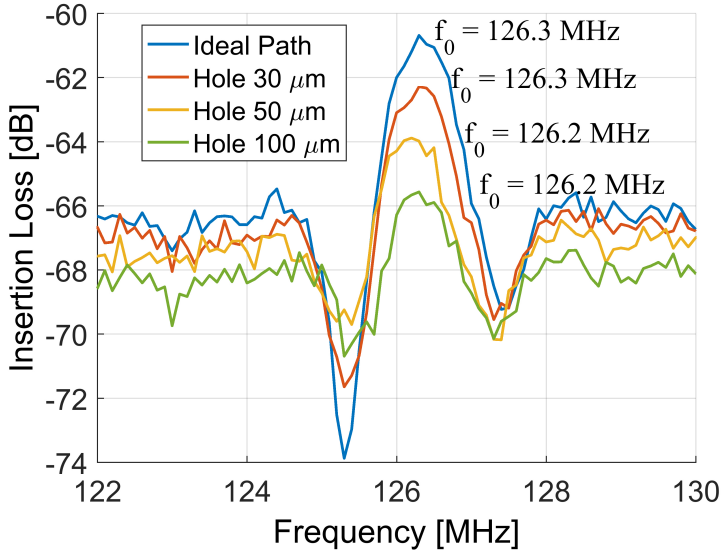

Figure 5.5: The insertion loss of the SAW devices corresponding to the ideal propagation path and the interrupted propagation path for the three microhole diameters (30, 50 and 100 µm) investigated.

The FEM simulation results (Fig 5.3) show that the Rayleigh-SAWs (R-SAWs) traveling through the interrupted path are not diffracted or fed back to the input IDTs. The output voltage versus the time and in the frequency domain is shown in Fig 5.4. The center frequency is not influenced by the presence of the microholes, but there is a strong effect on the signal magnitude. This effect is due to the complete loss into the medium (air). This also corresponds to an insertion loss of the SAW devices measured experimentally. The magnitude reduces with increasing diameter of the microholes, but an insignificant change in the operating frequency was recorded (see Fig 5.5). This shows the fabrication

technology for the realization of an arbitrary interruption in the propagation path to achieve the smallest frequency shift is possible. The magnitude attenuation depends on the size of the interruption on the propagation path, ideally 30 or 50-µm diameter size of the hole or cavity are preferred due to the smaller attenuation. To increase the contact area, we selected 50-µm diameter size for the hole.

5.3. EFFECT OF CHANGEABLE MEDIUM OF THE INTERRUPTED PROPAGATION PATH ON TRANSDUCER RESPONSE

THE liquid inside the microhole on the middle propagation path of the SAW device is studied. The influence of the liquid inside the microhole is analyzed through the evaporation phenomenon of the sample. The evaporation process of deionized water is a slow-time phenomenon which is very useful to observe the general SAW response to the changes in the liquid through the microhole. We assumed that the hole is filled with water and surrounded by air. The air flowing through the hole causes the evaporation of water. Three effects are considered in this model: the turbulent flow of air around the hole, heat transfer in all domains, and transport of water evaporation in air. The velocity and pressure field in computing are independent of the air temperature and moisture of the environment. During the evaporation, the values of mass concentration and pressure at time t = 0, 5, 10 and 20 minutes are reported in Fig 5.6a. These values are measured at the top surface of the liquid. The non-symmetric, changeable distribution of the surface shows the non-uniformity of the liquid concentration. The color of the contour shows the pressure also varies. The liquid concentration versus time is shown in Fig 5.6b.

As known, both density and concentration describe the amount of a solution per unit of volume. While density measures mass per volume, concentration measures the number of moles of atoms per volume. The relation between them can be calculated by:

$$\begin{aligned} Density &= \frac{mass}{volume} = \frac{concentration * volume * molar\_mass}{volume} \\ &= concentration * molar\_mass \end{aligned} \tag{5.1}$$

So, changing the concentration of a solution changes its density. As shown in Fig 5.6b, the reduction of the liquid molecules concentration over time during the evaporation process is similar to the decrease of the liquid volume. Therefore, to investigate the on-chip SAW response to concentration changes, the evaporation process of the liquid inside the hole is studied.

5.4. DESIGN AND FABRICATION OF THE SENSOR PACKAGING

THE proposed piezoelectric microdevice with the interrupted propagation path shown in Fig 5.7 consists of input and out IDTs patterned on a low stress, 1-µm-thick AlN layer and a microhole in the propagation path. The chosen substrate is a silicon wafer with very high resistivity (more than 1000 Ωcm) as this results in a higher quality of AlN piezoelectric grown on it [15]. The Silicon Nitride (SiN) mask layer (Fig 5.8a) for the KOH etching step used to form the hole or cavity, is deposited by low pressure chemical vapor deposition (LP CVD). The AlN thin film is produced by reactive sputtering using a low

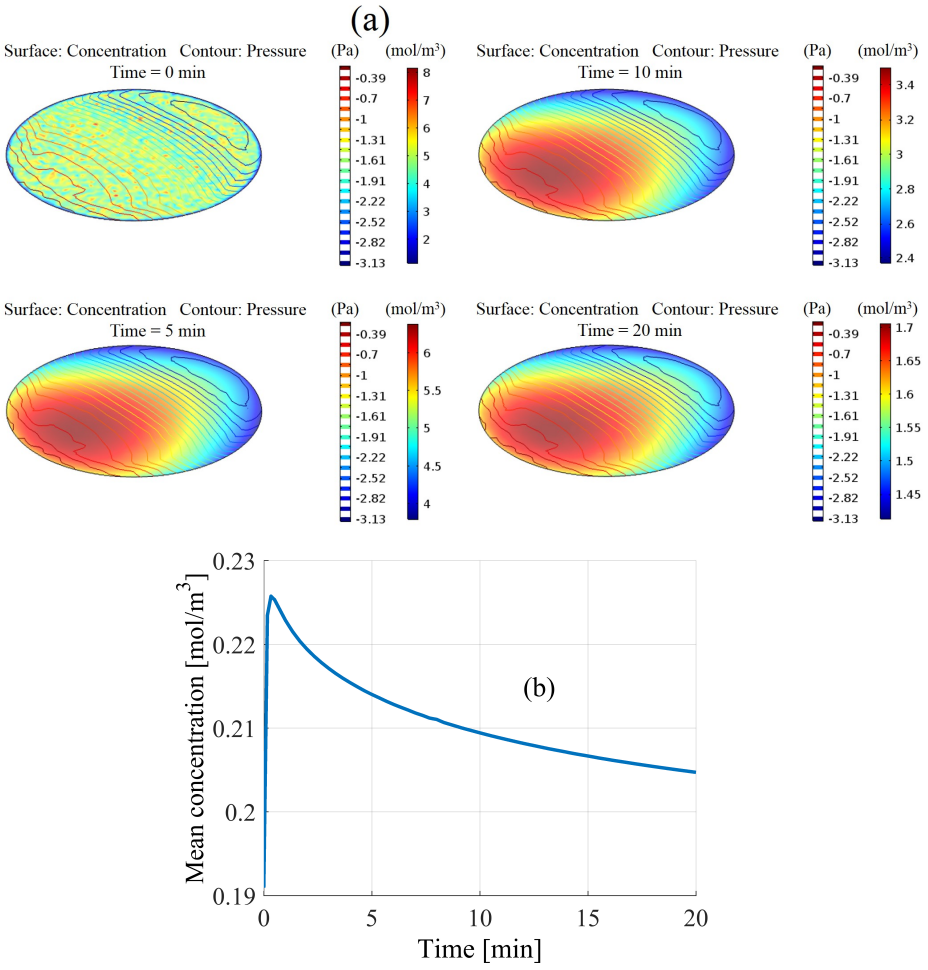

Figure 5.6: (a) Concentration and pressure of the liquid at the surface and (b) average concentration of liquid at the surface from $t = 0$ (water starts to evaporate) to $t_f = 20$ minutes.

deposition rate for low stress and a higher deposition temperature (400^0C) for good film crystallinity (Fig 5.8c). Before the reactive sputtering step of the Aluminum (Al) thin film used for the IDTs, plasma-enhanced chemical vapor deposition (PE CVD) of 100 nm SiN (Fig 5.8d) is carried out. The purpose of this layer is to protect the AlN thin film during the inductively coupled plasma (ICP) etching of the Al IDTs (Fig 5.8e). The microhole of 50 µm diameter is generated by etching alternately layers, SiO_2, Al, SiN, AlN and Si (Fig 5.8g and Fig 5.9a, b). As the SAWs cannot propagate beyond twice the wavelength, the substrate should be thicker than twice the wavelength. Therefore, we fixed the depth of the microhole to 80 µm (Fig 5.8j and Fig 5.9c).

The AlN thin film is etched by ICP technology to achieve highly anisotropically etched

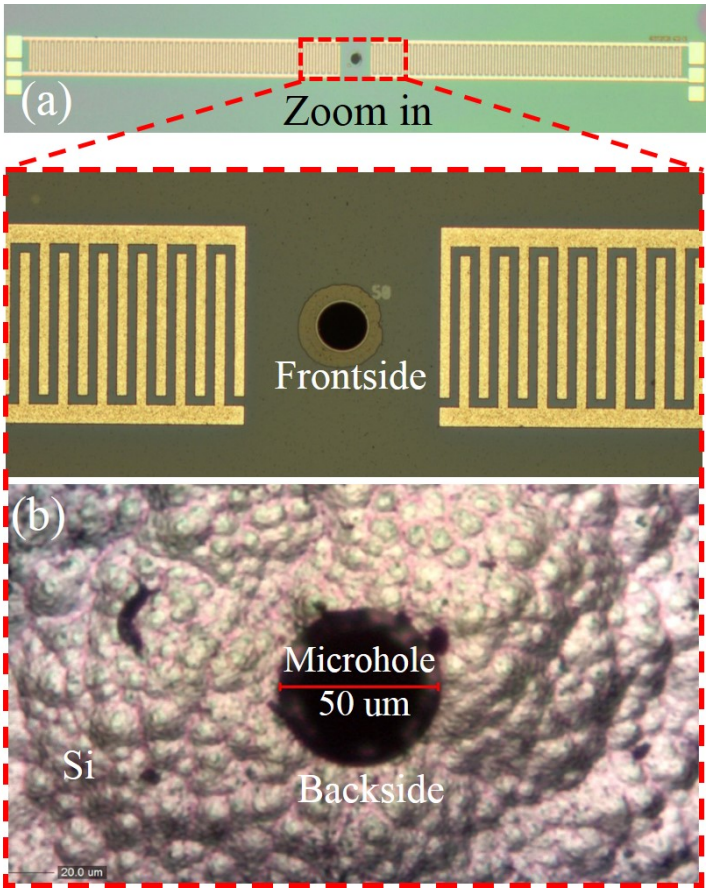

Figure 5.7: The fabricated SAW device: (a) Optical image of the chip; (b) close-up of the microhole at the frontside (top) and backside (back) of the chip.

sidewalls as shown in Fig 5.7b, c. During the following etching steps, the AlN layer is always protected by the SiO_2 layer or the special wafer holder for KOH to avoid over-etching (Fig 5.8g, h, j, and k). The complete microfabrication process is schematically shown in Fig 5.8 and the design parameters of the SAW device with the arbitrarily interrupted propagation path are reported in Table 5.1.

The overall device size is 1000 µm x 4800 µm. The microhole size (50 µm) of one third of the aperture is appropriate to achieve acceptable attenuation of the interrupted propagation path as shown in Fig 5.7. The fabrication and packaging process for the SAW sensor chip are based on integrated circuit (IC) compatible and packaging technologies. For 10 µm pitch of IDT arrays, an operating frequency of 125.9 MHz is measured. To integrate fluidics for sample handling, the chip is mounted on a dedicated PCB. To get a better performance, a 50-Ω impedance grounded-coplanar-waveguide for RF signals is considered for connection between PCB and the pads of the SAW device [16]. The signal

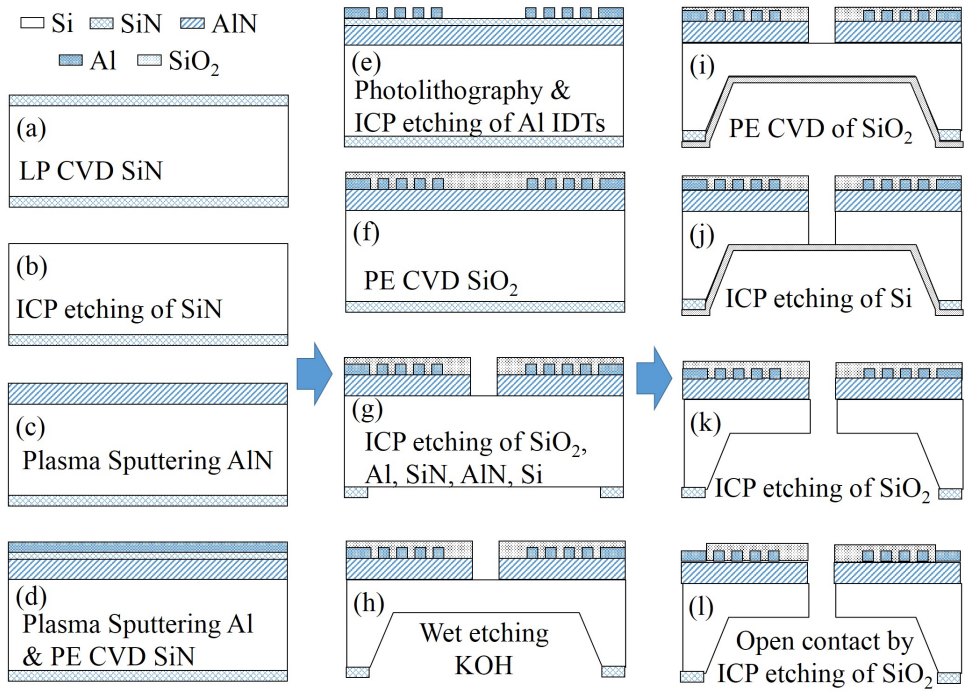

Figure 5.8: The fabrication flowchart of the SAW device with the interrupted propagation path: (a) LP CVD SiN deposition, (b) dry etching of SiN, (c) AlN sputtering, (d) PE CVD SiN deposition and then Al sputtering, (e) photolithography and etching of Al IDTs, (f) PE CVD deposition of the protecting SiO_2 layer, (g) dry etching of the SiO_2, Al, SiN, AlN layers stack on the frontside and of SiN on the backside (h) wet etching of Si, (i) PE CVD SiO_2 deposition, (j) dry etching of Si, (k) dry etching of SiO_2 and (l) contacts opening by dry etching of SiO_2.

Table 5.1: Design parameters of the SAW device.

Parameters	**Value**	**Unit**
Wavelength $\lambda = 4d$ (d is the finger width)	40	µm
IDT finger height	0.5	µm
Aperture	150	µm
Number of the input and output IDT fingers N	50x50	
Theoretical center frequency f_0	126.9	MHz
Propagation length	200	µm
Diameter of microhole	50	µm
SiN mask layer thickness on the wafer frontside	100	nm
SiN mask layer thickness on the wafer backside	2	µm
SiO_2 mask layer thickness on the wafer frontside	2	µm
SiO_2 mask layer thickness on the wafer backside	600	nm

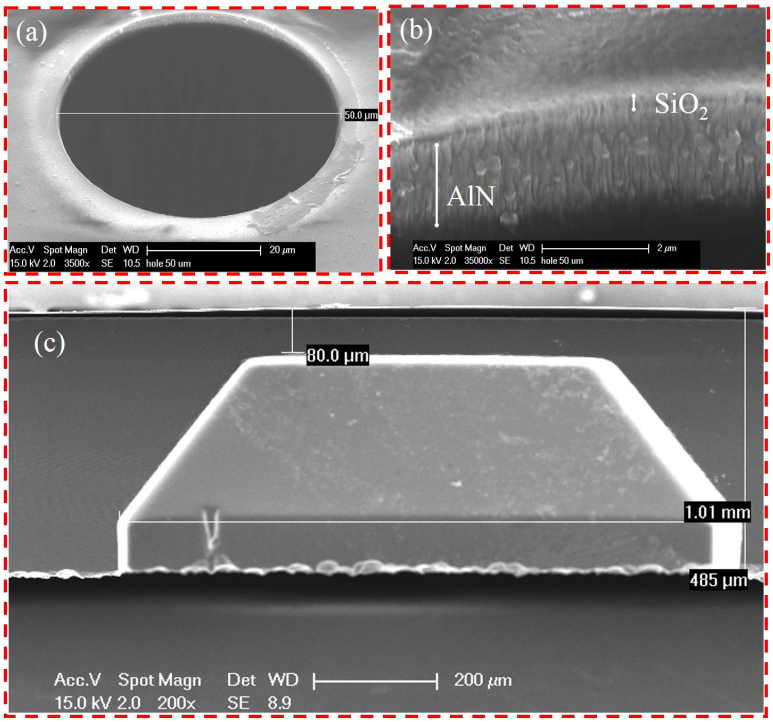

Figure 5.9: (a) SEM image of the microhole, (b) and (c) cross-section views of the hole, clearly showing the piezoelectric AlN layer and the oxide insulation layer.

is driven by the microstrip line at the top, while the other ground lines at the top and the plane at the bottom are connected to the ground.

5.5. EXPERIMENTAL SETUP

THE measurement system for testing the evaporation process of the liquid is illustrated in Fig 5.10a. The system includes top IP camera, network analyzer connected to computer. Deionized water (DW) is pumped into a chamber and then the microhole is filled. One SMA (subminiature version A) 50-Ω RF (radio frequency) coaxial connector is connected between the input of the circuit and the port of the network analyzer. The other is connected between the output of the circuit and the oscilloscope. Network analyzer plays a role in generating input signal of 5 dBm for the device while the oscilloscope collects output signal of the device. The changing meniscus of the liquid inside the hole is tracked and recorded by the top camera. All data is collected by the computer connected to the equipment.

A chamber is created at the backside of the chip and sealed by the acrylic plate as shown in Fig 5.10b. It behaves as a channel for inserting liquid/air from the outside into the microholes as shown in Fig 5.10b. For the pressure test, a pump is used for changing the pressure inside the microhole.

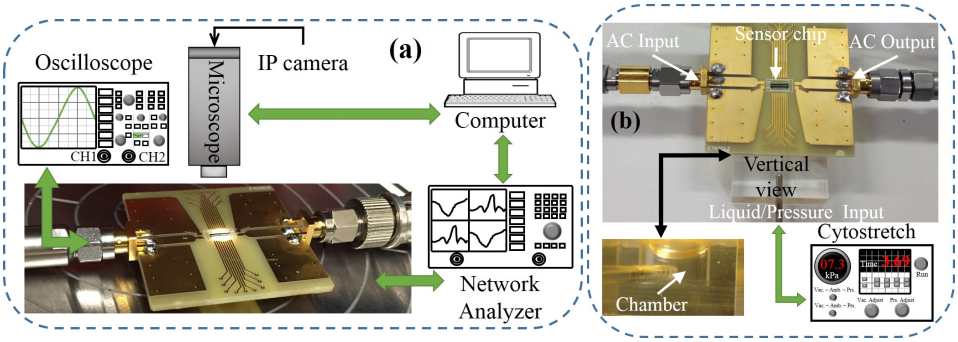

Figure 5.10: Measurement setup for testing (a) evaporation and (b) changeable pressure and density.

For the density variation experiment, this chamber avoids evaporation of the liquid in the environment. The DW level for testing is kept constant inside the microhole. Several micro-objects, such as gold (Au), aluminum (Al) wire and human hair fiber are added into the microhole to introduce a change in the mass density at the nozzle.

5

5.6. RESULTS AND DISCUSSIONS

BASED on the simulations results presented above, changes in pressure and liquid density at the wall of the microhole can occur when the liquid evaporates. As known, among piezoelectric transducers, the SAW device is very sensitive to perturbations on the surface. The experimental results in this section show that it does respond to small changes in pressure and density based on the evaporation process of the liquid, on air pumping and on the addition of samples inside the liquid.

5.6.1. EXPERIMENT OF THE EVAPORATED LIQUID INSIDE MICROHOLE

DEMI-WATER is filled from the bottom of the SAW device. The wall of the hole is considered as a hydrophobic layer because of the combination of the aluminum nitride and silicon oxide. As a wetting fluid in a capillary bridge [17–19], the water meniscuses with the different opening area at both sides are illustrated in Fig 5.11. A liquid bridge between two meniscuses is generated and balanced by the capillary-bridge forces in equilibrium. The initial image of the liquid capillary bridge inside the hole can be observed in the first image of Fig 5.12. As the simulation results show, the evaporation of the liquid can cause changes in pressure and density inside the microhole. The evaporation phenomenon leads to a decreased pressure inside the liquid bridge and surface tension force exerted around the annulus of the meniscus. Also, concentration of the liquid is changed because of the phase transformation of liquid into gas molecules.

As the opening area at the bottom of the device is much larger than the opening area (microhole) at the top of the chip; the evaporation process takes place at the bottom. This causes an unbalanced status of the liquid capillary bridge and pressure difference between frontside and backside of the hole. This pressure is proportionally inversed to the radius of the meniscus. At the initial time, the change in radius is very small, thus the influence on the surface can be ignored in the stable phase (yellow region) in Fig

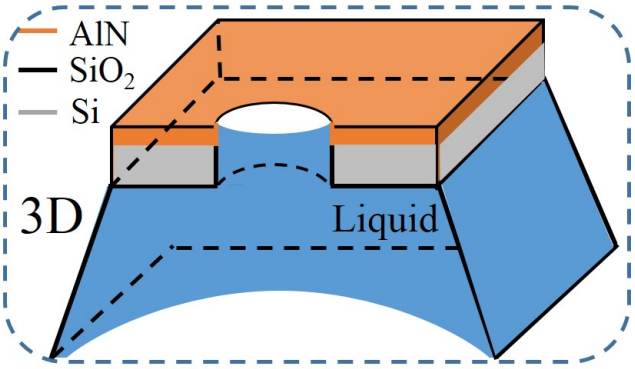

Figure 5.11: 3D sketch of the liquid inside the chamber during the evaporation experiment.

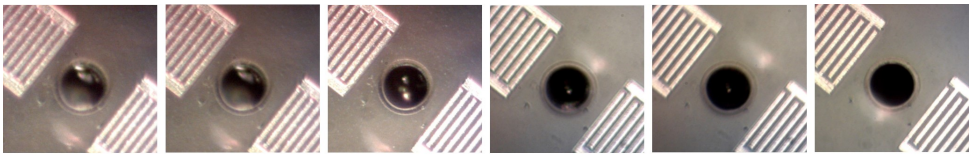

Figure 5.12: Images of DW inside the hole during the evaporation experiment.

5.13. The output voltage of the SAW device is collected at intervals of 5 seconds until the balance between te two free surfaces is reached. Thanks to the variable liquid capillary force on the two free surfaces during the evaporation, the envelop of the output voltage drops gradually down from 33.88 mV at stable status (yellow line) to 29.08 (violet line), 17.88 (green line) and 16.28 (light blue) mV. The evaporation process at the hole shown in Fig 5.12 is relative to the violet and green region in Fig 5.13. The plot shows that the output signal turns down quickly, an indication of the strongest influence on the wall of the microhole at this stage.

5.6.2. PRESSURE CHANGE

THE next experiment is intended to induce external pressure inside the hole. To achieve this, the air is pumped inside through a long pipe to avoid the solid membrane motion. Because of the long path as shown in Fig 5.14a, the pressure values generated by the pump are not relative to the pressure on the wall of the microhole. These values are used to observe the sensitivity of the device to the small change of pressure on the hole. These values are small enough to avoid any unexpected effect on the membrane. Fig 5.14b shows the changed output voltage of the SAW device when a pump provides a short pulse of 3.3 and then 6 kPa. The analytic envelop of the output voltage drops down from 3.8 mV at pressure of 6 kPa to 2.4 mV at pressure of 0 kPa. With the smaller pressure pulse, a smaller increase in the output voltage envelope (V_e = 3.6 mV) is observed.

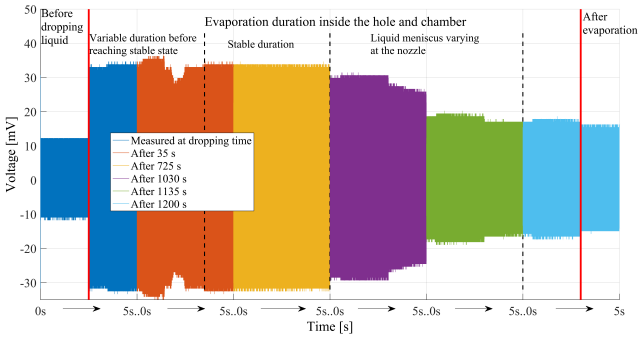

Figure 5.13: Voltage response of the SAW device during the whole evaporation process.

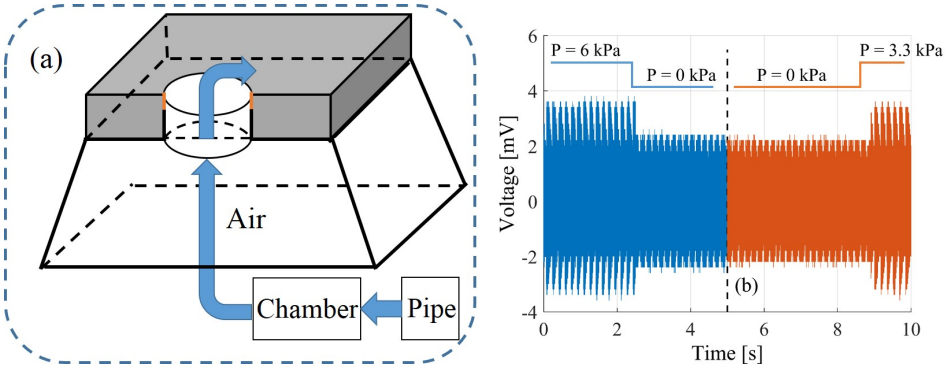

Figure 5.14: (a) Schematic drawing illustrating the air flow path: external air is pumped through a long pipe, the chamber and then reaches the microhole of the SAW device and (b) voltage response when the pressure inside the hole is changed.

5.6.3. DENSITY CHANGE

To evaluate the effect of the change in density, considering that the measurement system is stable and does not depend on measurement duration, the data can be collected by the network analyzer. To change density, some samples, Au, Al wire and human hair fiber are inserted inside the embedded microhole. The samples have different size and density, as reported in Table 5.2.

Fig 5.15 reports the attenuation of the insertion loss in magnitude and phase when three samples are inserted inside the microhole and compared to the case of only pure DW. As the hair fiber inside the embedded microhole is a little larger than the Au or Al sample, its effect on the oscillation of the mechanical waves on the propagation path can be distinguished more clearly than for the other samples. The change in density affects both the magnitude and phase of the insertion loss. Phase differences of 3.55°, 2.72° and 2.62° and magnitude attenuations of insertion loss of 0.46, 0.44 and 0.55 dB are obtained for Al, Au and hair fiber, respectively.

Table 5.2: Physical parameters of samples [20–22].

Parameter	Al	Au	Hair
Size (µm)	33.0	32.1	40.2
Density (g/cm^3)	2.7	19.32	1.32

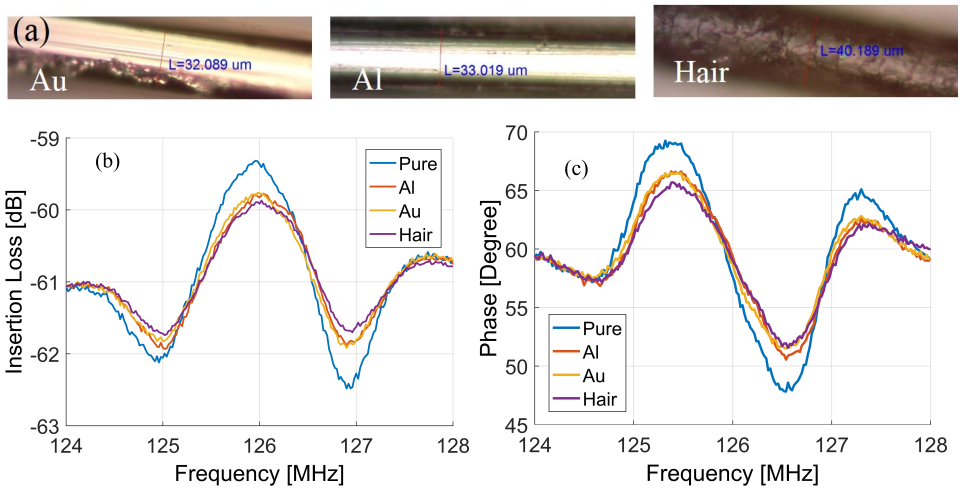

Figure 5.15: : The effect of density change on the SAW device output: (a) The three materials, gold, aluminum, and hair fiber used to change the liquid density; (b) magnitude and (c) phase of the insertion loss of the SAW sensor chip related to the density changes.

5.7. CONCLUSION

THE novel on-chip SAW device equipped with a vertical microhole is sensitive to changes in pressure or density of the liquid inserted in the microhole. Initial experimental results are in a good agreement with the expected large sensitivity of the SAW device when physical parameters, such as density and pressure, are changed. The testing principle is based on the evaporation capillary phenomenon between different free surfaces which affects the concentration of liquid inside the microhole and the pressure on the wall of the microhole. The output signal changes when small changes in both pressure and liquid concentration take place during the long evaporation process of the liquid. Moreover, the SAW response can be measured when either pressure or density is varied. These experimental results indicate a potential application of the SAW device for liquid sensing, specifically for the detection of liquid flow or level inside the microhole.

REFERENCES

[1] O. Tigli and M. E. Zaghloul, *A novel saw device in cmos: Design, modeling, and fabrication*, IEEE Sensors Journal (2007).

[2] T. Bui, B. Morana, A. Akhnoukh, T. C. Duc, and P. M. Sarro, *Liquid identification by using a micro-electro-mechanical interdigital transducer,* Analyst (2017).

[3] T. Bui, V. Nguyen, S. Vollebregt, B. Morana, H. van Zeijl, T. C. Duc, and P. M. Sarro, *Effect of droplet shrinking on surface acoustic wave response in microfluidic applications,* Applied Surface Science (2017).

[4] L. Y. Yeo and J. R. Friend, *Surface acoustic wave microfluidics,* Annual Review of Fluid Mechanics (2014).

[5] A. Qi, L. Y. Yeo, and J. R. Friend, *Interfacial destabilization and atomization driven by surface acoustic waves,* Physics of Fluids (2008).

[6] L. Y. Yeo and J. R. Friend, *Ultrafast microfluidics using surface acoustic waves,* Biomicrofluidics (2009).

[7] M. Takeshi, S. Mitsunori, and K. Jun, *Measurements of standard-viscosity liquids using shear horizontal surface acoustic wave sensors,* Japanese Journal of Applied Physics (2009).

[8] B. Yildirim, S. U. Senveli, R. W. R. L. Gajasinghe, and O. Tigli, *Surface acoustic wave viscosity sensor with integrated microfluidics on a pcb platform,* IEEE Sensors Journal (2018).

[9] S. U. Senveli, Z. Ao, S. Rawal, R. H. Datar, R. J. Cote, and O. Tigli, *A surface acoustic wave biosensor for interrogation of single tumour cells in microcavities,* Lab on a Chip (2016).

[10] S. U. Senveli and O. Tigli, *Finite element method analysis of surface acoustic wave devices with microcavities for detection of liquids,* Journal of Applied Physics (2013).

[11] J. Wei, P. M. Sarro, and T. C. Duc, *A piezoresistive sensor for pressure monitoring at inkjet nozzle,* 2010 IEEE sensors (2010).

[12] T. Yasui, Y. Inoue, T. Naito, Y. Okamoto, N. Kaji, and M. Tokeshi, *Inkjet injection of dna droplets for microchannel array electrophoresis,* Analytical Chemistry (2012).

[13] T. Bui, A. Tran, B. Morana, J. Wei, T. C. Duc, and P. M. Sarro, *Effect of the interruption of the propagation path on the response of surface acoustic wave transducers,* in *2016 IEEE SENSORS* (2016).

[14] S. U. Senvelia and O. Tigli, *A novel surface acoustic wave sensor with embedded microcavities for size differentiation of solid microparticles,* in *2014 IEEE SENSOR* (2014).

[15] D. Neculoiu, A. Muller, G. Deligeorgis, A. Dinescu, A. Stavrinidis, D. Vasilache, A. M. Cismaru, G. E. Stan, and G. Konstantinidis, *Ain on silicon based surface acoustic wave resonators operating at 5 ghz,* Electronics Letters (2009).

[16] B. C. Wadell, *Transmission Line Design Handbook* (Artech House, 1991).

[17] P. A. Kralchevsky and K. Nagayama, *Particles at fluid interfaces and membranes,* (Elsevier, Amsterdam, 2001) Chap. Capillary Bridges and Capillary-Bridge Forces.

[18] P. Lambert; and J.-B. Valsamis, *Surface tension in microsystems,* (P. Lambert, 2013) Chap. Chapter 2: Axial Capillary Forces.

[19] H. J. Butt and M. Kappl, *Surface and Interfacial Forces* (Willey-VCH, 2010).

[20] M. Zimmerley, C. Y. Lin, D. C. Oertel, J. M. Marsh, J. L. Ward, and E. O. Potma, *Quantitative detection of chemical compounds in human hair with coherent anti-stokes raman scattering microscopy,* Journal of biomedical optics (2009).

[21] M. Bishop, *An introduction to chemistry,* (Chiral Publishing Company, 2009) Chap. Chapter 8: Unit Conversions.

[22] Wikipedia, *Density,* https://en.wikipedia.org/wiki/Density .

6

ENHANCEMENT OF SAW SENSING PERFORMANCE

To further explore the potential of SAW devices operating in liquids, alternative geometries for IDTs are investigated. These proposed new SAW structures are namely focused IDTs (FIDTs) and multiplayer IDTs, specifically optimized for liquid applications. Comparison to the conventional SAW transducer shows that the focused IDT structure has a more concentrated acoustic wave beam at the center of the propagation path. This is determined by the significant loss due to obstacles on the propagation path. Also in this chapter, a mixing IDT structure for SAW devices is presented. It shows the potential for liquid sensing of the SAW device based on the phase shift while conventional devices cannot receive the output signal due to leaky energy of the longitudinal component inside the liquid medium.

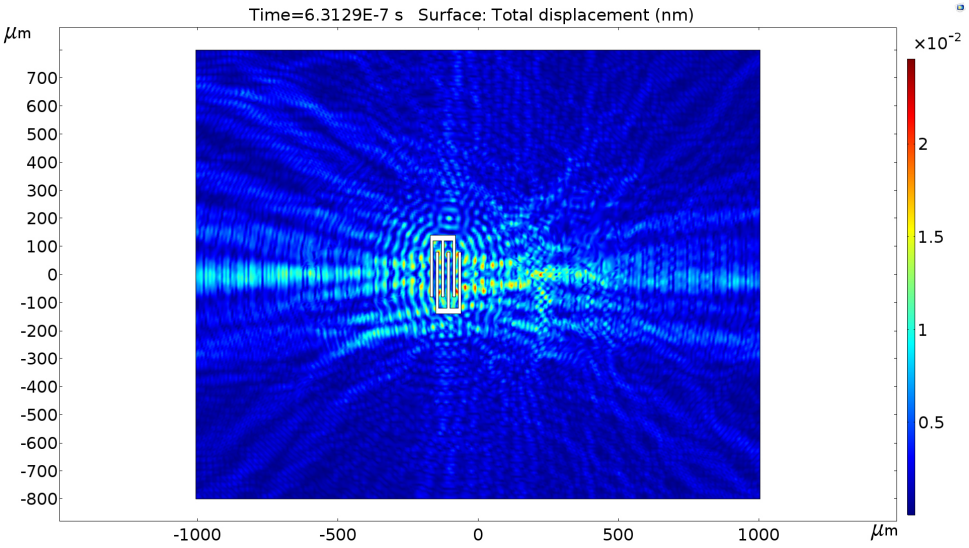

Figure 6.1: Total displacement of the SAW beam generated by three pairs of IDTs.

6.1. INTRODUCTION

As previously mentioned in 2.5.2, the SAW device is a comb structure of IDT fingers placed on a piezoelectric substrate (see Fig 2.15) [1, 2]. Similar to discrete sources, IDTs are utilised to generate mechanical waves propagating on the piezoelectric surface [3, 4]. The structure and position of the IDTs can generate different SAW beams. For the configuration of conventional straight and alternated fingers, the generated SAW beam spreads to the surrounding as shown in Fig 6.1 for the case of 3 IDT pairs. The energy of the conventional SAW device is uniformly diffused [5, 6]. Consequently, it leads to unwanted attenuation in the environment or probable wave interference at the edges. To limit undesired interference and loss, concentrated power is necessary. Hence, new structures of IDTs are explored to produce centralised energy areas [7–10].

Excessive attenuation of the longitudinal component into liquid medium is a problem for the performance of SAW sensors. If the received signal at the output is rather weak or goes to 0, it is impossible to observe the SAW response related to changes in the liquid. Meanwhile, other acoustic waves, like plate mode and shear mode, travel through the liquid medium [11–15]. Therefore, a new configuration needs to be implemented to restrict the wave homogenously spreading on the whole surface and to enhance the sensitivity of SAW devices.

In this chapter, a novel transducer is proposed consisting of FIDTs placed on the piezoelectric material. This configuration is analyzed by the angular spectrum of plane waves [16] and experimentally validated. It compares the perturbation of the SAW beam when there is an absorber, like a layer of photoresist, at the center of the propagation path to that of the SAW beam generated by the conventional IDT SAW device.

Next, to solve the possible leakage of the entire energy of SAWs into a liquid medium, a novel mixing surface acoustic wave (M-SAW) device equipped with multiple IDT layers

is proposed. This aims at generating another acoustic wave which can travel through the liquid medium with or without light attenuation.

6.2. FOCUSED IDT SAW DEVICES

SEVERAL circular, multi-segment structures were discussed and proposed for enhancing the performance of SAW devices [3–7]. The first one was discussed by Kharusi and Farnell [17] in 1972. Afterwards, Green et al. [18, 19] used Huygens's principle to calculate the amplitude field of circular-arc IDTs and proved the existence of the focal points. However calculation and experimental results of Fang and Zhang [20] showed a long and narrow SAW beam in the main propagation path. In 2005, Wu et al. [3] presented the design and analysis of a focused SAW device based on the better method, an angular spectrum of the plane wave theory. The focusing properties of FIDTs, such as having a focal point and a narrow, long and intense SAW beam in the main propagation direction, are suitable for sensors with narrow detecting regions. This avoids energy spreading in unnecessary directions as shown in Fig 6.2. The color bar shows that the measured total displacement of conventional IDT structure is less than that of the focused IDT structure with an arc of 40^0.

6.2.1. ANGULAR SPECTRUM OF PLANE WAVE THEORY FOR FIDT STRUCTURE

THIS section considers the diffraction of a non-leaky surface acoustic wave on the uniform piezoelectric surface. The analysis of the diffraction and orientation is based on the angular spectrum of plane wave method. The $X-Y$ plane is set as a plane of the piezoelectric surface and IDTs are placed along the X axis.

The total surface displacement is represented by the term $\psi(x,y)$, omitting z and t components. In Fig 6.3, k_x, k_y are the x, y components of the wave vector $\vec{k}(\phi)$ which makes an angle ϕ with the X axis. The fingers of the FIDT structure have the same degree of aperture D_a. According to the angular spectrum of plane wave theory [3, 16], for N IDT fingers, the total displacement distribution of the SAW beam at a point (x,y) is given by:

$$\psi(x,y) = \sum_{i=1}^{N} \frac{1}{2\pi} \int_{-\infty}^{\infty} \overline{\psi}(k_y) \exp\{-j[xk_x(k_y) + yk_y]\} dk_y \tag{6.1}$$

where $\overline{\psi}(k_y)$ is the amplitude distribution of the wave components, $x = l, l-d, l-2d, \ldots, l-Nd$ and l is the distance between the first finger and the considered point. There is no loss along the propagation path. For the wave component generated by the i^{th} finger, $\overline{\psi}(k_y)$ is the inverse Fourier transform of the acoustic source function $\psi(x_i', y_i')$ when $x = x_i'$.

$$\overline{\psi}(k_y) = \int_{-\infty}^{\infty} \psi(x_i', y_i') \exp(jy' k_y) dy' \tag{6.2}$$

According to Wu et al. [3], if $\psi(x_i', y_i')$ is a function of the SAW beam generated by the conventional IDT structure, for the circular arc FIDT, it can be written as:

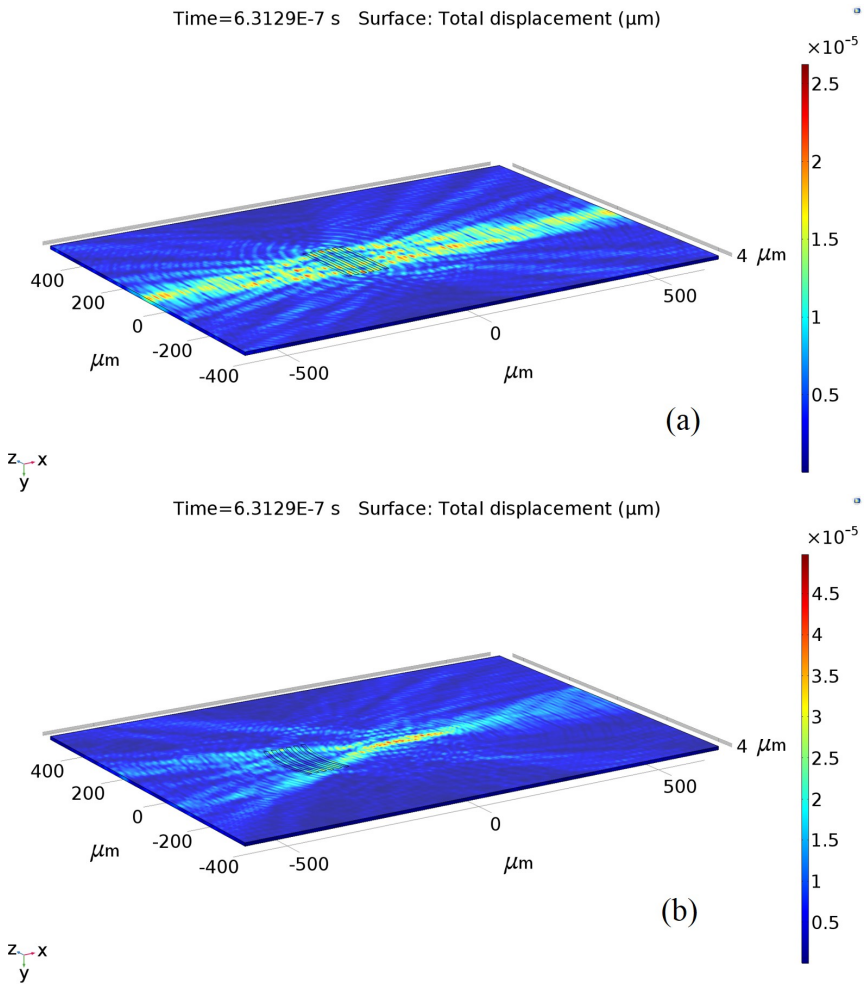

Figure 6.2: Total displacement of (a) conventional SAW device and (b) focused IDT SAW device.

$$\psi'(x'_i, y') = \psi(x'_i, y') \exp(j k_0 \Delta x') \tag{6.3}$$

where $\Delta x'$ is the path difference between the real aperture and the equivalent aperture of the i^{th} input FIDT finger. This parameter $\Delta x'$ depends on the value of arc D_a. Consequently, from Eqs. 6.1, 6.2, and 6.3, the total amplitude of the FIDT structure depends on the number of IDT pairs N, and the arc D_a. The focal length, which is the radius of the first circular arc of the FIDT finger is considered for designing the position of the output FIDT structure.

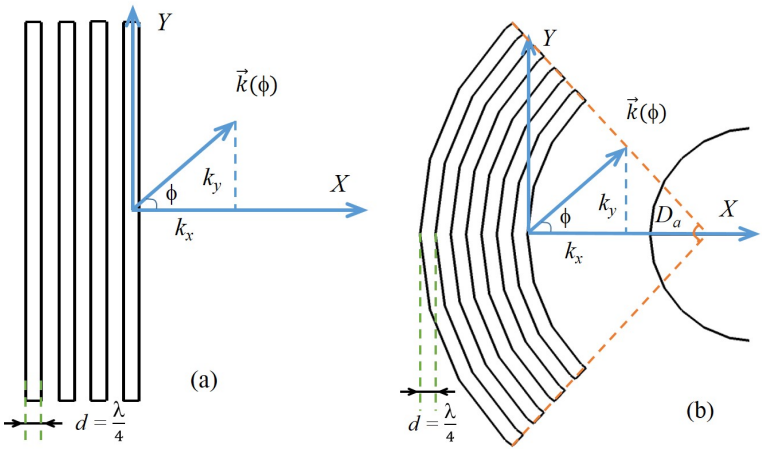

Figure 6.3: (a) Conventional IDTs and (b) FIDTs with circular shape.

6.2.2. ACOUSTIC WAVE PROPAGATION IN FIDT SAW DEVICES BY FEM

THE main design parameters used for FIDT SAW structures with different circular shapes are reported in Table 6.1. The SAW beam is generated by different input pairs of FIDTs and travels through a long path (more than 600 µm). The SAW device includes only input IDT pairs to ignore interference or noise possibly induced by the output IDT pairs. In this way, observation of the SAW beam induced by only input FIDTs becomes clearer.

The design parameters of 1, 2-1, 3 and 4 are listed in Table 6.1 corresponding to the simulated results of Fig 6.4. The results show that when the arc D_a increases, the SAW beam becomes less focused. The focusing property of the FIDT structure reduces faster at a distance larger than the focal length and then the amplitude of the total displacement becomes unstable.

Table 6.1: Design parameters of circular FIDT structures. A conventional IDT structure is included as well for reference.

Design	**Number of pairs** (N)	**Degree of arcs** (D_a)	**Aperture** (A)	**Focal length** (R)
Design 1	3	conventional IDT	200 µm	
Design 2-1	3	40^0	200 µm	292 µm
Design 2-2	5	40^0	200 µm	292 µm
Design 2-3	10	40^0	200 µm	292 µm
Design 2-4	20	40^0	200 µm	292 µm
Design 2-5	50	40^0	200 µm	292 µm
Design 3	3	60^0	200 µm	200 µm
Design 4	3	90^0	200 µm	141 µm

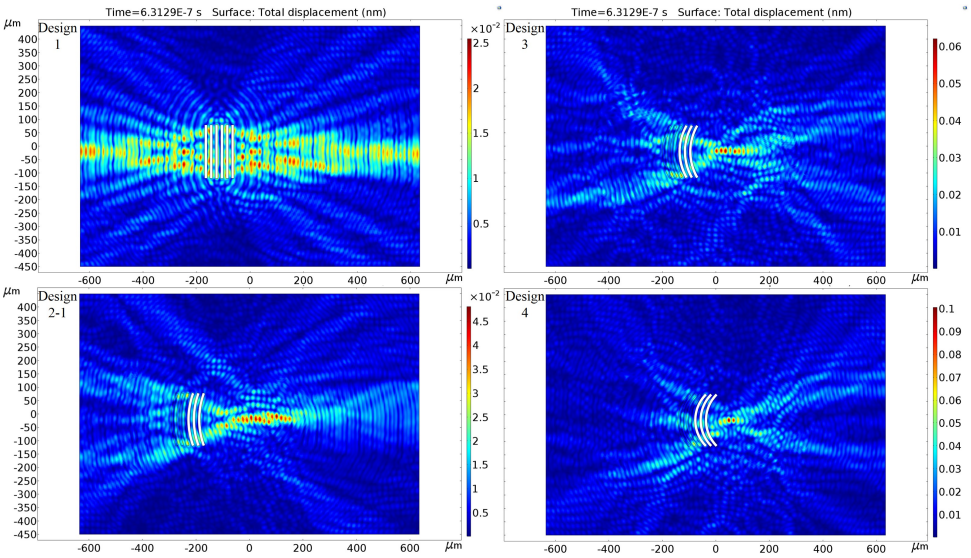

Figure 6.4: Total displacement of the FIDT design with different degree of arc at time t = 0.63 µs.

Let's now consider only the number of IDT pairs for the SAW devices with the 40^0-arc FIDTs with design parameters as given in Table 6.1.When the number of IDT pairs increases, the focusing property of the SAW beam is less obvious but the magnitude of some regions reaches a higher value as shown in Fig 6.5. While the maximum value of the total displacement of the conventional IDT design can only reach 4.2 x 10^{-2} nm, that of the design 2-1, design 2-2 are around 0.055 nm, design 2-3 and design 2-4 are around 0.065 nm and design 2-5 is up to 0.15 nm.

Three positions are considered: at the focal point of the first finger R, before and after the focal point far from the first IDT finger, at $R/2$ and $3R/2$ see Fig 6.6. The electrical potential of three points corresponding to the time of the max total displacement of each FIDT structure is shown in Fig 6.6. The plot colour shows that the potential of the SAW device 1, 2-1, 2-2 and 2-3 reaches the highest value at points close to the focal line. The farther the considered position is, the smaller the value of the potential becomes. From the intersection of these positions, the points having higher potential value stay close to the focal line, therefore, the focusing property of the SAW beam are maintained when the number of IDT pairs increases.

6.2.3. RESULTS AND DISCUSSIONS

BASED on the analysis of the simulation results, SAW devices with the conventional IDT structure and the 40^0-arc FIDT structure (see Fig 6.7) are studied. The SAW device has 50x50 pairs of transmitter and receiver IDT fingers, an IDT aperture of 150 µm and a propagation distance of 200 µm. It also employs Aluminum Nitride (AlN) as the piezoelectric material and Aluminum (Al) for the IDT fingers.

To examine the focusing of the SAW beam, an obstacle is placed in the middle of the propagation path of the SAW device. The focusing energy of the SAW beam travel-

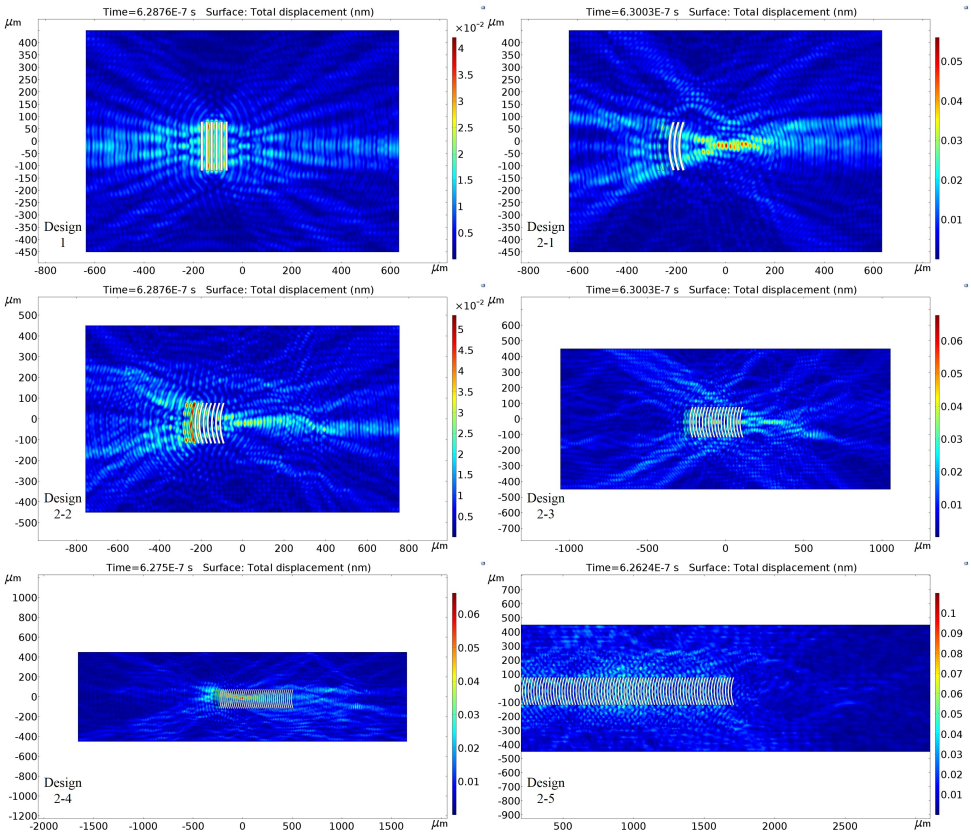

Figure 6.5: Total displacement of FIDT designs and of the conventional IDT design for comparison.

ling through the propagation path can be evaluated by the presence of obstacles. When more energy is lost due to obstacles in the center of the propagation path, the focusing energy increases in the middle. First, a 2.7-µm thickness negative photoresist (NPR) layer is coated on the surface, as shown in Fig 6.9. The diameter of the NPR layer on the propagation path, is 30, 50 or 100 µm, corresponding to 1/5, 1/3 and 2/3 value of the aperture and 3/20, 1/4 and 1/2 value of the propagation path. The presence of the NPR layer in the middle of the propagation path leads to attenuation of the SAW beam as shown in Fig 6.10. This attenuation for the SAW device with 40^0-arc FIDTs is more pronounced than that of the SAW device with the conventional IDTs, especially for the NPR layer of 100-µm in diameter.

Next, this attenuation is validated by embedding a hole with the same size as NPR in the middle of the propagation path. Similarly to the experiment with NPR, the energy of the SAW device with the 40^0-arc FIDTs is attenuated more than three times while that of the SAW device with the attenuation for conventional IDTs is about two times, as shown in Fig 6.11. Due to the strongest concentration for the device with the 40^0-arc FIDTs in the middle of the propagation path, the presence of the bigger hole causes more energy

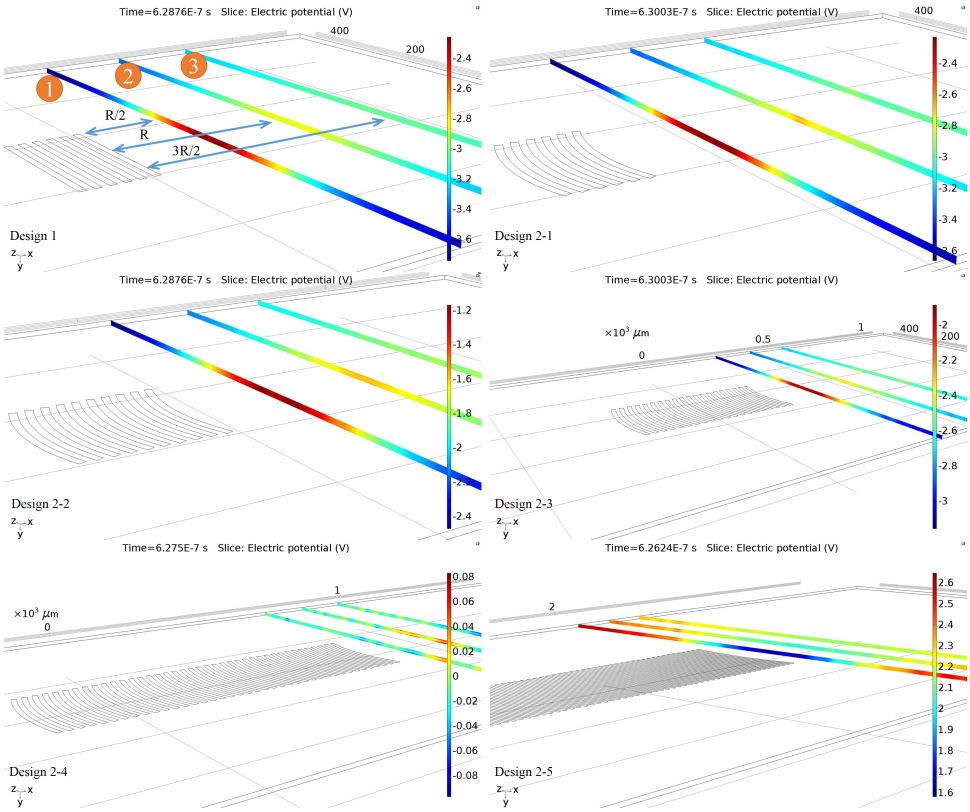

Figure 6.6: Electrical potential of FIDT designs versus the conventional IDT design.

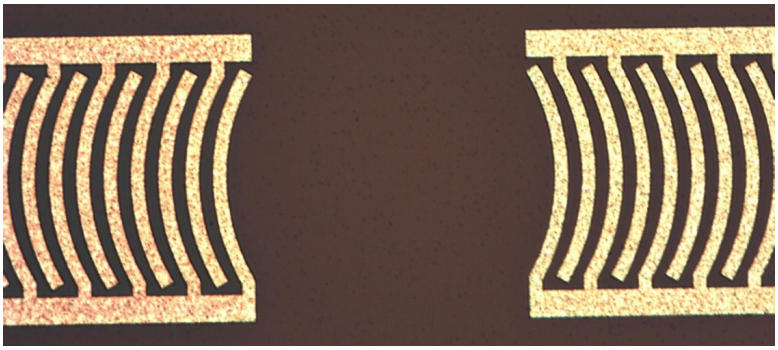

Figure 6.7: Optical image of the SAW device with the 40^0-arc FIDTs.

lost along the propagation path.

The experimental results between the SAW device with the conventional IDTs and the one with 40^0-arc FIDTs show that the SAW beam of the FIDT structure concentrated

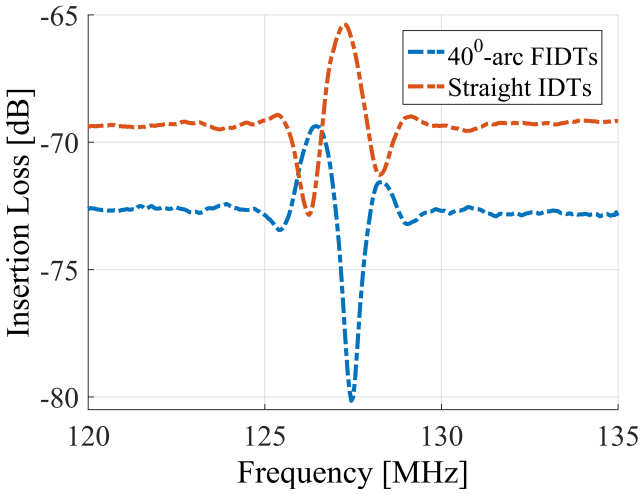

Figure 6.8: Insertion loss of SAW devices with the conventional IDTs and the 40^0-arc FIDTs.

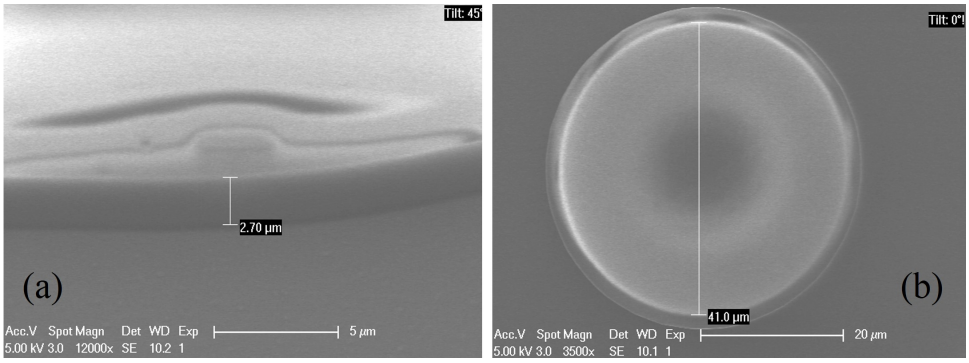

Figure 6.9: SEM images of the 2.7 µm thick photoresist layer, with 41 µm upper diameter positioned at the middle of the propagation path.

in the middle of the propagation path is stronger than that of the conventional IDT structure. Consequently, losses of the FIDT SAW devices due to interruption of the propagation path are larger, which is beneficial for the leakage and streaming phenomenon induced by the SAW beam propagating in a fluid medium, which makes it suited for sensing purposes, actuation and fluidic microtransport.

6.3. MULTIPLE-IDT SAW DEVICE AND LIQUID MEDIUM

As mentioned earlier (see section 2.2), the existence of the longitudinal waves in SAWs causes the leaky phenomenon into a liquid medium placed on the surface of the device [6, 21, 22]. Therefore, SAWs are rarely employed for liquid sensing, because if the liquid covers the whole propagation path, the power is entirely radiated into the liquid

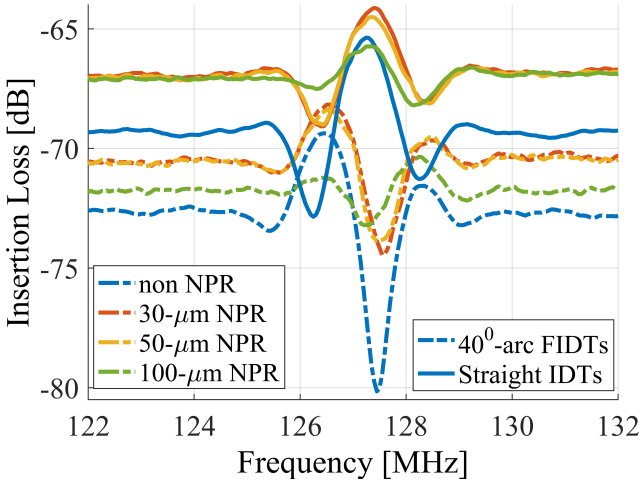

Figure 6.10: Insertion loss for SAW devices with the conventional IDTs and the 40^0-arc FIDTs when a negative photoresist layer (NPR) is placed in the middle of the propagation path.

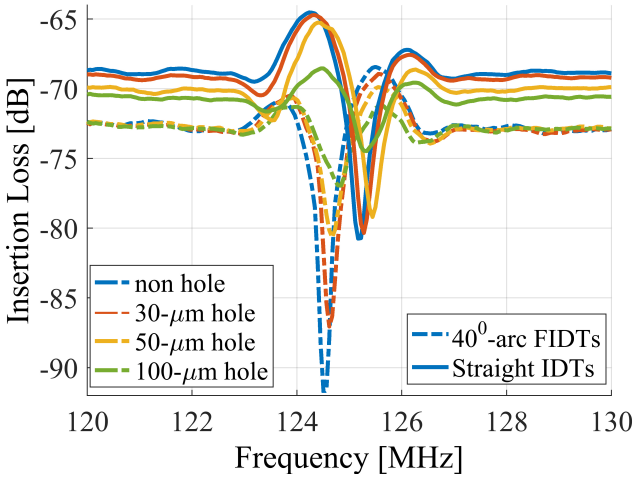

Figure 6.11: Insertion loss of SAW devices with the conventional IDTs and the 40^0-arc FIDTs when a hole is embedded in the middle of the propagation path.

medium and there is no signal at the receiver as also shown in Fig 6.12 when a big droplet is placed and covers the whole propgation path of the conventional SAW device. If there is generated acoustic waves which are capable of traveling through the liquid medium, it is possible to avoid the whole absorption of energy of the SAW device into the liquid medium.

Here, a novel mixing surface acoustic wave (M-SAW) device equipped with multiple IDT layers specifically designed for liquid sensing applications, is introduced. The

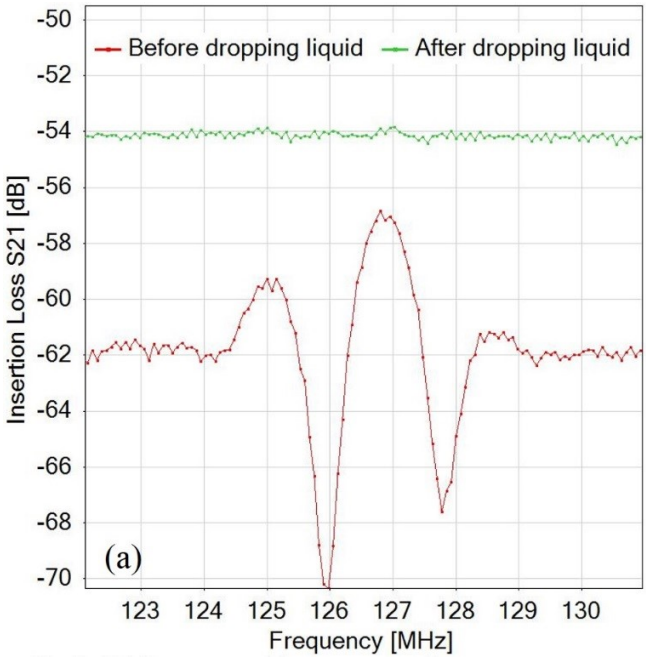

Figure 6.12: Insertion loss of the conventional SAW device in dB before and after dropping liquid.

proposed structures are based on the geometry schematically depicted in Fig 6.13. As each pair of fingers acts as a discrete source, the use of multiple input layers generates more acoustic waves in the piezoelectric medium. By means of theoretical analyses of the fundamental frequency response, we show the role of input-IDT arrays in the mixing acoustic wave (MAW) generation. Finite element analysis (FEA) method is used to model the 3D device and analyze the characteristics of MAWs generated by multiple sources along the wave direction and depth. The design parameters like the crystal cut angle, the thickness of the piezoelectric substrate, the number of finger pairs and the operating frequency are changed to optimize the structure. To evaluate its performance, the M-SAW device is compared to a conventional SAW device with single IDT layer patterned on the top of the piezoelectric layer. This study aims to show which parameter can indeed influence the MAW generation, and how to optimize the structure for liquid sensing applications. To evaluate the performance of the proposed M-SAW configurations, we experimentally measured the variations of single attenuation in the transmission line in the presence of a liquid covering the whole propagation path.

6.3.1. MIXING SAW EXCITATION AND DETECTION

THE proposed device has two input-IDT layers placed in between a thin piezoelectric AlN layer as shown in Fig 6.14. With the second IDT layer placed under the thin film, generated acoustic waves can be either bulk acoustic waves or shear horizontal component of acoustic plate mode waves (SH-APM waves) [23, 24]. The acoustic wave propa-

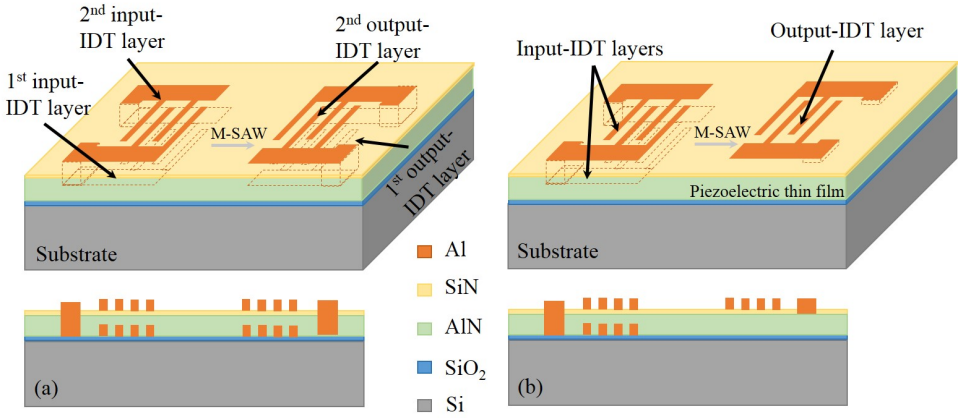

Figure 6.13: 3D sketch and schematic cross-view of the novel M-SAW structures including two IDT layers: (a) only at the input side and (b) at the both sides.

gates, covering a distance $\frac{h}{\cos(\beta)}$ of the plate at cut angle β to the surface as indicated in Fig 6.14. The angle value depends on the piezoelectric crystal cut. Rayleigh-SAWs from the first input-IDT layer travel on the piezoelectric material surface. They are mixed together and create MAWs which reduce the longitudinal waves of SAWs. Like shear horizontal wave devices [22, 24, 25], the generated MAWs, unlike the longitudinal waves, can propagate into solid-liquid interface.

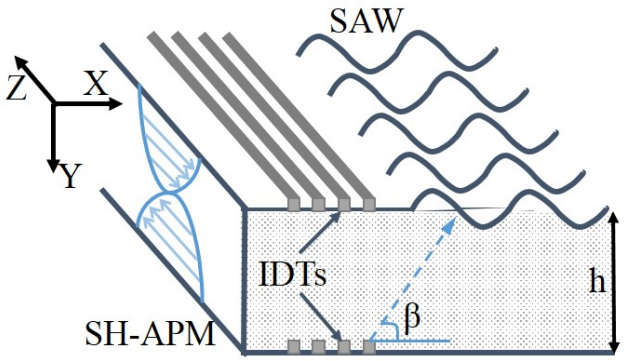

Figure 6.14: SAW and SH-APM waves generated by two input-IDT layers.

The IDT structure has uniform single-electrode transducers. Each m^{th} IDT finger pair is a discrete source exciting odd harmonics at synchronous frequency $f_m = mf_0$ [26]. The mechanical waves excited by the two sources at the top and bottom of the piezoelectric substrate have opposite-phase (see Fig 6.15). The transducer response $H_c(\omega)$ of the conventional SAW device is described as [16]:

$$H_c(\omega) = -jE(\omega)A(\omega)\sqrt{\omega W\varepsilon_\infty/(\Delta v/v)} = -j\overline{\rho}_k(k)A(\omega)\sqrt{\omega W(\Delta v/v)/\varepsilon_\infty} \tag{6.4}$$

Here, $\Delta v/v$ is the fractional difference between wave velocities for a free surface and a metallized surface, and $A(\omega)$ is the fractional difference between wave velocities at the free surface and at the metallized surface. ω, W, v and ε_∞ are the angle frequency, the aperture, the phase velocity and the effective permittivity at infinite wavenumber, respectively. The electrostatic charge density $\overline{\rho}_k(k)$ depends on the structure and position of the electrode transducer as shown in Fig 6.15. The transducer response $H(\omega)$ of the M-SAW device is given by:

$$H(\omega) = H_n^{'}(\omega) + H_c(\omega) = j\overline{\rho_k^{'}}(k)A(\omega)\sqrt{\frac{\omega W(\frac{\Delta v}{v})}{\varepsilon_\infty}} \times \exp(-\frac{\alpha\omega x_3}{v_p}) - j\overline{\rho_k}(k)A(\omega)\sqrt{\frac{\omega W(\frac{\Delta v}{v})}{\varepsilon_\infty}} \tag{6.5}$$

Here, $x_3 = \frac{h}{\cos\beta}$ is the propagation distance of the acoustic waves generated by the second IDT layer (see Fig 6.14), while ω, v_p are the attenuation coefficient and the plate velocity, respectively.

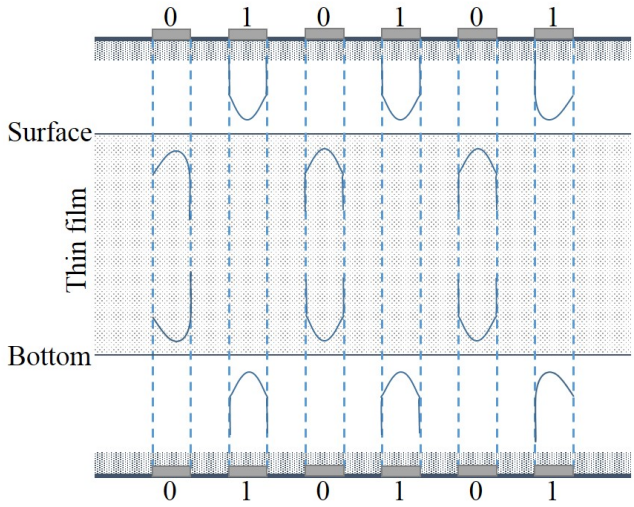

Figure 6.15: Electrostatic charge densities induced by the top and bottom IDTs of the M-SAW device are opposite in phase.

For the conventional SAW structure, as $E(\omega)$ is assumed constant, the shape of the transducer response in magnitude is given approximately as $sinc(X)$ [26]. For the M-SAW device, as $E(\omega)$ is a function of the electrostatic charge density (Fig 6.15), the form of the transducer response is approximated by:

$$|H(\omega)| \sim N\frac{\sin(X)}{X} + N\sin(X)[-m\frac{|\overline{\rho_k^{'}}(k)|}{X|\overline{\rho_k}(k)|}\exp(-\alpha\omega\frac{h}{v_p\cos\beta}) + 1] \tag{6.6}$$

Here, $N = M/2$ is the number of the IDT pairs and , with being the center frequency of the fundamental response. The approximated form of the transducer response in Eq. 6.6 shows that the generated acoustic waves on the surface include the original SAWs and MAWs which are superposed. So, due to the presence of longitudinal waves of the original SAWs, the leaky phenomenon still happens at the contact with the liquid, and as MAWs act like shear horizontal waves which can travel though the liquid medium, an oscillation of the output signal is still measured [27]. In fact, before dropping the liquid, the reflection coefficient S_{21} in two-port scattering matrix S consists of the superposition of the original SAW component, $sinc(X)$, and the MAWs component, the mostly uniform harmonic beams. The disappearance and appearance again of the term $sinc(X)$ before and after the liquid vaporization process is a good proof of the presence of longitudinal waves of the original SAWs. In the next section, the effect of the parameters in Eq. 6.6, such as the thickness h, the center frequency f_0, the cut angle β, and the number of the IDT pairs N, on longitudinal waves of SAWs is investigated and the mechanical acoustic waves on the surface are compared to those of the conventional devices.

6.3.2. FINITE ELEMENT ANALYSIS OF 3D MIXING SURFACE ACOUSTIC WAVE DEVICE

To observe the Rayleigh-SAW phenomenon excited by multiple sources, SAW devices are modeled and computed in 3D geometry in time domain. To investigate longitudinal waves along the propagation direction, we varied the AlN thickness, the operating frequency, the cut profile of the piezoelectric layer and the number of IDT pairs. The simulated M-SAW structures consist of metallic IDT layers (Al) placed on the top and bottom of the piezoelectric substrate (AlN). In this way, the piezoelectric effect used as the piezoelectric Multiphysics interface is a coupling between piezoelectric properties in solid mechanics and electrostatics instead of the single physical module. This simulation aims at the examination of which design parameters upgrade or degrade the mechanical waves of the M-SAW devices when Rayleigh damping is assumed for the top and bottom of the piezoelectric substrate compared to the conventional SAW device.

The same voltage sine (10 V) is applied to the even fingers of both input-IDT layers while the odd ones and those of the output IDTs are connected to ground. The formation of odd different-phase harmonics with synchronous frequencies at odd IDTs of both layers are mixed and propagate through the piezoelectric surface. The piezoelectric material, wave velocity and operating frequency are parameterized. To minimize the wave-reflection phenomenon, the substrate is much larger than the IDT modeling geometry and the low-reflecting boundary condition is assigned for all edges of the piezoelectric substrate.

Fig 6.16a shows the vibration of the longitudinal components along the wave direction X of the M-IDT device is slightly stronger than that of conventional ones. The original acoustic waves are generated by both IDT layers and superposed with mixing acoustic waves on the surface, as proved by the kinetic energy investigation on the piezoelectric surface shown in Fig 6.16b. Larger kinetic energy of the multiple IDT layer devices is measured at the central point of the propagation path, because of the presence of the mixing waves. A sequential analysis technique in the cumulative sum method [28, 29] is used to observe the stability rate of acoustic waves after they are superposed to orig-

inal acoustic waves and mixed. Fig 6.17a shows that the generated mechanical waves based on the stability rate of both novel structures are quite similar and faster than that of conventional ones. However, the output voltage of the M-SAW device (see Fig 6.17b) with two input-IDT layers is larger. The reason is that the energy of the two IDT-layer device is distributed on the two output IDT layers. Therefore, the M-SAW device with two input-IDT layers has the most effective performance.

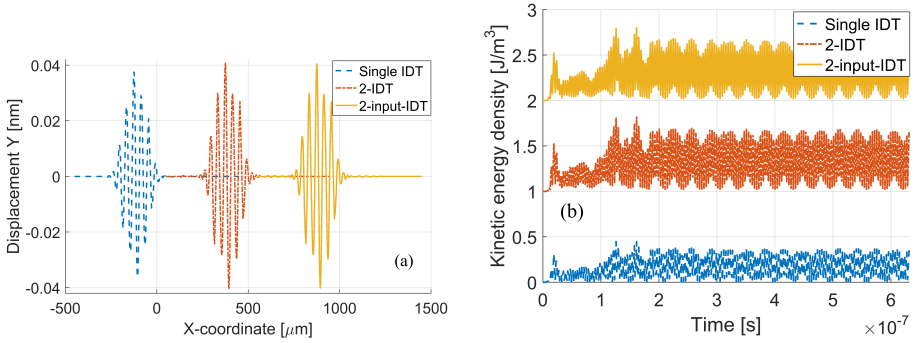

Figure 6.16: (a) Longitudinal displacement Y along the wave direction X at time $t = 10$ ns corresponding to the 3 structures studied (500 µm offset in X axis has been added to separate signals) and (b) kinetic energy density measured at the centre point on the surface (1 J/m^3 offset in Y axis has been added to separate signals).

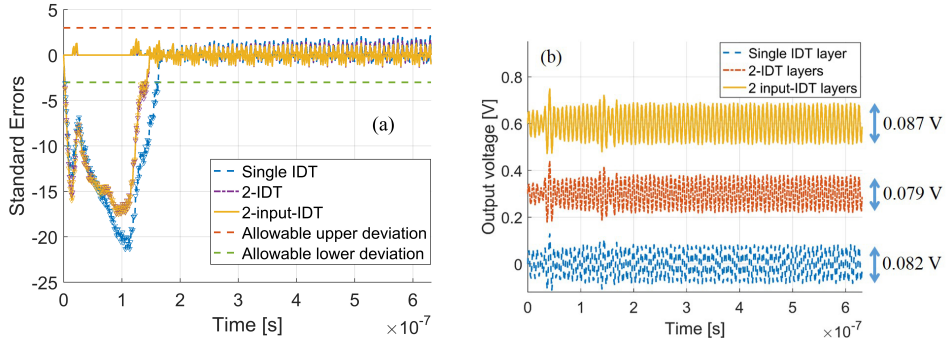

Figure 6.17: (a) The unstable vibration detection of the mechanical waves using the cumulative sum method [28, 29] and (b) output voltages of the novel M-SAW devices and the conventional SAW device (0.3 V offset in Y axis has been added to separate the signals).

Next, simulation results of the M-SAW device with two input-IDT layers, compared to the conventional device, are reported to show how configuration parameters in Eq. 6.6 affect the generated waves on the surface, especially the longitudinal waves along the propagation direction, which is responsible for the leakage inside the liquid medium.

A. THE THICKNESS OF THE PIEZOELECTRIC LAYER

As surface acoustic waves cannot propagate much beyond twice the wavelength, the examined piezoelectric thicknesses are 0.2λ, 0.25λ, 0.5λ, λ and 2λ, where λ is the

piezoelectric wavelength. Fig 6.18 shows how the variation in thickness of the thin film influences wave generation along the propagation path. The intensity of the shear horizontal waves from the second IDT layer traveling through the plate to the surface depends on the piezoelectric thickness. So, when the substrate is thinner, a larger excitation for the longitudinal waves of the novel M-SAW device along the wave direction is observed as illustrated in 6.18a. In all cases, these waves are always excited more than for the case of the conventional device. The kinetic energy investigation shows that generated mechanical waves on the surface are stronger (1.5 - 2.8 times), than that of the conventional ones (see Fig 6.18b), the highest increase is observed for a thickness of 0.5λ.

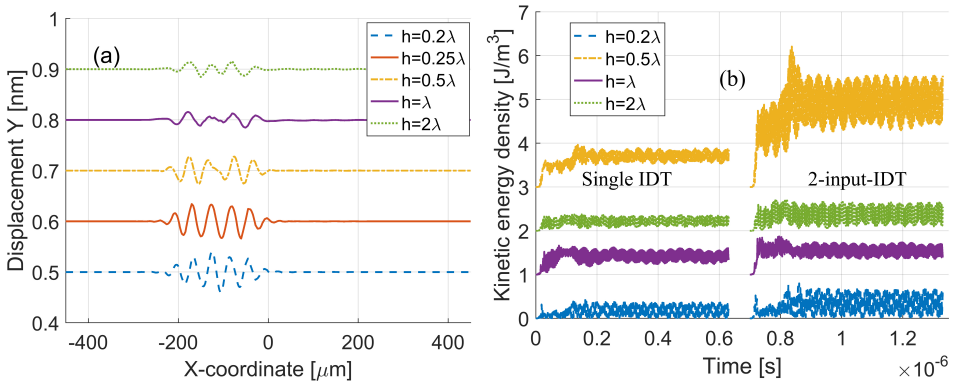

Figure 6.18: (a) Displacement Y of the mechanical waves along the wave direction X at time t = 10 ns corresponding to different substrate thickness h cases (0.1 nm offset in the Y axis has been added to separate the graphs); (b) kinetic energy density measured at the center point on the surface (1 J/m^3 offset in the Y axis and 700 µs offset in the X axis have been added to separate the graphs).

B. THE NUMBER OF FINGER PAIRS N

Incrementing the number of IDT pairs excites more odd harmonics at odd multiples of the synchronous frequency [26] (see Fig 6.19a). A large number of IDT pairs achieves not only a narrow bandwidth [16, 26], but also more odd harmonics of the frequency $f_m = mf_1$ at the odd fingers m^{th} of both IDT layers. For the M-SAW device, the second IDT layer induces partition in the longitudinal wave beam when the number of the finger pairs is incremented. But the maximum amplitude of the longitudinal waves does not change much. However, the investigation in energy shows that their kinetic energy is rather strong, especially at IDT pairs $N = 5$ and always larger than that of the conventional devices (see Fig 6.19b). In other words, generated mechanical acoustic waves on the surface are stronger, due to the intensity of mixing acoustic waves on the surface

C. THE OPERATING FREQUENCY f_0

The operating frequency f_0 is given by $f_0 = \frac{v}{\lambda} = \frac{v}{4d}$, where v, λ and d are the material velocity, the wavelength and the finger width, respectively. So, the operating frequency f_0 depends on the finger width d. The magnitude of the longitudinal waves along the wave direction of the novel device is stronger with increasing operating frequency and always better than that of the conventional ones (see Fig 6.20a). This is also observed in the

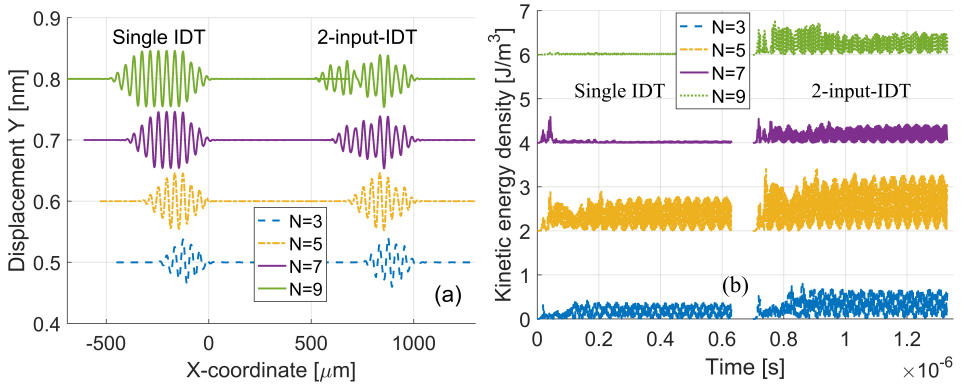

Figure 6.19: (a) Displacement of the mechanical waves along the wave direction X at time t = 10 ns corresponding to different number values of IDT pairs. (1000 µm offset in the X axis and 0.1 nm offset in the Y axis among the lines have been added), (b) kinetic energy density measured at the center point on the surface (2 J/m^3 offset in the Y axis and 700 µs offset in the X axis have been added to separate the graphs).

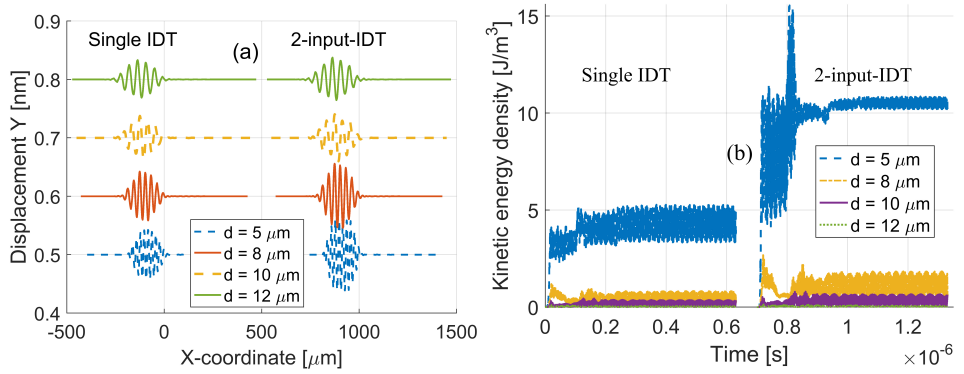

Figure 6.20: (a) Longitudinal displacement Y along the wave direction X of the novel and conventional structure corresponding to different values of $d = \lambda/4$ (1000 µm offset in the X axis and 0.1 nm offset in the Y axis among the lines have been added), (b) kinetic energy density measured at the center point on the surface (700 µs offset in the X axis among the lines has been added).

intensity of the kinetic energy as shown in Fig 6.20b. The kinetic energy of the acoustic waves varies dramatically at the operating frequency f_0 = 253 MHz, corresponding to d = 5 µm. Although its intensity is much higher than for the single IDT device, it has a smaller amplitude of the harmonic oscillation after 0.2 µs.

D. THE CUT PROFILE OF THE PIEZOELECTRIC LAYER β

The cut profile of the AlN crystal is investigated because it affects the generation of SAW and plate acoustic wave of SH-APM mode on the surface [23, 24]. Fig 6.21 shows that the wave displacement field along thickness at angle $\beta = 0^0$ changes the wave direction. The fluctuation magnitude of the longitudinal component along the propagation path is excited more when the angle β in Euler system is -90^0 (see Fig 6.22a). However, at 90^0,

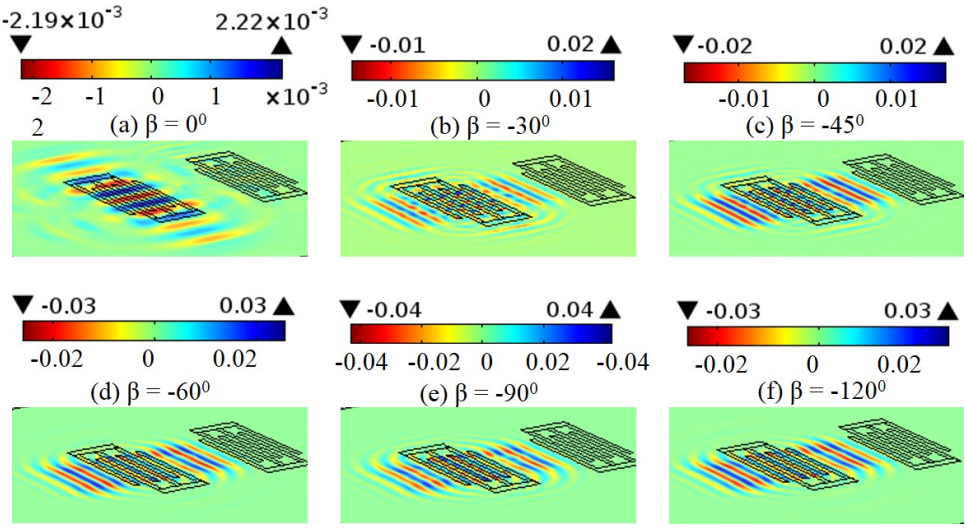

Figure 6.21: Simulation results showing the displacement field along the piezoelectric thickness of the two input-IDT layers corresponding to different values of the angle β.

6

the kinetic energy is smaller than for the other cut profiles. This means that the other components are weaker, thus the oscillation of the acoustic wave at the central point is weaker.

In conclusion, the simulation results show that the response of the M-SAW device is more significantly excited than the conventional device when the number of IDT pairs, the operating frequency, the cut profile and the substrate thickness are modified. The substrate thickness affects the formation of the longitudinal component. More acoustic waves are generated by the second IDT layer when the thickness is less than a half of the wavelength. Incrementing the value of finger pairs only influences the partition in the longitudinal wave beam and does not have any effect on the steady status of the device operation. With a higher center frequency, the magnitude of the longitudinal waves and the steady state are better. It is possible to achieve the most longitudinal wave along the propagation path when the Euler angle in the rotated coordinate system is 90^0.

6.3.3. DESIGN AND FABRICATION OF MULTI-SOURCE MSAW DEVICES

IN the previous section, the simulation results show the effect of the second IDT layer on the longitudinal component along the wave direction compared to the conventional device. Based on these results, the design of the novel M-SAW structures is optimized. The proposed devices have a large area of 4800 µm x 2500 µm, small wavelength (40 µm) and long delay line (1000 µm). The sensor includes two sets of Aluminum IDTs (40 x 40 finger pairs) patterned on the top and the bottom of the thin AlN film. The aim of the long aperture here is to avoid diffraction and Ohmic losses. The other layer dimensions and additional parameters of the M-SAW device can be found in Table 6.2.

To evaluate the performance of the novel M-SAW devices, we compare it to the conventional SAW device with the same design parameters such as the number of IDT fin-

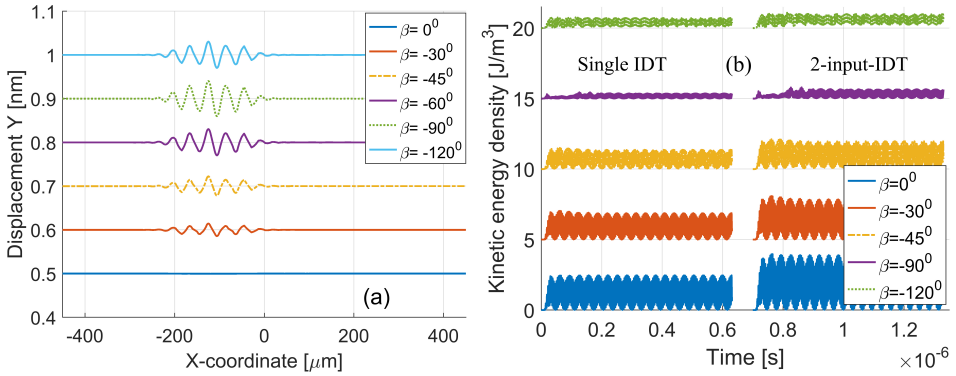

Figure 6.22: (a) Displacement of the mechanical waves along the wave direction X at time t = 10 ns corresponding to different angles in Euler system (0.1 nm offset in the Y axis among the lines has been added). (b) Kinetic energy density measured at the center point on the surface (5 J/m^3 offset in the Y axis and 700 μs offset in the X axis have been added to separate the graphs).

Table 6.2: The design parameters of the M-SAW devices.

Parameters	**Value**	**Unit**
IDT finger width $d = \lambda/4$	10	μm
1st and 2nd IDT finger height	800	nm
Aperture	2000	μm
Number of the input and output fingers	40x40	
The expected center frequency f_0	125	MHz
The propagation path	1000	μm
Thickness of the thin film AlN h	1	μm
Sublayer SiN	100	nm
Sublayer SiO_2	150	nm

ger pairs, the operating frequency, the substrate size and sublayers like SiO_2 and SiN as shown in Fig 6.23.

Fig 6.24 schematically shows the fabrication process of the devices. To obtain fine patterning of the IDT layers and of the thin AlN film, an IC-compatible fabrication process is used for the device fabrication. Main steps are reactive sputtering, inductively coupled plasma (ICP) dry etching technique and optical lithography. The sputtering technology aims at providing good adherence of the layers to the substrate, highly uniform composition and contamination reduction. Thin, low-stress SiO_2 interlayers are deposited to balance the tensile strength of the sputtered AlN thin film and improve the AlN piezoelectric quality [30]. The thin film of SiN is used to protect AlN during the metal etching process.

For precise fine patterning of the Al contact and the IDTs, ICP dry etching was preferred. After each dry etching step, the IDT fingers are wet etched to avoid any non-

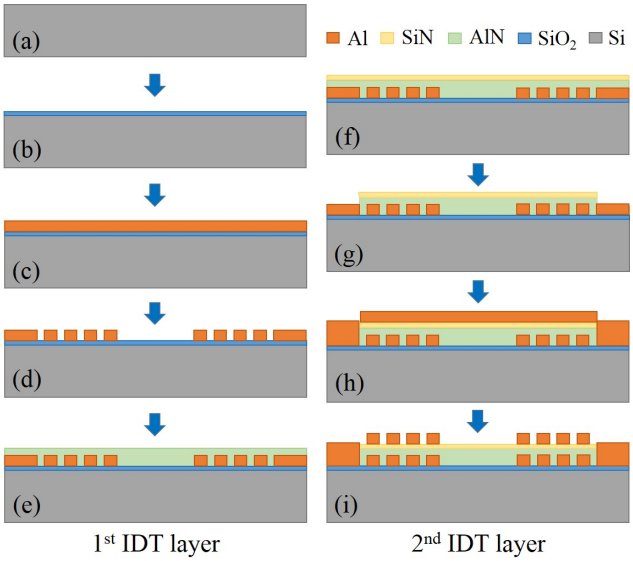

Figure 6.23: Investigated SAW structures: the conventional SAW structure (a), and the novel M-SAW structure with (b) two input and output IDT layers and (c) two input-IDT layers.

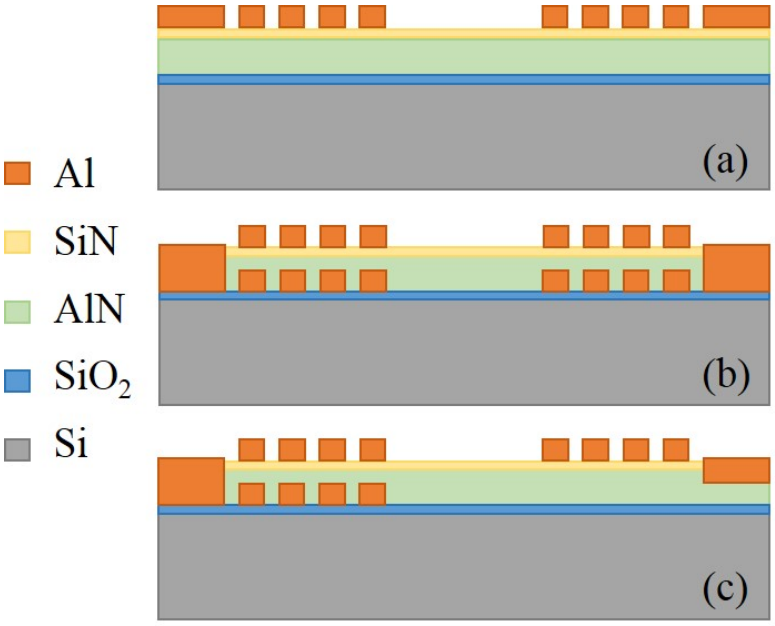

Figure 6.24: Main steps of the fabrication flow of M-SAW device with multiple IDT layers: (a)-(e) for the first IDT layer and (f)-(i) for the second IDT layer.

volatile and sidewall residues which lead to short-circuit and smooth out the side wall profile of the metal lines. Before depositing the second IDT layer, the AlN thin film and the protecting SiN layer are etched to open the contact between both IDT layers. SEM images of the fabricated device are shown in Fig 6.25. They show a representative anisotropic profile of multiple IDT layers and smooth sputtered AlN thin film.

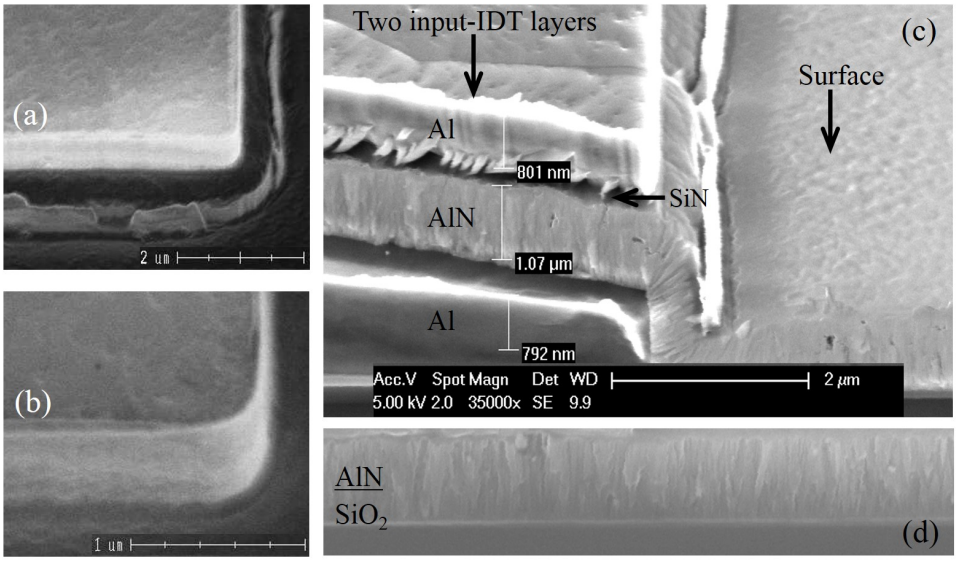

Figure 6.25: SEM image of the two input-IDT SAW device: Top-view of (a) input finger, (b) output finger, (c) cross-view of the input fingers and piezo surface and (d) AlN growth on the thin film SiO_2.

6.3.4. SYSTEM CONFIGURATION

THE measurement system (see Fig 6.26a) consists of an Agilent 8753E network analyzer connected to a manual RF probe station. These probes are controlled by micro-positioners stabilized on an air table. Chip pads are designed for waveguide infinity probe ground-signal-ground (GSG) to reduce stray EM fields near probe tip and improve crosstalk performance between tips. The highest power 5 dBm is applied at the two pads connecting to the input-IDT layers. The number of the sweeping points for each measurement time in the frequency range from 115 to 135 MHz, is 200. Therefore, the equipment delay is approximated to 5 seconds.

Liquid as the leaky medium is used to examine the existence and nature of the longitudinal and mixing waves. Here, we report on the investigation of the response of the M-SAW devices when a small amount of deionized water (0.05 – 0.13 µl) is dropped on the transmission line as shown in Fig 6.26b. To examine the sensitivity of this device, we performed experiment with deionized-water because an acceptable vaporization rate for the measurement equipment delay and very small amount of stagnant liquid molecules after vaporization process are expected. We drop different volumes of deionized water on the propagation path of the M-SAW devices with a high-precision manual pipette

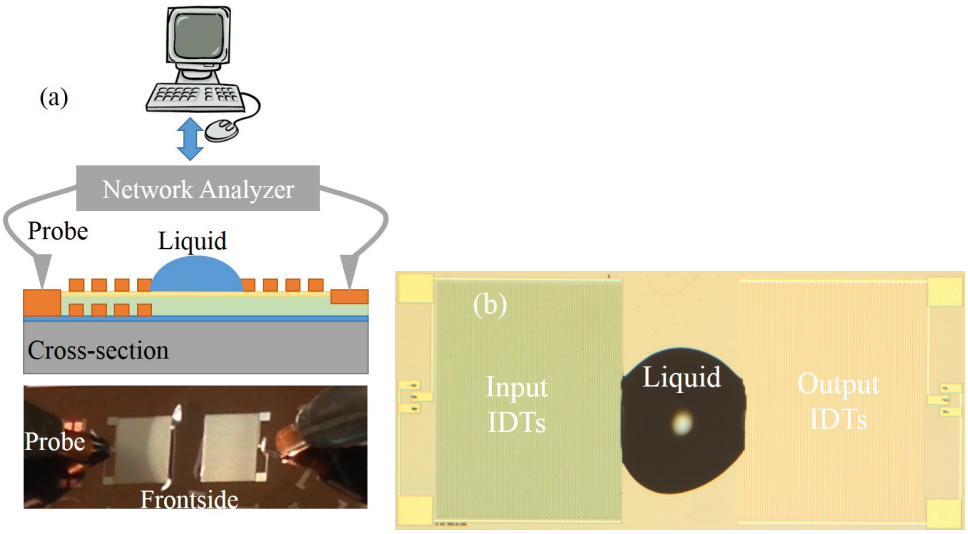

Figure 6.26: (a) A schematic cross section and frontside of the M-SAW device in the measurement system and (b) microscope image of the M-SAW device with two input-IDT layers and the droplet on the propagation path.

(Rainin Classic Pipette PR-2). The device response is measured continuously until the liquid vaporization process terminates.

6.3.5. RESULTS AND DISCUSSIONS

FIRST, the behavior of the M-SAW device is studied when a droplet is placed on the entire propagation path. The response of the multiple input-IDT SAW device corresponding to the evaporation duration of the droplet has been examined. Due to the leakage phenomenon of the Rayleigh-SAW component into liquid medium, the term $sinc(X)$ of the conventional device in the transducer response equation is ignored as shown in Fig 6.27. This phenomenon happens until DW is vaporized completely on the piezoelectric surface (Fig 6.28a). Experimental phase shift of -16.35^0, -11.23^0, -4.84^0, and -0.86^0 are obtained for different volumes of demi-water after 10 seconds, 2, 4 and 5 minutes of vaporization, respectively, as shown in Fig 6.28b.

A droplet, like liquid medium, is placed in the different positions of the propagation path as shown in Fig 6.29.

The generated M-SAWs are superposition of a component similar to the single-layer transducer response termed as $sinc(X)$ and of MAWs formed as a uniform harmonic beams as described in section 6.2. This also shows in the magnitude of the insertion loss reported in Fig 6.29. To examine the sensitivity of the MAW component when it contacts the liquid medium, we investigated the response change during the entire deionized water vaporization process. Because of the leakage phenomenon of the longitudinal component in M-SAWs into liquid medium, the term $sinc(X)$ of the conventional SAW device in the transducer response form disappears. During the vaporization process, only most MAWs can exist and travel through the liquid medium.

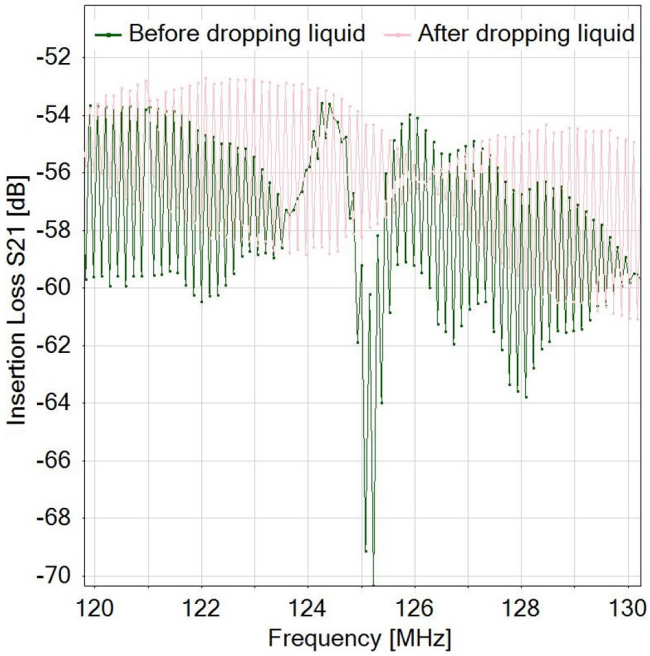

Figure 6.27: Insertion loss of multiple input-IDT SAW device in dB before and after dropping liquid.

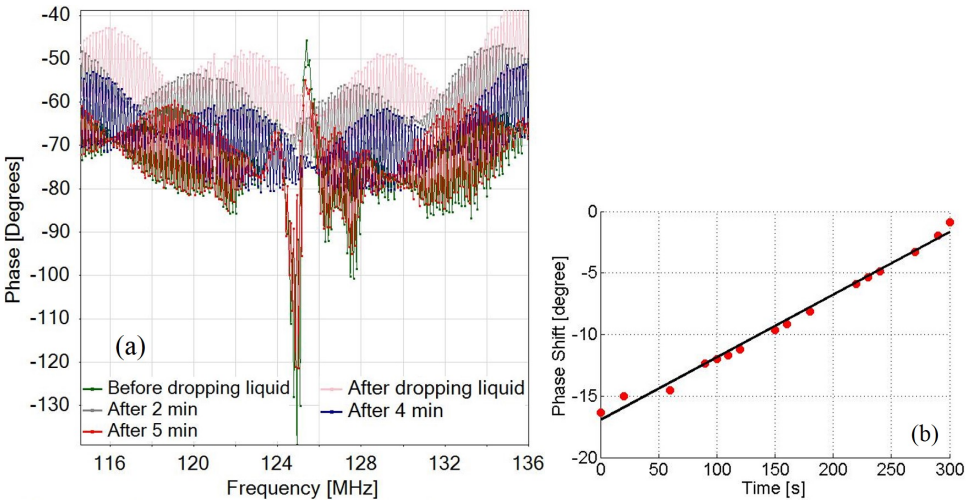

Figure 6.28: (a) Phase attenuation and (b) phase shift of the multiple input-IDT SAW device during the liquid evaporation process.

We also observed an effect of the position of the smaller droplets on the wave propagation path as illustrated in Fig 6.29where the attenuation of the M-SAW device with two input-IDT layers in phase is shown. The M-SAW response is most strongly influenced

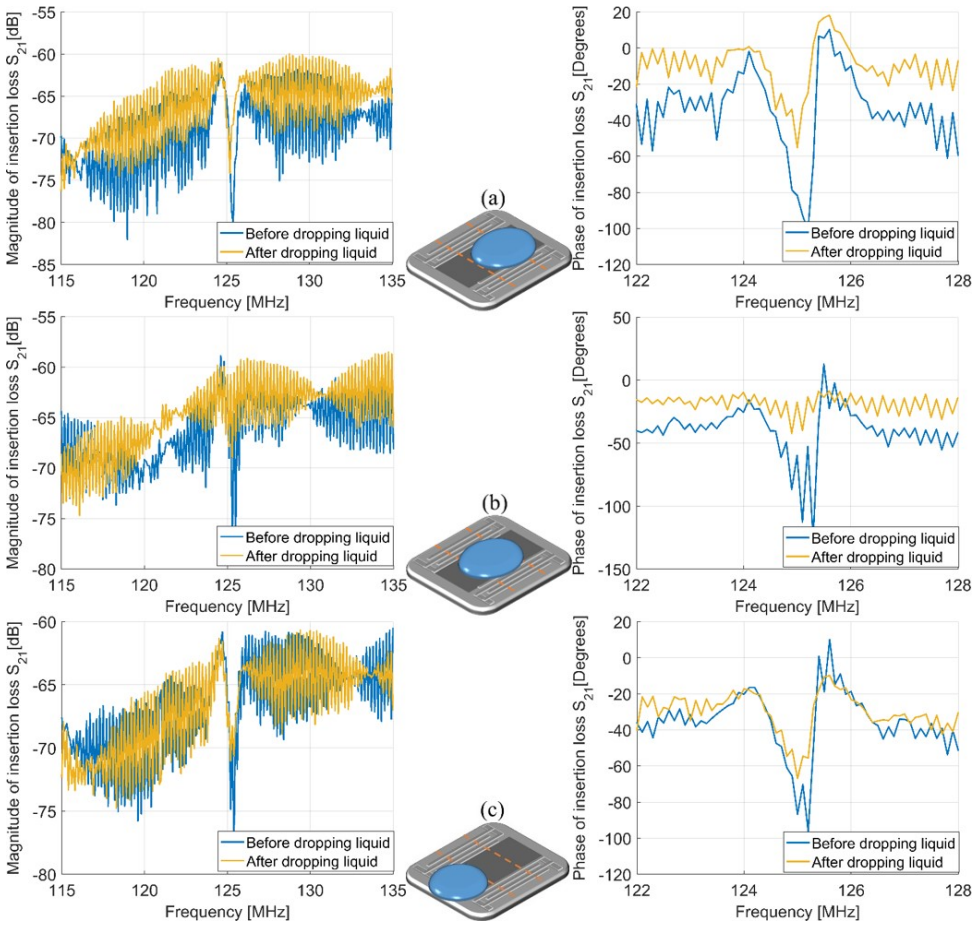

Figure 6.29: The magnitude and the phase of the insertion loss of the M-SAW device with two input-IDT layers are measured before and after dropping the liquid when deionized water is dropped in the different positions of the propagation path such as (a) one half propagation area at the top, (b) one half propagation area of the middle and (c) one third propagation area at the bottom.

and stably modified when the droplet is placed in the middle of the propagation path. Also, for the same liquid volume, but dropped in the middle, the stable status occurs faster, indicating that the energy of MAWs focuses mostly in the middle of the propagation path. The difference between the phases of the insertion loss S_{21} before and after dropping the liquid is continuously recorded. In Fig 6.30, we see the phase shift increases linearly during the liquid vaporization process before achieving saturation. If the same volume of liquid covers less area, the phase shift is small and quickly reaches stability.

We studied the device response for different volumes of liquid as illustrated in Fig 6.31 and Fig 6.32. They show that the slope of the curve of the phase shift increases with the liquid volume. As the duration for the liquid vaporization process of the bigger droplet is longer, the duration of the phase shift to reach stability is also longer. When

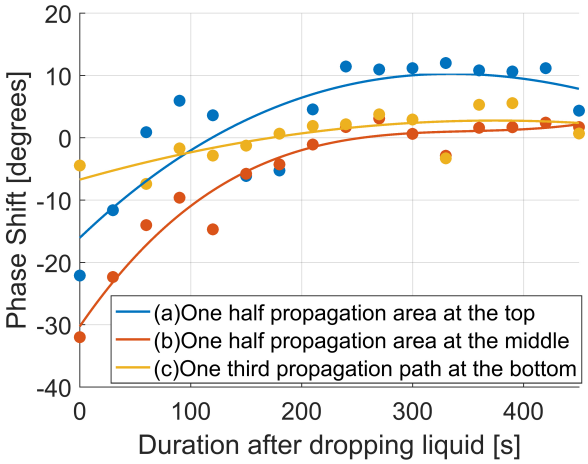

Figure 6.30: Phase shift of the M-SAW device during the vaporization process.

the volume of the vaporized bigger droplet equals the volume of the smaller droplet, its phase shift is similar to that of the smaller one.

The sensitivity of a liquid sensor is defined by the ratio of the output change to the change of the liquid volume. It depends on liquid volume, duration for the whole liquid vaporization process and response of the measurement system such as the pipette accuracy and the resolution of network analyzer. Therefore, it can be measured as ratio of the average change speed of the phase shift to the liquid vaporization rate as shown in Table 6.3. This rate is considered from the time when the liquid is dropped on the piezoelectric surface to the time the liquid vaporizes completely.

Table 6.3: The sensitivity of the M-SAW device.

Type	**Liquid volume (µl)**	**Vaporization time (s)**			**Sensitivity (degrees/µl)**		
		1^{st}	2^{nd}	3^{rd}	1^{st}	2^{nd}	3^{rd}
two input-IDT layers	0.05	180	210		46.0	177	
	0.1	270	270	270	98.8	103.0	134.2
	0.13	270	330	360	59.6	47.3	55.1
two IDT layers	0.1	150	210	180	67.9	26.0	53.9
	0.13	390	390	330	67.9	67.0	58.7

The resolution, called a threshold sensitivity, is defined as the lowest change of the input, like smallest liquid volume, which gives a measurable change of the sensor output. From these data, we see that 0.03 µl is the smallest change of the liquid volume that causes distinguishable phase shift duration. The full range of a sensor refers to the value range which can measure. It depends on the aperture size of the IDT fingers, the propagation area and in case no confinement for the liquid is present, overflow of liquid on

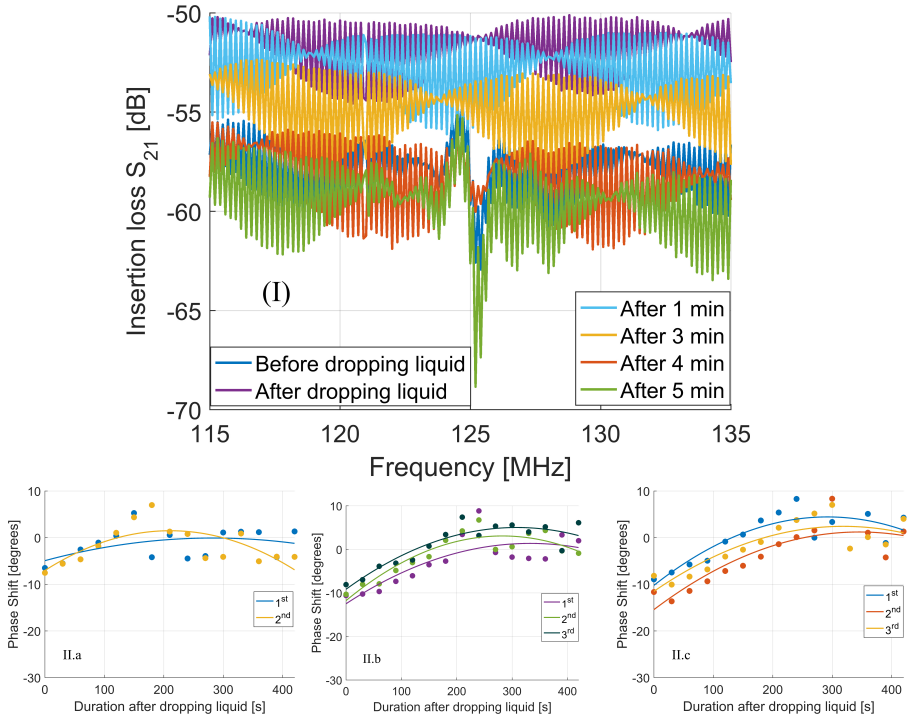

Figure 6.31: (I) The magnitude of the insertion loss of the M-SAW device with two input- IDT layers in dB during the first-stage vaporization of the liquid for a 0.1 µl volume and (II) phase shift when the droplet (a) 0.05 µl, (b) less than 0.1 µl and (c) 0.13 µl is dropped in the middle of the propagation path.

the electrodes should be prevented. For the current design, this range is 0.05 – 0.13 µl.

6.4. CONCLUSION

THE simulation and experimental results show that the FIDT structure generates the stronger SAW beam focused mostly on the local line without changing the properties of SAWs. The focused IDT SAW device is a good approach for detecting micro-size droplets due to the better concentration of the energy traveling through the propagation path.

With the proposed multiple-IDT-layer M-SAW structures, it is possible to reduce the longitudinal component in SAWs and generate novel MAWs by mixing surface waves and plate waves on the piezoelectric material. The mixing acoustic wave component can propagate through the liquid medium. This provides a potential method in liquid sensing applications. Like the conventional SAW device, the M-SAW transducer response, based on the longitudinal displacement along the propagation path, depends on material parameters, such as the number of IDT pairs, substrate thickness, operating frequency and cut profile in simulation, but the effect is significantly stronger. The experimental results show that it is also sensitive to the position of the droplet, especially

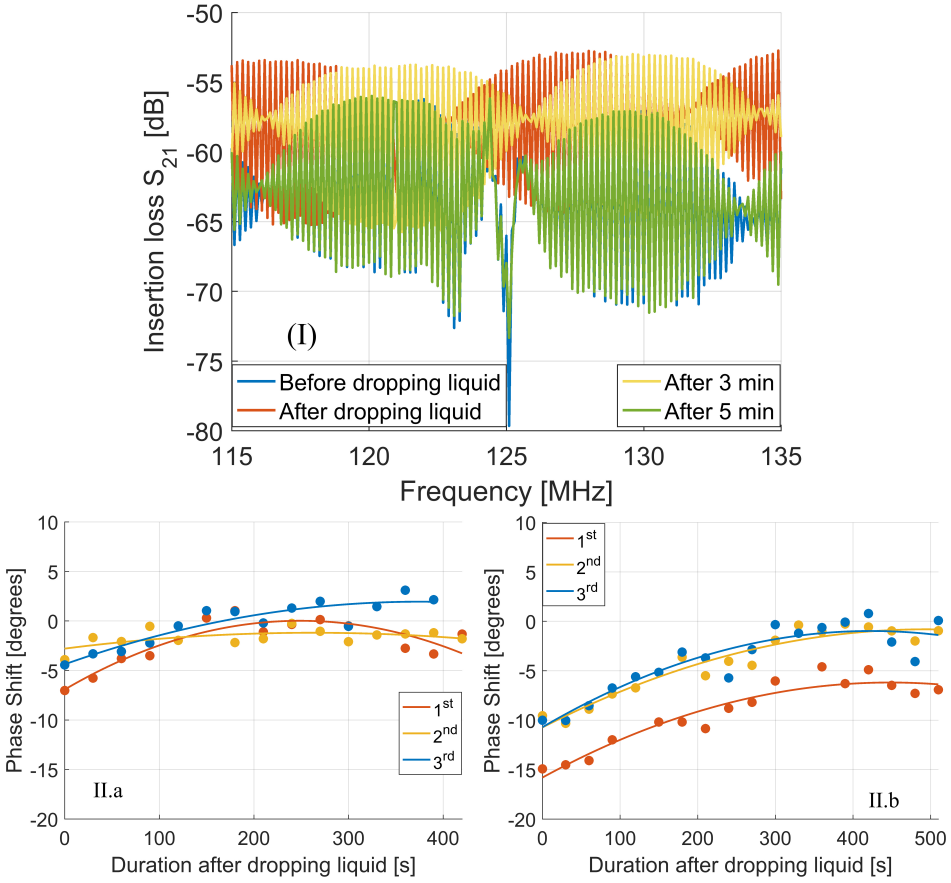

Figure 6.32: (I) The magnitude of the insertion loss of the M-SAW device with two IDT layers in dB during the third-stage vaporization of the liquid for a 0.1 µl volume and (II) phase shift when the droplet (a) less than 0.1 µl and (b) 0.13 µl is dropped at the middle of the propagation path.

when the droplet is placed in the middle of the propagation path, and to the volume of the liquid. The greater the phase shift of M-SAW structures, the larger the liquid volume dropped on the propagation surface. The M-SAW device with size of 4800 µm x 2500 µm can be used for the liquid range 0.05 – 0.13 µl, with a resolution of 0.03 µl. If the propagation area is increased or a confinement well for the liquid is integrated, larger volumes can be used as well.

REFERENCES

[1] T. H. Bui and D. T. Chu, *Multilayer saw device for flow rate sensing in a microfluidic channel,* in *SENSORS, 2013 IEEE* (2013).

[2] T. H. Bui, D. N. Tien, T. B. Duc, and T. C. Duc, *3-d finite element modeling of saw*

sensing system for liquids, in *IEEE/ASME International Conference on Advanced Intelligent Mechatronics AIM* (2012).

[3] T. T. Wu, T. HeTai, C. YungYu, and P. L. Liu, *Analysis and design of focused interdigital transducers,* Ultrasonics, Ferroelectrics, and Frequency Control, IEEE Transactions on (2005).

[4] T. H. Bui, T. B. Duc, and T. C. Duc, *An optimisation of idts for surface acoustic wave sensor,* International Journal of Nanotechnology (2015).

[5] S. K. R. S. Sankaranarayanan and V. R. Bhethanabotla, *Numerical analysis of wave generation and propagation in a focused surface acoustic wave device for potential microfluidics applications,* Journal of Applied Physics (2009).

[6] S. K. R. S. Sankaranarayanan and V. R. Bhethanabotla, *Design of efficient focused surface acoustic wave devices for potential microfluidic applications,* Journal of Applied Physics (2008).

[7] R. Singh and V. R. Bhethanabotla, *Design of mutually interacting multi-directional transducer configurations on a surface acoustic wave device for enhanced biosensing,* in *2009 IEEE Sensors* (2009).

[8] M. Kirci and E. Akcakaya, *Analysis of focused surface wave transducers,* in *IEE Proceedings G - Circuits, Devices and Systems* (1990).

[9] P. Marechal, F. Levassort, Tran-Huu-Hue, M. Lethiecq, and N. Felix, *P3p-7 modeling of lens focused piezoelectric transducer for medical imaging,* in *2006 IEEE Ultrasonics Symposium* (2006).

[10] R. Singh and V. R. Bhethanabotla, *Enhancement in ultrasonic micro-transport using focused inter-digital transducers in a surface acoustic wave device: Fluid-structure interaction study,* in *2009 IEEE Sensors* (2009).

[11] S. J. Martin and A. J. Ricco, *Sensing in liquids using acoustic plate mode devices,* in *1987 International Electron Devices Meeting* (1987).

[12] V. I. Anisimkin, C. Caliendo, and E. Verona, *Acoustic plate mode sensing in liquids based on free and electrically shorted plate surfaces,* Ultrasonics (2016).

[13] A. J. Ricco, S. J. Martin, T. M. Niemczyk, and a. G. C. Frye, *Liquid-phase sensors based on acoustic plate mode devices,* Chemical Sensors and Microinstrumentation (1989).

[14] S. Toshio, O. Hiroshi, K. Yutaka, M. Ryohei, and N. Haruhiko, *Shear horizontal acoustic plate mode viscosity sensor,* Japanese Journal of Applied Physics (1993).

[15] G. Kovacs and A. Venema, *Theoretical comparison of sensitivities of acoustic shear wave modes for (bio)chemical sensing in liquids,* Applied Physics Letters (1992).

[16] D. Morgan, *Surface Acoustic Wave Filters: With Applications to Electronic Communications and Signal Processing* (Elsevier Ltd., 2007).

[17] M. S. Kharusi and G. W. Farnell, *On diffraction and focusing in anisotropic crystals,* in *Proceedings of the IEEE* (1972).

[18] J. B. Green and G. S. Kino, *Saw convolvers using focused interdigital transducers,* IEEE Transactions on Sonics and Ultrasonics (1983).

[19] J. B. Green, G. S. Kino, and B. T. Khuri-Yakub, *Focused surface wave transducers on anisotropic substrates: A theory developed for the waveguided storage correlator,* in *1980 Ultrasonics Symposium* (1980).

[20] S. R. Fang, S. Y. Zhang, and Z. F. Lu, *Saw focusing by circular-arc interdigital transducers on yz-linbo3,* IEEE Transactions on Ultrasonics, Ferroelectrics, and Frequency Control (1989).

[21] T. H. Bui, D. T. Bui, and D. T. Chu, *Microfluidic injector simulation with fsaw sensor for 3-d integration,* Instrumentation and Measurement, IEEE Transactions on (2015).

[22] S. Showko and K. Jun, *Surface acoustic wave sensors,* Japanese Journal of Applied Physics (2004).

[23] M. Y. K.-Y. Hashimoto, *Excitation and propagation of shear-horizontal-type surface and bulk acoustic waves,* IEEE Transactions on Ultrasonics, Ferroelectrics, and Frequency Control (2001).

[24] K. Hashimoto, *Surface Acoustic Wave Devices in Telecommunications: Modelling and Simulation* (Berlin, Heidelberg: Springer Berlin Heidelberg, 2000).

[25] J. Kondoh, Y. Okiyama, S. Mikuni, Y. Matsui, H. Yatsuda, and M. Nara, *Development of sh-saw sensing system for liquids,* in *Frequency Control Symposium, 2007 Joint with the 21st European Frequency and Time Forum. IEEE International* (2007).

[26] J. Ballantine, R. M. White, S. I. Martin, A. J. Ricco, E. T. Zellers, G. C. Frye, and et al., *Acoustic Wave Sensors, 1st Edition: Theory, Design, & Physico-Chemical Applications* (USA: ACADEMIC PRESS, 1997).

[27] T. H. Bui, T. Scholtes, T. C. Duc, and P. M. Sarro, *A mixing surface acoustic wave device for liquid sensing applications: Design, simulation, and analysis,* in *IEEE-MEMS2016* (2016).

[28] G. A. Barnard, *Control charts and stochastic processes,* Journal of the Royal Statistical Society. Series B (Methodological) (1959).

[29] E. S. Page, *Continuous inspection schemes,* Biometrika (1954).

[30] A. Artieda and P. Muralt, *High-q aln/sio2 symmetric composite thin film bulk acoustic wave resonators,* IEEE Trans. on Ultrasonics, Ferroelectrics, and Frequency Control (2008).

7

CONCLUSION AND PERSPECTIVE

Surface acoustic wave devices have been used for a variety of microfluidic applications, especially in biochemical analysis and drug delivery. However, sensing capacity is extremely challenging for the SAW device due to leakage phenomena into the liquid medium. An approach to address this problem, so to fully exploit the potential of SAW devices in liquid sensing, using Aluminum Nitride as piezoelectric substrate, was presented in this study. Numerical analysis and experimental investigation of the mutual relation between surface acoustic waves generated on the AlN piezoelectric substrate and some physical properties of microdroplets was conducted. The main conclusions are given below, together with recommendations for future work.

7.1. CONCLUSIONS

SENSING applications of SAW devices based on AlN in liquids are investigated. Microliter volumes are considered to avoid the loss of the entire energy of the Rayleigh waves into the liquid medium. The piezoelectric material, AlN, is chosen because of its stable and good piezoelectric properties in a large temperature range, high acoustic velocity, high hardness and compatibility with the silicon IC microelectronic process. From the analysis of various deposition methods of this material, reactive sputtering appears to be the best choice. The fabrication process is based on surface micromachining, and the sputtering is optimized to obtain the best piezoelectric properties of the film. The devices use 50x50 pairs of IDTs and a sensing region (large cavity or microhole) is created in the center of the propagation path. This structure is used throughout the entire work to confine the liquid under investigation and validate the sensing capacity of the SAW device for liquid applications.

First, we analysed the SAW device with the presence of liquid inside the microhole. An important conclusion from the simulation results is that in the SAW device with the embedded hole, the energy is not entirely attenuated, thus there is still an output voltage value at the receiver. These results also show that the SAW device is sensitive to density changes of the liquid and to small changes at the nozzle of the embedded hole, specifically pressure.

Based on the simulation results, we continued to investigate the response of the SAW device to the liquid medium in the microliter volume range. This experiment uses the typical configuration of the SAW device including a pair of transmitter and receiver IDTs. The numerical analysis of the mutual relation between the attenuation of the SAW beam and the presence of microliter volume liquid has been carried out. The device is capable to differentiate the energy emitted into the same liquid but with different microliter volumes. This is expressed by the fraction coefficient $\alpha \sim kr^2 \frac{\sin\theta(2+\cos\theta)}{(1+\cos\theta)^2}$. The change in contact radius influences the fraction coefficient more than the change in contact angle, especially on hydrophilic ($\theta < 90^0$) and super-hydrophilic surfaces ($\theta \ll 90^0$). The energy variation happened continuously during the evaporation process of the sessile droplet placed on the middle of the piezoelectric propagation path. This shows that the SAW device is sensitive to the changing volume of the liquid. Besides, this also highlights the need to consider, for proper use of SAW devices in microfluidic applications, the shape of the droplet on the surface, the effect of the evaporation, the droplet volume and the surface wettability, especially for experiments which requires long-time actuation and manipulation.

To study the behaviour of the SAW device in a liquid medium, we investigated the evaporation process of different microliter volume liquid samples. These samples can have different density or similar density but different stagnant liquid molecules after evaporation. The experimental results show that the response of the SAW device is also sensitive to differences in density and stagnant liquid molecules because both lead to changes in surface mass density of the piezoelectric material. This suggests a potential method to identify liquid samples of microliter volumes in microfluidic biosensors based on the SAW device.

Next, a novel SAW device equipped with an embedded microhole is proposed for the control and monitor of the contact area between the piezoelectric material and the

liquid medium. The simulation and experimental results show that the presence of the microhole only affects attenuation of the SAW device in magnitude. The first results confirm the sensitivity of the SAW device. In fact, the SAW devices response corresponding to changes in both parameters, pressure and density of the liquid inserted in the microhole, and to each change in density or pressure, can be measured. The first testing principle is based on the evaporation capillary phenomenon between different free surfaces, which affects the concentration of liquid inside the microhole, and the pressure on the wall of the microhole. The output signal changes when small changes in both pressure and liquid concentration take place during the long evaporation process of the liquid or when each of them (density or pressure) separately varies. These experimental results once more indicate the applicability of SAW devices for liquid sensing, especially for liquid flowing inside a tubular structure.

Finally, the simulation and experimental results showed that SAW devices with circular shape FIDTs have better performance, and is a good approach for detecting microsize droplets due to the better concentration of the energy traveling through the propagation path. Also, multiple-IDT-layer mixing surface acoustic wave (M-SAW) structures are proposed to reduce the longitudinal component in SAWs and generate novel MAWs by mixing surface waves and plate waves on the piezoelectric material. This novel configuration simply needs 2 layers of input IDTs. The mixing acoustic wave component can propagate through the liquid medium. Therefore, while the response of a conventional SAW device goes to zero in the presence of a liquid medium on the propagation path, the responsible term $\frac{sinX}{X}$ disappears in the response of the proposed SAW structure.

7.2. RECOMMENDATIONS FOR FUTURE WORK

THE theoretical analysis and experimental results reported in this thesis show the potential of liquid sensing of SAW devices. Initial applications of the proposed devices demonstrated the possibility to provide liquid type identification or fluid level measurement. Other applications such as sensing liquid flow, contaminated liquid or the presence of particles in the liquid medium, can also be targeted. Besides, new currently promising materials, like LiNbO3, could be explored and the proposed FIDT SAW devices could be experimentally realized and validated. Therefore, future work can extend this research in the following directions:

- For a first order analysis, the size of the SAW device was 4800 x 1000 or 1200 x 1000 µm, targeting liquid volumes below 0.13 or 0.05 µl. If different volume ranges are targeted, the cavity (microhole) can be modified to accommodate the difference in liquid volume. This can be incorporated into commercial products designed for the identification of liquid samples.
- The experiment shows not only the SAW response to the different surfaces where the droplet is placed, but also its sensitivity to the droplet size. Further investigation should be carried out. Closed-cavity of the SAW device is recommended to avoid the effect of ambient (humidity and temperature) changes.
- With respect to the employed technology, improvements can be achieved with respect to the cavity formation. For example, SOI substrates with a device layer thickness of 20 µm could be used, shortening the process and providing an accurate control on the required cavity depth.

• The preliminary experiments of the micro-hole SAW device show its applicability in the detection of liquid flow or liquid level based on equivalent phenomena (evaporation, effect of density and pressure). Further, the effect of assembling with an injector should be studied as well. The SAW devices should be further tested for the detection of the presence and concentration of substances/contaminants in a liquid solution. SAW-based structures (embedded micro-cavities and holes) can be possibly applied in other microfluidics applications, such as biological cell models.

• With the mixing model and focused IDT SAW structure introduced in this study, better SAW performance could be achieved. These could be further experimentally tested following a similar method as the one used to detect the presence and concentration of substances in liquid medium or to identify a liquid.

• Other piezoelectric material, like quartz crystal with good temperature stability and possibility for etching with a high precision, could be explored with the same device configuration. The operating frequency of the generated SAWs could then be much lower, or closer to the frequency of the carrier signal (induced by the substances to be detected).

APPENDIX-A: PARAMETERS OF PIEZOELECTRIC AND SOME LIQUIDS

Aluminum nitride is a piezoelectric material with the class 6-mm symmetry. Its piezoelectric coefficient matrices of coupling, elasticity and relative permittivity are used in simulation as below:

$$c_f = \begin{pmatrix} c_f & c_f & c_f & 0 & 0 & 0 \\ c_f & c_f & c_f & 0 & 0 & 0 \\ c_f & c_f & c_f & 0 & 0 & 0 \\ 0 & 0 & 0 & 0 & 0 & 0 \\ 0 & 0 & 0 & 0 & 0 & 0 \\ 0 & 0 & 0 & 0 & 0 & 0 \end{pmatrix}$$

$$c = \begin{pmatrix} c_{11} & c_{12} & c_{13} & 0 & 0 & 0 \\ c_{12} & c_{11} & c_{13} & 0 & 0 & 0 \\ c_{13} & c_{13} & c_{33} & 0 & 0 & 0 \\ 0 & 0 & 0 & c_{44} & 0 & 0 \\ 0 & 0 & 0 & 0 & c_{44} & 0 \\ 0 & 0 & 0 & 0 & 0 & \frac{(c_{11}-c_{12})}{2}) \end{pmatrix}$$

$$e = \begin{pmatrix} 0 & 0 & 0 & 0 & e_{15} & 0 \\ 0 & 0 & 0 & e_{15} & 0 & 0 \\ e_{31} & e_{31} & e_{33} & 0 & 0 & 0 \end{pmatrix}$$

$$\varepsilon = \begin{pmatrix} \varepsilon_{11} & 0 & 0 \\ 0 & \varepsilon_{11} & 0 \\ 0 & 0 & \varepsilon_{33} \end{pmatrix}$$

where $c_{11} = 345GPa$, $c_{33} = 395GPa$, $c_{44} = 118GPa$, $c_{12} = 125GPa$, $c_{13} = 120GPa$, $c_f = 2.25GPa$, $e_{15} = -0.48C/m^2$, $e_{31} = -0.58C/m^2$, $e_{33} = 1.55C/m^2$, $\varepsilon_{11} = 9$, $\varepsilon_{33} = 11$. $\rho_p = 3260kg/m^3$ and $v_p = 5049m/s$ for the piezoelectric medium. $\rho_f = 1000kg/m^3$ and $v_l = c_l = 1480m/s$ for the liquid medium.

SUMMARY

The thesis focuses on the investigation of thin-film surface acoustic wave (SAW) devices for liquid sensing applications. The piezoelectric material is a thin film of Aluminum Nitride (AlN), a CMOS compatible material, deposited by pulse DC reactive sputtering technique. A CMOS compatible process is developed and employed to fabricate the AlN/Si surface acoustic wave (SAW) devices which operate in a liquid medium. The applicability of the SAW device in sensing liquid is proved by numerical analysis, simulations and experimental results.

In the first chapter, the development of liquid sensors based on MEMS fabrication is introduced together with the wide range of applications for these devices. Also, the motivation to investigate the SAW device based on thin film AlN for liquid sensing is presented. In chapter 2, sensing mechanisms in general and applicable mechanisms of SAW sensors for liquid are presented. To determine the most suitable design of the SAW devices, three-dimension (3D) modeling based on the finite element method (FEM) is performed and analyzed.

Chapter 3 reports on the effect of a micro-size droplet shape, specifically the liquid contact angle, radius (area) and wettability of the contact surface on the SAW response. The numerical analysis and experimental results explain the interaction mechanism between the attenuated SAW beam and micro-droplets. The beam, which is emitted into the droplet, is expressed by the fraction coefficient. The change in contact radius r influences the fraction coefficient more than the change in contact angle θ, especially on hydrophilic and super-hydrophilic surfaces.

In chapter 4, the first applicability of the SAW sensor is demonstrated by identifying the kind of liquid present on the propagation path. The sensing mechanism is based on physical properties (liquid density, sound speed in liquid and evaporation rate) and mass loading (concentration of stagnant liquid molecules). This also suggests a potential method to identify liquid samples of microliter volumes in microfluidic biosensors based on this SAW device.

In chapter 5, a SAW device equipped with an embedded microhole is proposed for the control and monitoring of the contact area between the piezoelectric material and the liquid medium. The device is miniaturized to be integrated on a printed circuit board (PCB). The device response to changes in density and pressure as well as to the evaporation of the liquid inside the microhole is studied. These initial indirect experimental results show the applicability of the SAW device for the state of liquid flow inside the microhole.

In chapter 6, some optimized structures of the SAW device are proposed. The simulation and experimental results showed that SAW devices with circular shape FIDTs have better performance, and provide a good method to detect micro-size droplets due to the better concentration of the energy traveling through the propagation path. Also in this chapter, a mixing IDT structure for SAW devices, which includes two layers of input IDTs,

is proposed to reduce the longitudinal component in SAWs and generate novel mixing acoustic waves by mixing surface waves and plate waves on the piezoelectric material.

Finally, in chapter 7 concluding remarks and recommendations for future work are given.

SAMENVATTING

Deze dissertatie focust op het onderzoek naar dunne laag oppervlakte akoestische golf (SAW) apparaten voor vloeistof waarneming toepassingen. Het piëzo-elektrisch materiaal is een dunne laag van aluminiumnitride (AIN), een CMOS verenigbaar materiaal, gedeponeerd door middel van een puls DC reactieve sputter techniek. Een CMOS verenigbaar proces is ontwikkeld en gebruikt om de AIN/Si SAW apparaten te fabriceren die werken in een vloeibaar medium. De toepasbaarheid van het SAW apparaat in het waarnemen van vloeistof is bewezen met numerieke analyse, simulaties en experimentele resultaten.

In het eerste hoofdstuk wordt de ontwikkeling van vloeistof sensoren gebaseerd op MEMS fabricatie geïntroduceerd tezamen met de wijde selectie van toepassingen voor deze apparaten. Eveneens wordt de motivatie voor het onderzoek naar het SAW apparaat gebaseerd op dunne laag AIN voor vloeistof waarneming gepresenteerd. In hoofdstuk 2 worden algemene waarneming mechanismen en toepasbare mechanismen van SAW sensoren voor vloeistoffen gepresenteerd. Om het meest geschikte ontwerp van de SAW apparaten te bepalen, is drie dimensionale (3D) modelering gebaseerd op de eindige elementen methode (FEM) uitgevoerd en geanalyseerd.

Hoofdstuk 3 rapporteert het effect van een microformaat druppel vorm, specifiek de vloeistof contact hoek, radius (oppervlakte) en bevochtigbaarheid van het contact oppervlak op de SAW respons. De numerieke analyse en experimentele resultaten verklaren het interactie mechanisme tussen de verzwakte SAW straal en micro-druppels. De straal, welke wordt uitgezonden in de druppel, wordt uitgedrukt door de fractie coëfficiënt. De verandering in contact radius r beïnvloed de fractie coëfficiënt meer dan verandering in contact hoek θ, met name op hydrofiele en super-hydrofiele oppervlaktes.

In hoofdstuk 4 is de eerste applicatie van de SAW sensor gedemonstreerd door het soort vloeistof in het propagatie pad te identificeren. Het waarnemend mechanisme is gebaseerd op fysische eigenschappen (vloeistof dichtheid, snelheid van geluid in vloeistof en verdamping snelheid) en massa laden (concentratie van de stagnerende vloeibare moleculen). Dit suggereert ook het bestaan van een potentiele methode, gebaseerd op dit SAW apparaat, om vloeibare monsters van microliter volumes in microvloeistof biosensoren te identificeren.

In hoofdstuk 5 wordt een SAW apparaat, uitgerust met een ingebed micro gat, voorgesteld voor de controle en observatie van het contact oppervlak tussen het piëzo-elektrisch materiaal en vloeibaar medium. Het apparaat is geminiaturizeerd zodat het kan worden geïntegreerd op een printplaat (PCB). De reactie van het apparaat op veranderingen in dichtheid en druk, maar ook verandering in de verdamping van de vloeistof in het micro gat, zijn bestudeerd. Deze initiële experimentele resultaten laten de toepasbaarheid van het SAW apparaat voor de toestand van de vloeistof stroom in het micro gat zien.

In hoofdstuk 6 worden enkele geoptimaliseerde structuren voor het SAW apparaat voorgesteld. De simulatie en experimentele resultaten lieten zien dat SAW apparaten met ronde vorm FIDTs beter presteerden en verschaffen een goede methode om microformaat druppels te detecteren vanwege de betere concentratie van de bewegende energie door het propagatie pad. Dit hoofdstuk stelt ook een mengend IDT structuur voor, welke twee invoer lagen bevat, om de lengte component in SAWs te reduceren en genereert nieuwe mengende akoestische golven door oppervlakte golven en plaat golven te mengen op het piëzo-elektrisch materiaal.

Ten slotte zijn in hoofdstuk 7 afsluitende opmerkingen en aanbevelingen voor toekomstig onderzoek gegeven.

LIST OF PUBLICATIONS

Journal Publications

7. **ThuHang Bui**, Jia Wei, Bruno Morana, Trinh Chu Duc and Pasqualina M. Sarro, "A novel on-chip SAW device with the vertical hole for microfluidcs", (Submitted).

6. **ThuHang Bui**, Van Nguyen, Sten Vollebregt, Bruno Morana, Henk van Zeijl, Trinh Chu Duc, and Pasqualina M. Sarro, "Effect of Droplet Shrinking on Surface Acoustic Wave Response in Microfluidic Applications", *Applied Surface Science*, 2017.

5. **ThuHang Bui**, Bruno Morana, Atef B. Akhnoukh, Trinh Chu Duc, and Pasqualina M. Sarro, "Liquid Identification by a Micro-electro-mechanical Interdigital Transducer", *Analyst*, 2017.

4. **ThuHang Bui**, Bruno Morana, Tom Scholtes, Trinh Chu Duc, and Pasqualina M. Sarro "A mixing surface acoustic wave device for liquid sensing applications: Design, simulation, and analysis", *Journal of Applied Physics*, 120, 074504, 2016.

3. **ThuHang Bui**, Tung Bui Duc and Trinh Chu Duc, "Microfluidic Injector Simulation with F-SAW Sensor for 3D Integration", *IEEE Trans. on Instrumentation and Measurement*, Vol. 64, No. 4, pp. 849 - 856, Apr. 2015.

2. **ThuHang Bui**, Tung Bui Duc and Trinh Chu Duc, "An optimization of IDTs for surface acoustic wave sensor", *Int. J. Nanotechnology*, Vol.12, No.5/6/7, pp.485 – 495, 2015.

1. **ThuHang Bui**, Bui Duc Tung, Nguyen Tien Dat and Chu Duc Trinh, "Attenuation Coefficient for Surface Acoustic Waves in Fluid Region", *Vietnam Journal of Mechanics*, ISSN: 0866 7136, vol. 34, no. 4, pp. 225-236, 2012.

Conference

10. **ThuHang Bui**, An Tran, Bruno Morana, Jia Wei, Trinh Chu Duc, Pasqualina M. Sarro, "Effect of the Interruption of the Propagation Path on the Response of Surface Acoustic Wave Transducers", *IEEE-Sensors2016*, USA, Oct 30 – Nov 2, pp. 745-747.

9. **ThuHang Bui**, Bruno Morana, Trinh Chu Duc and Pasqualina M. Sarro, "A novel mixing surface acoustic wave device for liquid sensing applications", *2016 IEEE 29th International Conference on Micro Electro Mechanical Systems (IEEE MEMS2016)*, China, ISBN: 978-1-5090-1973-1/16.

8. **ThuHang Bui**, Bruno Morana, An Tran, Tom Scholtes, Trinh Chu Duc and Pasqualina M. Sarro, "SAW device for liquid vaporization rate and remaining molecule sensing", *IEEE-Sensors2015*, Korea, Nov. 1-4, ISBN: 978-1-4799-8203-5/15.

7. **ThuHang Bui**, Tung Bui Duc and Trinh Chu Duc, Lina Sarro, "Associated IDTs in Surface Acoustic Wave Devices for Closed-loop Control Inkjet System", *IEEE-Sensors2014*, Spanish, Nov. 3-5, pp. 1936-1939, ISBN: 978-1-4799-0162-3/14.

6. Tung Bui Duc, Nam Pham Hoai, **ThuHang Bui**, Trinh Chu Duc, "Effect of the focused surface acoustic wave devices on the microfluidic channel", *Proceedings of ICEMA 2014*, pp.221-225.

5. **ThuHang Bui**, and Trinh Chu Duc, "Microfluidic Injector Simulation with SAW Sensor for 3D Integration", *IEEE-Sensors Applications Symposium 2014*, Queenstown, New Zealand, February 18-20, pp. 213-218, ISBN: 978-1-4799-2179-9/14.

4. **ThuHang Bui**, Tung Bui Duc and Trinh Chu Duc, "An optimization of IDTs for surface acoustic wave sensor", *Proceedings of IWNA 2013*, November 14-16, 2013, Vung Tau, Vietnam, pp. 159-162.

3. **ThuHang Bui**, and Trinh Chu Duc, "Multilayer SAW device for flow rate sensing in a microfluidic channel", *IEEE-Sensors2013*, Maryland, USA, November 3-6, pp. 487-490, ISBN: 978-1-4673-4642-9/13.

2. **ThuHang Bui**, Dat Nguyen Tien, Tung Bui Duc and Trinh Chu Duc, "3-D Finite Element Modeling of SAW sensing system for liquids", *IEEE/ASME Int. Conf. on Advanced Intelligent Mechatronics 2012*, Kaohsiung, Taiwan, July 11-14, pp. 782 – 787, ISSN: 2159-6247, Print ISBN: 978-1-4673-2575-2.

1. Tung Bui Duc, **ThuHang Bui**, Dat Nguyen Tien and Trinh Chu Duc, "R-SAW Analysis on Single-Crystal AlN Substrate for Liquid Sensors", *Proceedings of ICEMA 2012*, August 16-17, 2012, Hanoi, ISBN: 978-604-913-097-7, pp. 13-18.

Workshop

1. **ThuHang Bui**, and Trinh Chu Duc, "Focused surface acoustic wave devices for pressure sensing at inkjet nozzle", *8th Interantional Symposium on Organic Molecular Electronics (ISOME)*, Japan (2014).

ACKNOWLEDGEMENTS

My PhD left the biggest impression on my life up until now. In this time, I have made many new friends and supporters and experienced some of the most important events in my life. Here, I want to express my gratitude towards them.

I would like first to sincerely thank my promotor, Prof. dr. Pasqilina M. Sarro, for her understanding, guidance, encouragement and strong support during the whole time spent at TU Delft. Without her patience, encouragement and wise guidance, writing papers and this thesis would have never happened. Words are not enough to express how greatly indebted to her I feel and how proud I am of being her student and a member of her research group. I am very grateful to her for her fruitful discussion on each paper and most importantly for her patience and thorough attention when reading and revising my writing. She has constantly encouraged me in all of my ambitions, even when not directly related to my work. She truly gave me the different perspective about working with a professor means.

I would also like to sincerely thank my co-promotor, Prof. Trinh Chu Duc. He initially introduction into MEMS and later to Prof. Sarro and effectively enabled me to pursue my PhD at TU Delft. His guidance and suggestions during this time was invaluable. I would also like to express my gratitude for his supervision at the University of Engineering and Technology, VNU-HN during my M.Sc. studies. I appreciate his personal support and guidance, not only for the gained knowledge in the shape of the first lessons about MEMS and cleanroom but also for gaining passion in research.

I need to express my thanks to the other committee members, Prof. Joost Lotters, Prof. Michael Johannes Vellekoop, Prof. Paddy French, Prof. Peter Steeneken and Dr. Gregory Pandraud for corrections, comments and suggestions to improve my thesis and further work. I am especially grateful to Gregory for his help setting up the first devices when I just came to TU Delft.

I would like to thank Dr. Tran Trong An for his help in creating the first devices which I made in DIMES. With meticulous training, instructions and help of An and Hugo Schellevis, a former member in EKL, for Aluminum Nitride sputter, I quickly fabricated the first SAW devices. An trained me first lessons in the cleanroom and setup the measurement system for the SAW device, especially told me who I can ask when I get a problem. So my start was quite smoothly.

The first friend I made in EKL after I arrived was Bruno Morana. Everyone jokes that he is like a big boss because of his wide knowledge and kindness. Many thanks for his suggestions on the design of my devic. I am also grateful to Bruno's contribution in my publications. I also thank Jia Wei for his help, advice and contributing to my first design of the SAW device.

Other people I need to express my thanks are Tom Scholtes, Mario Laros, Henk van Zeijl, Koos van Hartingsveldt, Silvana Milosavljević, Cassan Visser, Johan van der Cingel, Johannes van Wingerden and thank again to Gregory Pandraud for sharing technical

knowledge. They were really patient and helpful every time I got troubles in the cleanroom. Thanks to Henk van Zeijl for helping me to solve challenging problems in the lithography steps. Especially thanks to Tom Scholtes and Mario Laros for all the times the worked late and helped me finish the process. I understand more about the Netherlands and Dutch culture through the conversations with Tom Scholtes and Mario Laros. Like an uncle, Tom asked, instructed and advised me when I worked in the cleanroom.

I would also like to thank Atef Akhnoukh from the Electronics Research Laboratory (ELCA), Sten Vollebregt for performing the measurement system of the SAW device. Many thanks to Atef for giving me many tips and advice for measuring, choosing probes and designing PCB.

I would like to thank Wim van der Vlist for training me on how to use the dicing machine, his kind help and infinite patience. You helped and taught me how to dice and wire-bond my devices and structures. Many thanks to Koos van Hartingsveldt for help me dicing and bonding as well.

Many thanks to Marcel Bus from the Department of Chemical Engineering (ChemE) for his thorough training on AFM, especially PFM mode.

My appreciations and gratitude goes to Marian Roozenburg for solving my administrative problems and Veronique van der Varst for her support related to my PhD position and my initial time in Delft.

I would like to thank Joost Romijn for translating my summary into Dutch.

I am lucky for working in close with the ECTM group which includes friendly, warm and enthusiastic members. I am glad to work, cooperate, enjoy lunch times with them, especially Bruno Morana, Cinzia Silvestri, Yelena Grachova, Nikolas Gaio, Marta Kluba, Aleksandar Jovic, Paolo Sberna, Rene Poelma, Filiberto Ricciardella, Violeta Prodanovic, Hong Wah Chan, Jian Li, William Quiros Solano, Xueming Li, Hengqian Yi, Juan Alfaro Barrantes.

I met many new friends when I studied in TU Delft in 4 years. They have made my life full of color and helped me get rid of the negative emotions during my PhD life. I really enjoyed the time spent with my roomates Yen Vu, Ha Nguyen Thi Thu. I am also grateful for meeting many Vietnamese friends on Tet holidays, summer seasons, seniors' defenses. I would like to thank to them: HoangAnh Nguyen Du, Quynh Tran Tran Thien, Minh Ha Do, Thang Nguyen, Hang Ngo (IHE), Duoc Nguyen (IHE), Hung Phan, KimAnh Do Thi, Huong Bui Thi, Thien Vu Trong, Ngan Vu, Son Truong Hong, and also to all other friends not explicitly mentioned here. I really appreciate the time we spent together.

Special thanks to my best cousin, Phan Quoc Vi, who always encouraged me to study and pursue my dreams. Due to his generosity, I always had the best computers as an undergraduate. Thanks to my sister, Bui Thu Thuy, who helped me take care of mom when I studied aboard and encouraged me keep focusing on my studies.

My best appreciation and gratitude to my mom who gave my birth, brought me up and taught me alone after my dad passed away. Without her spiritual support and encouragement in all ways I passed, this time never comes. She is always by my side when I am down, stressed or on my way to becoming a mother myself.

Last but not least, I am grateful to my husband Catalin for his understanding and support. He is always by my side and encouraged me, especially when I was down because of troubles in the process and measurement. Thanks to my new baby Anna, she

brings me spiritual support, motivation, happiness and joy.

ABOUT THE AUTHOR

Thu Hang BUI

Thu Hang Bui was born on 16 June 1987 in Hanoi, VietNam. She received the B.Sc. degree in telecommunication and electronic engineering from Hanoi University of Science and Technology (former name Hanoi University of Technology, HUST) in 2010. The M.Sc. degree which she received in telecommunications and electronics at University of Engineer and Technology, Vietnam National University, Hanoi (UET-VNU, HN).

From 2011 to 2014, she worked as an assistant lecturer in MEMS group, Telecommunications and Electronics department, University of Engineer and Technology, Vietnam National University, Hanoi (UET-VNU, HN). Her research is about piezoelectric technology, especially fundamental and simulations of the SAW devices for microfluidics applications.

In September 2014, she moved to The Netherlands for the PhD program of Technical University of Delft. During the Ph.D., she focused on investigation of the SAW device and new suitable designs of the SAW device for sensing liquids. Her research interests include piezoelectric sensors and microfabrication technologies.